From air to leaves and soils: How atmospheric mercury released from informal gold mines moves through the ecosystems and degrades plant health.

Robin Ruhm

A dissertation submitted in partial fulfillment

of the requirements for the degree of

Doctor of Philosophy

University of Washington

2026

Reading Committee:

Rebecca Neumann, chair

Eric Cosio

Sarah Janssen

Alex Turner

Program Authorized to Offer Degree:

Civil and Environmental Engineering

University of Washington

Abstract

From air to leaves and soils: How atmospheric mercury released from informal gold mines moves through the ecosystems and degrades plant health.

Robin Ruhm

Chair of the Supervisory Committee:

Rebecca Neumann

Department of Civil and Environmental Engineering

Since the 1990s, informal gold mining has spread across the Amazon. Due to its propensity to amalgamate with gold, mercury is added to fine sands, enabling the extraction of gold held within. This mercury is ultimately vaporized off gold amalgam, spreading downwind. Informal gold mining is now considered the leading global emitter of mercury, with 40% of gold mining emissions released in the Amazon. However, existing research has only begun to characterize the downwind fate and regional-to-global implications of Amazon mercury emissions into the atmosphere.

In Chapter 2, we predict at a high resolution where emissions occur and how they move downwind. We use remote sensing, Lagrangian transport, and on-the-ground mercury data to jointly model Amazon gold-mining emissions and their downwind concentration footprints at a 1-kilometer scale, annually between 2001 and 2024. We estimate a 5-fold

Amazon-wide mercury emission increase between 2001 and 2017; emissions rose with gold price and livelihood insecurity during the 2015-2016 El Niño drought but plateaued following the 2017 Minamata Convention. Our model predicts measured air-mercury concentrations with a log concordance correlation of 0.79 compared to near-zero correlations when atmospheric transport is applied to existing inventories. Extended across the Amazon, our model finds that 100,000 km^2 of land area experience more than double background mercury levels with disproportionate effects in urban centers, where gold shops burn mercury amalgam. As a result, between 8,000 and 220,000 urban residents are exposed to toxic levels, depending on the applied toxicity threshold. This model offers scientists, environmental nonprofits, and community organizations a tool to characterize mercury emissions, their drivers, and downwind exposure.

In Chapter 3, we consider the impacts of mercury emissions from Amazon gold mining on forest productivity. Across a mercury contamination gradient, field sampling revealed significant cross-species declines in oxygen-evolving complex performance, leaf size, and diameter at breast height, with species-dependent declines in photosystem I performance and chlorophyll content. Combining satellite remote sensing of forest productivity and Chapter 2's mercury concentration footprint maps, we estimate that long-term low mercury doses result in a 3.7% per $\mathrm{ng\ m}^{-3}$ exposure reduction in plant productivity with forests recovering 10-15 years after mercury exposure stops. Across the Amazon, mercury toxicity results in a 23 MtC annual loss in Amazon rainforest gross primary productivity, which exceeds the losses associated with direct deforestation. The combined deforestation and mercury-induced productivity declines result in a 9% reduction in

annual net carbon storage across the Amazon. These productivity declines may propagate up the food chain and reduce crop productivity; may reduce transpiration, worsening Amazon drought and pushing an additional 1,500 km^2 of vulnerable forests towards a die-off tipping point; and may extend to global forest productivity declines from an enriched global atmospheric cycle. This chapter highlights hidden social and ecological impacts from gold mining due to mercury's impact on plant productivity, whose social cost rivals the value of gold produced.

Chapter 4 asks what happens to mercury once it has spread across the regional atmosphere. Using a gradient flux setup, we found that dry deposition of mercury directly from air into soil is the leading flux, outpacing leaf uptake. We estimated that approximately 40% of Amazon mercury emissions ultimately deposit regionally rather than entering the global mercury cycle. Once in soils, this mercury is subject to a couple of loss pathways. We found that 26-59% of terrestrial mercury soil deposition—primarily at low relative elevations—erodes into waterways, potentially explaining $76 \pm 15\%$ of observed river mercury in the heavily mined Madre de Dios region. Eroded mercury threatens aquatic ecosystems, whereas the remaining 41-74% of soil mercury likely evades back into the atmosphere, where it can travel globally. We found that Amazon deforestation rapidly accelerates evasion, emitting 1 to 2 times the mercury released from all Amazon alluvial gold mining. Together the atmospheric loading, erosion, and deforestation explain 74% of surficial soil-mercury variation, which allowed us to build 1-km resolution soil-mercury prediction maps that may support future research or community risk assessment.

Together, this dissertation tracks the movement of mercury from emission sources, the downwind impacts on forest productivity, and this mercury's long-term fate in regional ecosystems. These findings highlight the regional-to-global drivers and impacts of Amazon informal gold mining and may support regional mercury exposure mitigation and global mercury budgeting.

TABLE OF CONTENTS

LIST OF FIGURES **10**

LIST OF TABLES **15**

Chapter 1. Introduction ***16***

1.1. Background **16**

1.2. Dissertation Overview **17**

1.3. Positionality Statement **19**

1.4. Acknowledgements **20**

Chapter 2. A High-Resolution Approach to Estimate Gold-Mining Mercury Emissions and Their Downwind Concentration Footprints ***23***

2.1. Introduction **23**

2.1.1. Graphical Abstract 24

2.2. Methods and Materials **24**

2.2.1. Gold mining identification 24

2.2.2. Model Parameterization 24

2.2.3. Atmospheric Transport 25

2.2.4. Model Calibration 25

2.2.5. Uncertainty estimation 26

2.2.6. Mining Concentration Impact Analysis 26

2.2.7. Passive Mercury Sampling 27

2.3. Results and Discussion **27**

2.3.1. Model optimization, accuracy, and uncertainty 27

2.3.2. Comparing SMDN Emissions with Existing Inventories 30

2.3.3. Spatial and Temporal Trends in Emissions 32

2.3.4. Using Concentration Footprints to Understand Ecosystem and Human Exposure 35

2.3.5. Synthesis and Outlook 39

Chapter 3. Mercury Emissions from Amazon Gold Mining Reduce Forest Productivity and Carbon Stocks ***41***

3.1. Introduction **41**

3.2. Methods **42**

3.2.1. Leaf Sampling 42

3.2.2. Total Mercury Analysis 43

3.2.3. Building MODIS Annual De-Seasonalized NIRv Greenness Composites 43

3.2.4. Mercury Concentration Footprint Selection 45

3.2.5. Regression Methodology 45

3.2.6. Regression Uncertainty 46

3.2.7. Isolating Downwind Mercury Impacts from Confounding Variables 47

3.2.8. Gross Primary Productivity and NPP impacts 48

3.3. Results and Discussion 48

3.3.1. Amazon Plant Toxicity during Moderate Air-Mercury Exposure 48

3.3.2. Using Satellite Greenness to Estimate Amazon GPP Declines 51

3.3.3. Aggregate Amazon Forest Productivity Loss 53

3.3.4. Additional Predicted Environmental Impacts 54

3.3.5. The Regional and Global Costs of Productivity Loss 56

Chapter 4. Terrestrial Cycling and Fate of Mercury in the Amazon 59

4.1. Introduction 59

4.1.1. Graphical Abstract 60

4.2. Methods 60

4.2.1. Field Sampling and Prior Dataset Inclusion 60

4.2.2. Flux Tower Measurements Collected 62

4.2.3. Gradient Flux Calculation 63

4.2.4. Using the Gradient Flux Method to Estimate Mercury's Dry Deposition, Stomatal Uptake, and Evasion 65

4.2.5. Extending Fluxes to the Broader Amazon. 66

4.2.6. Total Mercury and Mercury Isotope Analysis 67

4.2.7. Soil Organic Carbon Analysis 68

4.2.8. Leaf Endmember Modeling from and Soil and Air Inputs 69

4.2.9. Applying Lagrangian Transport to Estimate the Fate of Emissions 70

4.2.10. Soil Mercury Prediction: Loading, Topography, and Deforestation 70

4.3. Results and Discussion 72

4.3.1. Estimating Fluxes at the Los Amigos Biological Station 72

4.3.2. Soil and Air Mercury Co-Determine Leaf Mercury 74

4.3.3. Quantifying the Regional and Global Fate of Amazon Mercury Emissions 77

4.3.4. Mercury Loading Explains the Soil-Mercury Enrichment 79

4.3.5. Topography Explains Baseline Soil Mercury 81

4.3.6. Eroded Mercury Depletes Soils and Enriches Rivers 82

4.3.7. Deforestation: A Leading Amazon Mercury Emission Source 84

4.3.8. Mapping Surficial Soil-Mercury Concentrations 86

4.3.9. Broader Implications 87

Chapter 5. Conclusion 90

5.1. Key Findings and Implications 90

5.2. Closing Thoughts: Addressing Gold Mining's Impacts 91

REFERENCES 94

Chapter 6. Supplemental Information 112

6.1. Chapter 2 Supplemental Information 112

6.1.1. Model Parameterization 112

6.1.2. Lagrangian Transport Modeling 112

6.1.3. Lagrangian Transport Model Uncertainty 113

6.1.4. Uncertainty in Kilometer-Scale Emission Modeling..... 115

6.2. Chapter 3 Supplemental Information 116

6.2.1. Speculated Agricultural Productivity Declines 116

6.2.2. Potential Global Plant Productivity Declines 116

6.2.3. Mining Reduces Downwind Precipitation and Accelerates Forest Die-Off 117

6.3. Chapter 4 Supplemental Information 118

6.3.1. Eddy Diffusivity Model Parameterization 118

6.3.2. Residence Time of Soil Mercury 118

6.3.3. Evasion Pathways at High Relative Elevations 119

6.3.4. Prior River-Mercury Literature is Consistent with Erosion 120

6.4. Supplementary Figures 121

6.5. Supplementary Tables 129

LIST OF FIGURES

Figure 2-1. Mercury emissions and concentration map for Madre de Dios, Peru. Panel A displays modeled 2017 mercury emissions using the mining deforestation emissions model in Madre de Dios, Peru separated by mining site emissions (gold) and mining town emissions (purple). Panel B shows the modeled concentration increases due to mining that result from the SMDN, EDGAR, and GMA 2017 emissions estimates in Madre de Dios, Peru, alongside calibration data from 2017-2019 passive-mercury samplers.[15] Panel C displays on-the-ground Hg levels against SMDN's modeled concentrations; calibration data from 2017-2019 Madre de Dios, Peru[15] (shown in B) are included alongside validation data collected from 2023-2025 Madre de Dios (by coauthors), Brazil and Colombia in 2017-2019,[38] Suriname in 2006-2007,[17] and Guyana in 2023.[16] The bottom table offers a colormap legend for each model (which mix as an RGB composite in panel B) and log concordance correlations for calibration data and validation data. 29

Figure 2-2. Mercury emissions estimates at different spatial scales. Panels A, B, and C estimate mining emissions by year for Madre de Dios, the Brazilian Amazon, and the non-Brazilian Amazon, respectively, for SMDN, EDGAR, and GMA. We include 95%-CIs for SMDN and reported uncertainties of 50% for GMA estimates. EDGAR does not report gold-mining emission uncertainties, but we include a 50% uncertainty in this plot (matching GMA's uncertainties) to clarify that numbers are not precisely known. Gold price,[50] adjusted for inflation to 2010 US dollars, is also included in each panel. Dashed lines represent national (Brazil's Forest Code and Peru's Operation Mercury) or international (Minamata Convention) policy changes and the gray box represents the 2015-2016 El Niño years. 32

Figure 2-3. Modeled mercury concentration footprints before and after regulation events. Modeled concentration footprints in Brazil's Tapajós basin (panel A) and Madre de Dios, Peru (panel B) during the five years before and after Brazil's 2012 Forest Code deregulating deforestation (panel A) and Peru's 2019-2020 Operation Mercury, an enforcement operation targeting illegal mining camps (panel B). Green shows the average concentration footprint in the five years preceding each event and red shows average concentration footprint during the five subsequent years. Red and green mix to form gradients of orange as an RG composite (mixing creates yellows). Panel A includes hatched shaded regions that show conservation and Indigenous land concessions. Panel B includes the Interoceanic highway and circles Operation Mercury's region of enforcement south of the highway bordering the Tambopata Reserve. 35

Figure 2-4. Exposure of land and people to mercury. Panel A shows percentiles of modeled mercury exposure in 2024 due to mining across the entire Amazon, in conservation concessions, in Indigenous concessions, in croplands, and in urban areas for

the SMDN model. Thresholds are marked matching where modeled concentrations are double background atmospheric Hg levels (2x 0.68 $ng\ m-3$), the state of California Office of Environmental Health Hazard Assessment (OEHHA)'s chronic exposure threshold[74] (30 $ng\ m-3$), U.S. Department of Health and Human Services Agency for Toxic Substances and Disease Registry (ATSDR)'s chronic exposure threshold[75] (300 $ng\ m-3$), and a threshold at which neurological effects have been observed from chronic exposure[73] (1400 $ng\ m-3$). Panel B shows percentiles of modeled Amazon urban resident exposure in 2001, 2013, and 2024 due to mining under the SMDN model, with the same toxicity thresholds included. Panel C shows the number of Amazon urban residents exposed to each exposure threshold in each year between 2001 and 2024. Future scenarios are bounded by a gold-price-elasticity scenario where production tracks the doubling in gold prices from 2024-2026 and a mercury-capture scenario where mining remains at 2024 levels, but all miners adopt mercury-capture technology with 80% efficiency. 38
Figure 3-1 shows the leaf sampling sites used in this study. 43
Figure 3-2 shows plant physiological changes for Gynerium sagittatum (GS) plotted in black and Cecropia peltata (CP) plotted in blue versus leaf mercury concentrations along an air-contamination gradient that includes LP (4.62 $ng\ m-3$), MDD (2.23 $ng\ m-3$), LAR (1.45 $ng\ m-3$), TAM (1.74 $ng\ m-3$), KILO (1.68 $ng\ m-3$), and CM2 (near background). Panels a-e show in order: oxygen evolving complex efficiency (proxied by the fraction of initial 2 ms fluorescence rise occurring during the first 0.3 ms), photosystem I efficiency (proxied by the fraction of fluorescence variable fluorescence occurring after 30 ms), diameter at breast height, leaf size, and chlorophyll content (proxied by SPAD measurements which combines infrared and red reflectance bands). Site level correlations (r) and Pearson one-tailed p-values of those correlations are included in each panel. The main text notes likely mercury stress for measured physiological parameters if p<0.05 for the leaf level mercury comparison (n=60 leaves) and (due to the underpowered nature of a 6-site mercury-gradient study) p<0.1 for site level average comparison; for reporting cross-species significance, the Stouffer combined p-value was required to meet those criteria. 50
Figure 3-3. Plot A displays normalized NIRv change (normalized by the average NIRv of forested pixels within 300 km) between 2005 and 2024 overlaid with modeled 5 $ng\ m-3$ mercury exposure contours for 2024 (see Chapter 2). Plot B displays estimated multiple-linear regression coefficients of normalized NIRv versus footprints for 0-15 years after modeled footprints (black) and for the non-mining control pseudo footprints (orange). ... 52
Figure 3-4. This figure shows gross primary productivity (GPP) loss in panel A and lost biomass carbon storage in panel B due to Amazon gold mining between 2001 and 2024. The impacts of direct mining deforestation are shown in black, and the impacts of mercury degradation are shown in grey. 54

Figure 3-5: This plot shows the average 2001-2024 Maximum Cumulative Water Deficit (MCWD) in South American forests with grey indicating non-forested pixels, red indicating pixels exceeding water deficits that support forests, blue indicating deficits that forests can sustain, and the blue-purple-red gradient indicating the predicted transition zone where forests transition to savanna.[104] Grey and black contours represent speculated average MCWD increases of 0.1 and 1 mm (restricted to forested areas where it was calculated) resulting from upwind reductions in transpiration from mining deforestation and mercury degradation. 56
Figure 4-1. This figure shows the sampling locations and their site names where soils, litter, and air mercury measurements were taken by authors (in orange) and prior studies[19,113] (in black). Below we include a list of the sites, the ground-level (1.75-m height) air concentrations; the above-canopy air-mercury concentrations (53 or 58-m height depending on the site); the source of total mercury (THg) measurements: either authors, Gerson et al,[19] or Szponar[113]; the source of air, soil, and litter isotopes: either authors or Szponar[113]; and whether total mercury concentrations from a neighboring deforested plot are available (from the same source as THg measurements). 61
Figure 4-2. This figure shows the air-mercury gradient between 16m and 58m (Panel A), modeled eddy diffusivities (Panel B), and net mercury flux into soils (Panel C), averaged by hour of day from continuous mercury data collected at the Los Amigos Flux tower in June 2024 and September 2024 through January 2025. Panel D and E display the average vertical mercury gradient between 16 and 58 m for different 58-m air-mercury concentrations for all times of day in Panel D and separated by day (blue) and night (orange) in panel E. 73
Figure 4-3. This figure plots the difference of $\Delta 199$ in litter versus soil, normalized by $\Delta 199$ in air. 75
Figure 4-4 displays measured versus predicted total mercury (panels A & D), $\delta 202$ (panels B & E), and $\Delta 199$ (panels C & F) for a two endmember model with air and soil uptake into leaves (panels A, B, & C) and a one endmember model with only air uptake (panels D, E, & F). In each panel, we included a pseudo-$R2$ representing the fraction of measured variance explained by the two endmember model in the given parameter. 76
Figure 4-5. **Air-concentration and soil loading impacts of emissions.** Panel A displays the fraction of emitted mercury depositing in Amazon soils, depending in which pixel the emissions occurred; black contours denote $0.25°$ grid cells where emissions exceeded, on average, $0.3\ \mathrm{kg\ km-2\ year-1}$. Panel B and C display fraction of emitted mercury absorbing into Amazon soil stores along with the modeled time (minutes) an average emitted mercury-vapor atom resides in the lowest meter of air (before either absorbing into soils or entering the free troposphere) by the hour of day (panel B) and month of the year (panel C) in which the emission occurred. 79

Figure 4-6. This figure compares the observed and modeled soil mercury gradient between 10-15 cm and 0-5 cm depths. The modeled soil mercury gradient is presented as is (panel A) and after correcting by the site's ratio of observed to modeled air-mercury concentration (panel B). The sites of Boca Colorado and Kilo tower were marked to highlight the substantial air-mercury model correction required (for Boca Colorado) and a negative mercury gradient indicating some other process is present (for Kilo). 80
Figure 4-7 plots total mercury (panel A) and Mercury $\Delta 199$ (panel B) for the baseline (10-15 cm) horizon against the relative elevation above the minimum of all pixels within 1 km. ... 82
Figure 4-8 shows the fractional loss of surficial (0-5 cm) mercury at deforested versus neighboring forested plots against the estimated number of years since deforestation. ... 85
Figure 4-9. Panel A displays measured vs modeled mercury levels at 12 forested (filled points) and 9 deforested plots (unfilled points) in Madre de Dios, Peru. The Kilo site is labeled in Panel A, to highlight the model's poor prediction accuracy at that site, reflecting the site's potential disturbance history (discussed in section 4.3.4). Panel B displays the spatial predictions of surficial (0-5 cm) soil mercury in Madre de Dios, Peru, accounting for mining enrichment (contours), depleted surface mercury due to deforestation (yellow), and the sum of topographic baseline plus enrichment minus deforestation loss (red). Note that red and orange mix to form oranges, indicating that predicted soil mercury and predicted lost surficial soil mercury due to deforestation are on the same order of magnitude. 87

Figure SI 6-1 shows the mean log squared error between measured air-mercury (Hg) levels in calibration data[15] and modeled mercury using the Spatial Mining Deforestation and Nighttime Light (SMDN) model. A vertical line of 2.49 corresponds to the decay power estimated by Carrillo-Tudela & Li[33] for Andean reference-price mineral trade. 122
Figure SI 6-2 displays the nighttime light of the most lit pixel for 7 towns in Madre de Dios, Peru, where elevated Hg or mining shops have been observed.[15,53] Previously reported urban cutoffs of 0.6 $nW\ sr - 1cm - 2$ for VIIRS[36] and 3 digital numbers for CCNL[37] are included. Axes represent Visible Infrared Imaging Radiometer Suite (VIIRS) and Consistent and Corrected Nighttime Light Dataset (CCNL). 122
Figure SI 6-3 shows the sequence of steps followed to calibrate the Spatial Mining Deforestation and Nighttime Light model. Mining site and mining town emission pixels were identified via remote sensing and combined with Lagrangian modeling outputs to produce unscaled footprints. Maximum likelihood emission scaling factors were then estimated to produce scaled concentration footprints that best reproduce on-the-ground air-mercury data. 123
Figure SI 6-4 shows the Lagrangian transport model results for Paramaribo, a Guyana mine, and Puerto Maldonado in 2006, 2018, and 2024 corresponding to the years with air-mercury measurements in validation data. 123

Figure SI 6-5 shows the above canopy (53 meters at the Tambopata flux tower and 58 meters at other sites) and below canopy (1.75 m) mercury (Hg) concentrations. A line of best fit of $Hgground$ = 0.66 $Hgabove$ - 0.13 $ng\ m-3$ is included..... 124
Figure SI 6-6 shows ERA5 and Radiosonde[209] estimates for the planetary boundary layer (PBL) height estimated four times per day at a site near Manaus, Brazil in 2014. A 1:1 line is also included. As found by Dias-Júnior et al[174] there is reasonable agreement between the two datasets for the thicker daytime boundary layer, but they are less correlated at night; however, the overall distribution remains similar across the two datasets. 125
Figure SI 6-7 displays estimated multiple-linear regression coefficients of daytime land surface temperature (over a background-mercury baseline) versus footprints for 0-15 years after modeled mercury concentration footprints (black) and for the non-mining control (orange)..... 126
Figure SI 6-8 displays the estimated impact of mercury concentrations controlling for the prior year's concentrations during times of increasing mercury concentrations (blue) and decreasing concentrations (grey), as well during increasing non-mining deforestation control (red). Each scenario is calculated by assigning pixel-year combinations to binned categorical variables for its mercury concentrations, comparing year-to-year change in normalized NIRv with change in the categorical bin variables (-1 if the previous year's bin's categorical variable, 1 in the next year's bin's categorical variable, and 0 in all other categorical variables). 126
Figure SI 6-9 plots Total mercury (panels A & B), $\Delta 199$ (panels C & D), and height above the minimum for all pixels within 1 kilometer (panels E & F) against pH (panels A, C, & E) and loss on ignition (panels B, D, & F). 127
Figure SI 6-10 plots $\Delta 201$ versus $\Delta 199$ for soil mercury at 10-15 cm depths, along with the regression line of best fit. 128
Figure SI 6-11 plots $\Delta 199$ for 1.75-m air (grey), 58-m air (black), and 0-5 cm soils (red) against air-mercury concentrations. 128
Figure SI 6-12 shows the fractional loss of soil mercury in the 5-10 cm profile (panel A) and 10-15 cm profile (panel B) at deforested versus neighboring forested plots against the estimated number of years since deforestation. 129

LIST OF TABLES

Table SI 6-1 lists the air-mercury (Hg) concentration data utilized in this study. Sample ID, country, longitude, latitude, deployment date, retrieval date, year (midpoints of deployment and retrieval dates were used for selecting the year of model comparison), average air-mercury concentrations, authors, publication date, and data use (calibration or validation) are included..... 129
Table SI 6-2 shows the estimated replacement time per cm of baseline soil mercury, along with a baseline estimate of the equilibrium residence time of the 0-5 cm surficial pool from authors' sampling sites along with prior study sites[19,113]..... 133
Table SI 6-3 compiles particulate mercury, total suspended solids, and mercury concentrations in suspended particulates across wet season and dry season measurements reported by prior Amazon studies. Ambiguous shoulder season measurements[198] were reported as wet season for the purpose of comparison. For studies[20] where only total particulate mercury and total suspended solid concentrations were reported, the particulate mercury concentration within suspended solids were computed by dividing the former by the latter with quadrature fractional error propagation. When only total suspended solid and mercury concentrations within suspended solid data were available,[201] total river particulate mercury concentrations were calculated via multiplication but errors were not computed on the result as they would overestimate the study's measured sample error in river particulate mercury concentrations. For a blackwater study[200] where multiple depth profiles were reported, we included only 5-6 meter depth samples from the center of the river, because we believe that they are more representative of average water concentrations than organic rich surficial water. 134

Chapter 1. Introduction

1.1. Background

Since the industrial revolution, anthropogenic mercury emissions have driven an 11-fold increase in atmospheric mercury concentrations.[1] As a biomagnifying neurotoxin in its methylated form, mercury has drawn international scrutiny, culminating in the 2013 Minamata Convention on Mercury to mitigate global emissions. With 153 signatory countries, the Convention mandated mercury emission reductions and entered force in 2017. However, mercury emissions from informal gold mining have proven particularly challenging to address, and this mining now comprises 37% of global emissions.[2] Incentivized by gold demand in wealthy countries,[3] this mining impacts ecosystems and communities where mining occurs, primarily in the tropics and Global South.

Informal gold miners typically add liquid elemental mercury to fine sediments, where it combines with gold particles to form identifiable clumps of amalgam that can be visually separated. For each gram of gold extracted, miners typically require 10-25 grams of mercury if mixed with raw crushed sediment or 1-3 grams if added after pre-concentration.[4] Miners then burn off residual elemental mercury from the gold amalgam, generating mercury vapor near mining sites and at urban gold shops during the smelting process.[5] This type of informal mining is often referred to as artisanal small-scale gold mining (ASGM). However, in most locations the practice does not meet the criteria for small-scale,[6] with mine tailings extending over thousands of square kilometers. Following Verbrugge & Besmanos,[6] we instead refer to this sector as informal gold mining to highlight its position outside formal economies and distinguish it from regulated industrial operations.

An estimated 45% of mercury used in informal gold mining vaporizes into the atmosphere,[7] although this number likely varies by region and mining practice. We studied the fate and impacts of atmospheric mercury emissions from Amazon gold mining, which account for 40% of mercury emissions associated with informal gold mining globally.[2] The Amazon—in this paper referring to the Amazon rainforest region, along with deforested regions that used to be a part of the rainforest—is a vital yet deteriorating carbon sink,[8] a biodiversity hotspot under threat from deforestation and forest degradation,[9] and a provider of ecosystem services essential for traditional Amazon livelihoods that are becoming less secure in a changing environment.[10]

Atmospheric mercury emissions can elevate air-mercury concentrations outside of urban gold shops[11–13] and across large distances in Amazon gold-mining regions.[11,14–17] Past research[18,19] has correlated—but without a dose-response relationship—elevated leaf-

mercury concentrations to gold-mining proximity. However, it remains unclear whether atmospheric loading downwind of mining explains the observed[19] variation in soil-mercury levels or if it is a non-negligible driver of the mercury observed in birds, fish, crops, meat, and human hair[19–22] in mining regions. Other than a few urban mining districts where measured air concentrations exceed toxicity thresholds,[11–13] it remains unclear if atmospheric mercury loading into ecosystems presents a health risk to plants, soil microbiomes, animals, fish, or people. Even less is known about the spatial profile of impacts or long-term fate of emitted mercury, presenting challenges for non-profits, governments, and international bodies aiming to target the most impacted areas and mitigate mercury's harmful effects.

1.2. Dissertation Overview

This thesis combines field measurements of air, plant, and soil in the heavily mined Madre de Dios region in the Peruvian Amazon with remote sensing and atmospheric modeling to estimate the impact of mercury emissions at the regional and Amazon scales.

Chapter 2 investigates the emission sites and downwind footprints from Amazon gold mining. This chapter builds a high-resolution model that can accurately predict where emissions occur, both from mining sites and gold shops in nearby urban centers, as well as the exposure in nearby population centers and downwind ecosystems. Prior studies have considered emissions and downwind concentration footprints in isolation, estimating the former with bottom-up inventories of mining activity and the latter with on-the-ground measurements of air-mercury at specific sites. Recognizing that emissions and downwind footprints are highly linked, we jointly estimated them via Lagrangian particle modeling. Using an extensive network of air-mercury measurements from prior work in the Madre de Dios region of the Peruvian Amazon, existing remote sensing analysis of mining site locations, and Lagrangian transport, we calibrated a model for the rate of emission per mined area and the resulting concentration downwind. We verified the model across a limited air-mercury dataset from other parts of the Amazon and used the model to understand the socio-economic drivers of gold mining and the health exposure in mining regions. This chapter (with some introductory components moved into Chapter 1) is copied from a submitted manuscript:

Ruhm R.; Chaboteaux E.; Cosio E. G.; Cruz Chino R. S.; Janssen S. E.; Plunkett S. A.; Ramos Chang E.; Tate M. T.; Turner A. J.; Neumann R. B. A High-Resolution Approach to Estimate Gold-Mining Mercury Emissions and Their Downwind Concentration Footprints, 2026.

Chapter 3 addresses the plant health impacts of mercury downwind from Amazon gold mining. Mercury toxicity has been previously observed in aquatic plants in contaminated

water, terrestrial plants in contaminated soils, and grasses in highly contaminated air; this chapter evaluates if effects are observed at the low-to-moderate air-concentrations experienced by Amazon forests across gold mining regions. We sampled on-the-ground pioneer species for mercury levels and a variety of plant health metrics, allowing us to evaluate whether an effect occurs and, if so, the physiological mechanism of that effect. Then, using satellite remote sensing, we quantified the scale of aggregated forest productivity impacts across the Amazon. Based on these productivity declines, we calculated a resulting decline of regional carbon stock, potential hydrologic feedback loops leading to further forest die-off, and other speculated regional and global impacts. This chapter reveals a host of potential socio-ecological impacts resulting from this lost productivity, with a broader social cost valuation on par with the total value of gold produced. This research corresponds to a manuscript in prep:

Ruhm R.; Chaboteaux E.; Cosio E. G.; Cruz Chino R. S.; Flucke L. E.; Janssen S. E.; Ramos Chang E.; Tate M. T.; Turner A. J.; Zwieniecki M.; Neumann R. B. Mercury Emissions from Amazon Gold Mining Reduce Forest Productivity and Carbon Stocks. In prep.

Chapter 4 considers the fluxes in and out of Madre de Dios soils with implications for the broader Amazon. Prior research has identified leaf uptake as an important input of atmospheric mercury into Amazon soils, especially in contaminated mining regions. However, past work has not comprehensively characterized Amazon soil fluxes, explained the observed variation in soil mercury concentrations, or described the different long-term fates of soil mercury. This chapter estimates additional input and output fluxes, including direct dry deposition from air to soils, evasion back into air, and erosion into waterways. Using these estimated fluxes, Chapter 4 describes the fate of Amazon emissions including the fraction of atmospheric mercury emissions that enters regional ecosystems, the fraction of soil mercury inputs that ultimately erode into waterways (with implications for aquatic ecosystems), and the additional mercury emissions associated with Amazon deforestation. Chapter 4 material corresponds to two publications that are in the drafting stage (corresponding to sections 4.3.1-4.3.3 on mercury loading from air to soil and 4.3.4-4.3.8 on predicting the soil-mercury accumulation and its long-term fate); the research presented in this chapter involved collaborators: Grace Armstrong, Elena Chaboteaux, Eric Cosio, Rudi Cruz Chino, Laura Flucke, Sarah Janssen, Michael Tate, Thomas Wang, and Rebecca Neumann.

Chapter 5 synthesizes the dissertation's main results, highlighting key takeaways that can be applied to future research, policy, and community action. The dissertation closes by situating this work in theories of societal change and proposes future types of research that can reduce the harm posed by gold mining.

1.3. Positionality Statement

Before shifting to empirical results, I want to situate my role as a researcher and the context where research was conducted.

I am a white settler living and working on Coast Salish and Duwamish ancestral lands while completing my PhD at the University of Washington. This work has focused on the Amazon rainforest, where I have no ancestral connection and have only visited for three brief field campaigns. In recognizing the history of extractive research conducted by western researchers in and around communities in the Global South, I have aimed to apply critical (Lave et al., 2018) and anti-colonial (Liboiron, 2021) methodologies in conducting natural science research that grapples with global institutions of power, extractive industry, and the role of research. My PhD research has aimed to build multidisciplinary collaboration that addresses multiple facets that influence mercury emissions from ASGM.

This research has only been possible through an extensive collaboration with PUCP and ACCA for on-the-ground logistics, understanding the local landscapes, and identifying relevant research questions. At the same time, there are many stakeholder communities, organizations, and Indigenous communities in the region with whom we've built limited or no relationship; not having built deep relationships with these groups biases our research methods, methodologies, and values. We have followed guidance from the work of CINCIA, a non-profit in Madre de Dios that conducts research and works with local communities around the mercury contamination from gold mines. We seek to cohere research based on theories of change[23] given the on-the-ground realities of gold mining.

By building and sharing emission, footprint, and soil-loading maps with local stakeholders, I hope this work can offer insights that can help inform mercury risk assessments and advisories that ultimately assist communities in adapting livelihoods near mercury contamination. I hope this research can extend beyond simply adding to the body of findings that gold extraction harms ecosystem and human health, by supporting local harm mitigation and global movements for change. Through relationships built with Amazon environmental organizations, we intend to share risk maps in an appropriate manner to support communities in minimizing exposure pathways. We connect the highly visible role of miners in constituting the informal gold-mining industry with global gold-consumption and climate drivers that highlight the shared global responsibility in addressing gold mining's harms. On the other hand, we connect the local and regional scale of visible mining impacts with the less understood global impacts on the carbon and mercury cycles to highlight the importance of global stewardship on what's often perceived as a regional issue.

1.4. Acknowledgements

I would like to thank everyone who has supported me on my PhD journey. I have been fortunate to connect with and learn from an academic community from multiple disciplines and countries. The project was only made possible in collaboration with Peruvian colleagues. Eric Cosio helped formulate the project's inception and offered feedback along the way. Dr. Cosio's lab, including Esteban Ramos Chang, Rudi Cruz, and Manuel Marca Zevallas, supported immensely in field work; they invited us into the team of researchers utilizing flux towers across the Peruvian Amazon, shared their infrastructure and expertise in working on said towers, and offered much time and patience during the setup and maintenance of the continuous mercury analyzer installed at the Los Amigos flux tower. Elena Chaboteaux helped design the plant sampling approach, identified appropriate species and sites for sampling, joined for multiple sampling trips, and supported with issues in field deployments when we were away from the Los Amigos station. In addition to these collaborations with La Pontificia Universidad Católica del Perú and Climate Corridors, we received logistical support from Andes Amazon Fund, La Asociación para la Conservación de la Cuenca Amazonica (ACCA), and the Center for Amazonian Scientific Innovation (CINCIA) in conducting this work. The Promotores de Conservación guided us upriver into the Los Amigos concession across three field campaigns, helped identify sampling sites, and supported in sampling air, foliage, and soils of these pristine forests.

This work has also been supported by colleagues and mentors outside of Peru. I owe much gratitude to Jackie Gerson and Natalie Szponar, who built an extensive mercury dataset of air, foliage, leaf litter, and soil in Madre de Dios, which augmented our own collection and enabled the findings in chapters 2 and 4. Maciej Zwieniecki offered feedback and shared his plant physiological expertise that helped shape our plant sampling methodology and interpretation of results; his team also lent us a Licor 6400 for photosynthetic analysis and measured carbohydrate levels in our branch samples.

The USGS M3 lab—including Sarah Janssen, Michael Tate, Grace Armstrong, Bryce Cook, Laura Flucke, Tylor Rosera, and Thomas Wang—graciously invited me into their lab, trained me in mercury analysis, and hosted me as I analyzed air, foliage, and soil samples. Lab members generously offered their time after I departed the Madison lab to analyze samples for mercury isotopes, complete remaining associated sample preparation steps, and analyze soil samples for methylmercury. Sarah and Mike also offered extensive feedback along the way, including proposing the isotopic sampling plan that was critical for Chapter 4's analysis.

Dan Jaffe generously donated a Tekran 2537 mercury analyzer, along with supplemental equipment, and supported technical hurdles along the way. Lucas Hawkins offered extensive technical support with the mercury analyzer issues and donated a second Tekran 2537 mercury analyzer for future research. Soo-Hyung Kim's lab generously lent a SPAD chlorophyll meter and supplemental Licor 6400 equipment to support field campaigns. Shannon Plunkett and Elena Chaboteaux shared unpublished air and soil mercury measurements for inclusion in this thesis.

Members of the Neumann, Butman, Turner, and Shah labs have offered feedback on research along the way. Alex Turner helped develop the satellite greenness and atmospheric modeling methodology. Sameer Shah has supported me in incorporating methods across disciplines and thinking through environmental justice dimensions of this work. Ben Miller and Joel Eklof traveled to Peru to support in field campaigns.

Becca Neumann launched the project as PI and has mentored me through all the challenges along the way. She exemplifies what it means to conduct rigorous scientific research, organize field campaigns to collect compelling datasets, and hone scientific writing into manuscripts. She has supported me in incorporating diverse methods, both within and outside her own expertise. What started as a seemingly outlandish idea of installing a continuous mercury analyzer on a remote Amazon flux tower turned into a key part of the work; along the way she helped me learn the scientific and field sampling skills to turn an idea into rigorous science. Becca has generously and patiently offered her time throughout my PhD as I've developed my strengths, worked on my weaknesses, and built a PhD that I feel proud of.

Finally, my family, community, and professional mentors have supported me in growing into the person and scholar I am becoming. My winding academic and professional journey moved from abstract mathematics to software development to econometric research to water treatment to mercury research. The personal and activist connections built over the past decade shaped the anti-colonial approach I have striven to bring to Global South mercury contamination research. I want to thank Clarita Lefthand-Begay for inviting me into a UW network of Indigenous scholars and allies supporting Native research in academia. My sibling William has shaped me as an activist and in how I conceive of liberation, and my parents Chris and Maryanna have supported me throughout my life's journey to get here. My partner Shay has seen me through the emotional ups and downs of the PhD, has shared in the excitement for the new knowledge built along the way and the grief of the harm mercury findings often pose, and has been my home to return to after the long field trips to Peru, lab trips to Madison, and the other PhD travels. Thank you to everyone past, present, and future who has shaped my journey.

This research was funded by the UW Global Innovation Fund, the UW Population Health Initiative, and the HKS GEM Incubation Fund. My PhD has been funded by the NSF Graduate Research Fellowship Program, the UW College of Engineering Dean's Fellowship, and the NSF-funded Future Rivers Traineeship through Earth Lab. Google Earth Engine was used extensively for coding and data analysis; Earth Engine generously uplifted my account to partner tier status to support larger computation tasks involved in the research. Claude versions 4 and 5 were used for copy editing and to find additional literature sources relevant to this work.

Chapter 2. A High-Resolution Approach to Estimate Gold-Mining Mercury Emissions and Their Downwind Concentration Footprints

2.1. Introduction

These atmospheric emissions from Amazon gold mining elevate air-mercury concentrations across surrounding regions,[11,14–17] with urban gold-shop districts reaching toxic concentrations.[11–13] More broadly in Amazon mining regions, elevated mercury concentrations have been observed in birds, fish, crops, and meat,[19–21] and human-hair samples have frequently exceeded World Health Organization mercury thresholds.[22] However, the full spatial extent of mercury contamination in the Amazon is unknown due to the challenges associated with quantifying informal gold mining activity and sampling at remote sites. Such knowledge is needed to fully assess the human and ecosystem impacts of emitted mercury and to design interventions that minimize negative effects.

The Global Mercury Assessments[2,7] (GMA) and the Emissions Dataset for Global Atmospheric Research[24] (EDGAR) are the leading global mercury-emission inventories. However, these two products, which depend on country-level proxies for gold mining, have high uncertainties and exist at spatial resolutions (0.25° and 0.1°, or approximately 27 and 11 km, respectively) that are too coarse for assessing human and ecosystem impacts. To overcome these limitations, we harnessed recent advances in satellite image classification[25] and air-mercury measurement[26] to model how vaporized mercury from informal gold mining travels across Amazon landscapes with an annual time step and 1-km spatial resolution.

The model, called the Spatial Mining Deforestation and Nighttime Light (SMDN) model, uses remote sensing of mining deforestation to identify emission sites, Lagrangian transport to translate emissions to concentration footprints, and on-the-ground air mercury measurements to back-calibrate emissions. Here we use the model to uncover patterns in emissions from rural mining sites and gold shops, identify trends in emissions over time and space, and quantify toxic exposure levels for humans and ecosystems.

2.1.1. Graphical Abstract

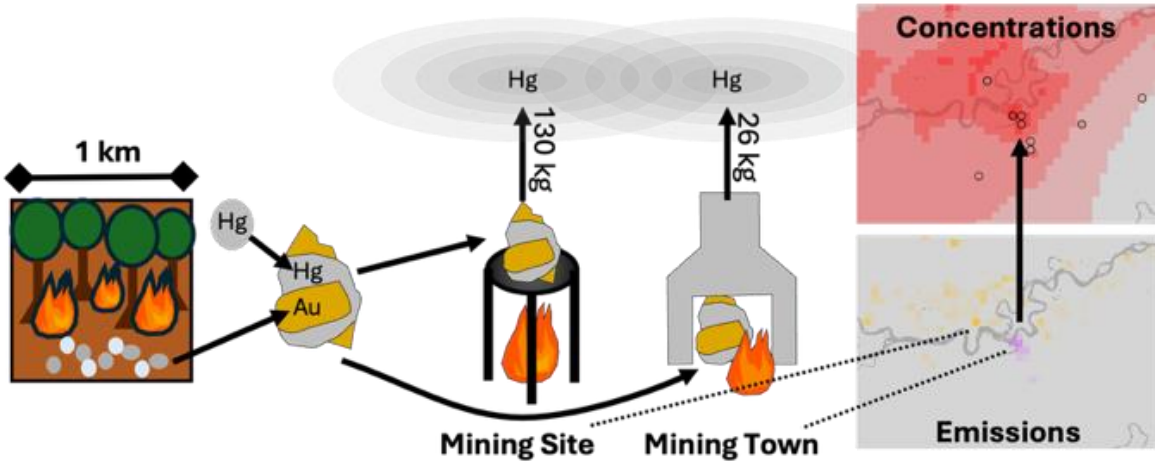

2.2. Methods and Materials

2.2.1. Gold mining identification

We used Amazon Mining Watch mining polygons[25] to identify accumulated mining area, as of 2025, ensuring complete coverage of mined area through 2024. We consider polygons that lie closer to gold deposits[27] than to known industrial mines[28] as informal gold mining and exclude the rest. This process removed 4% of the total mined area (representing probable industrial mining sites) from consideration in our analysis. Using Google Earth Engine,[29] we overlaid annual deforestation[30] (2001-2024, 30-m resolution) to identify newly mined pixels within these polygons each year, and aggregated the resulting annual mined area to a 1-kilometer scale for computational tractability.

2.2.2. Model Parameterization

Following the observation in Cordy et al[5] that mercury is vaporized from gold amalgams both at mining sites and in mining shops in nearby towns, we modeled emissions at a 1000-m, 2-dimensional pixel X each year according to:

$$\text{Emissions}(\text{X}, \text{Year}) = E_{site} * \delta_{site}(\text{X}, \text{Year}) + E_{urban} * \rho_{\text{urban}}(\text{X}, \text{Year})$$

where E_{site} and E_{urban} are constants representing the mining-site and urban-component of emissions (kg $\text{year}^{-1}\text{km}^{-2}$), and δ_{site} is the (dimensionless) fraction of a pixel deforested for mining in the given year. The urban component of emissions is distributed according to a gravity model[31]:

$$\rho_{\text{urban}}(X, \text{Year}) = \int_{X'} \delta_{site}(X', \text{Year}) * \frac{\text{NightLight}(X, \text{Year})/D(X, X')^{\text{decay}}}{\int_{X''} \text{NightLight}(X'', \text{Year})/D(X'', X')^{\text{decay}}}$$

where nighttime light proxies for urbanization, D is Euclidean distance, X is the target pixel, X' is a nearby mining pixel (within 200 km of X), and X'' is any other pixel within 200 km of X' with potential nighttime light.[32] We integrated over mining pixels X' to

aggregate urban emissions at X, normalizing the urban component of emissions from X' across all urban pixels X'' that may receive it. We applied a gravity decay coefficient of 2.49 from past research on the Andean trade in mineral reference-price goods[33] (of which gold is an example). Supporting information (SI) section 1 and Figure SI 6-1 consider the sensitivity of the model to this exponent.

Only pixels outside known mining polygons[25] were considered for E_{urban}, preventing collinear downwind concentration footprints and distinguishing mining towns from electrified mining camps. We used Visible Infrared Imaging Radiometer Suite (VIIRS)[34] nighttime light after 2013 and Consistent and Corrected Nighttime Light Dataset (CCNL) from the Defense Meteorological Satellite Program Operational Linescan System (DMSP-OLS)[35] in prior years, restricting urban emissions to pixels exceeding established thresholds: 0.6 $\mathrm{nW\ sr^{-1}cm^{-2}}$ for VIIRS[36] and 3 digital numbers (DN) for CCNL[37] (see Figure SI 6-2 for threshold validation).

2.2.3. Atmospheric Transport

We translated modeled emissions to concentration footprints using Lagrangian transport modeling within the planetary boundary layer (PBL). This framework estimates Lagrangian plumes—downwind concentration ($\mathrm{ng\ m^{-3}}$) per emission ($\mathrm{kg\ km^{-2}year^{-1}}$)—at medium-field distances of 1 to 60 kilometers downwind but ignores free tropospheric (long range) and ground-level (near-field) transport. Particles were advected for 24 hours. Vertical dispersion was calculated using surface similarity theory during initial hours until dispersion fully mixes plumes into the planetary boundary layer. Once fully mixed in the boundary layer, particles escape into the free troposphere only during turbulent deep convection events. See SI section 6.1.2 for the full Lagrangian transport model description and SI section 6.1.3 for the associated uncertainty.

2.2.4. Model Calibration

We applied these Lagrangian plumes as a spatially variable convolution on modeled emissions to estimate downwind concentration footprints (see Figure SI 6-3 for a conceptual diagram of model calibration steps):

$$\mathrm{Hg_{mining}(X, Year)} = (E_{\mathrm{site}} * \delta_{\mathrm{site}}(\mathrm{X, Year}) + E_{\mathrm{urban}} * \rho_{\mathrm{urban}}(\mathrm{X, Year})) \otimes \mathrm{Plume(X, Year)}$$

In this equation, X is a 1000-m 2-dimensional pixel; plume is the Lagrangian plume ($\mathrm{ng\ m^{-3}}$ per $\mathrm{kg\ year^{-1}}$), which depends on pixel-location and year; background mercury levels are a priori not known (see Figure **2-1** for translation from emissions to downwind concentration impact); and regression coefficients E_{site} ($\mathrm{kg\ year^{-1}}$) and E_{urban} ($\mathrm{kg\ year^{-1}}$) are modeled as constant emission rates per unscaled emission parameters δ_{site} and ρ_{urban} (unitless). We then estimated modeled concentrations, $\mathrm{Hg_{modeled}}$ = $\mathrm{Hg_{mining}}$ + $\mathrm{Hg_{background}}$, with a constant average background mercury concentration (discussed at the end of this subsection). We use a log-likelihood estimator to minimize the least squared error between log-observed concentrations and log-modeled concentrations:

$$\mathrm{LE} \propto \exp\left(-\frac{\sum(\log(\mathrm{Hg_{obs}})-\log(\mathrm{Hg_{modeled}}))^2}{2*\sum(\log(\mathrm{Hg_{obs}})-\log(\mathrm{Hg_{mle}}))^2*\frac{1}{n-3}}\right).$$

where $\mathrm{Hg}_{\mathrm{obs}}$ is observed air-mercury concentration. The maximum likelihood mercury concentration model, $\mathrm{Hg}_{\mathrm{mle}}$, is estimated by minimizing log least squared errors (the numerator of the exponent in the LE expression). This model estimates the mining-site emission coefficient, E_{site}; the urban emission coefficient, E_{urban}; and background atmospheric mercury. This log transformation prioritizes fractional error and reduces the outsized influence of high-mercury observations near emission sites.

Calibration data were collected in Madre de Dios, Peru between 2017 and 2019 by Szponar et al.[15] Validation data were collected in Peru between 2023 and 2025 by authors (see section 2.2.7 for sampling and analysis methodology), Brazil and Colombia between 2017 and 2019,[38] Suriname between 2006 and 2007,[17] and Guyana in 2023.[16] Point source emissions elevate nearby (<1-kilometer distance) air concentrations more than is captured by SMDN's 1-kilometer resolution model. To minimize regression bias from elevated near-field observations, we excluded measurements within 1 km of the highest sampled concentration of known mining towns: Puerto Maldonado, Laberinto, Mazuko, Guacamayo, Boca Colorado, and Libertad, Peru;[15] a Guyana mining camp;[16] and Paramaribo, Suriname.[17]

We applied a median aggregation across measurements within the same 1-km pixel to match SMDN's resolution. This averaging yielded 82 data points for calibration and 19 for validation. For Madre de Dios and other southern hemisphere sites, we used a calibrated background Hg level of 0.68 (CI: [0.49, 0.94]) $\mathrm{ng\ m^{-3}}$. However, atmospheric transport between hemispheres occurs on the order of months, and deposition fluxes operate at a similar timescale, which leads to different background levels in the two hemispheres. Therefore, for northern hemisphere sites in Suriname and Guyana, we used a higher background of 1.4 $\mathrm{ng\ m^{-3}}$, which was measured in Suriname.[17]

2.2.5. Uncertainty estimation

We calculated 95% confidence intervals where $\log(\mathrm{MLE}) - \log(\mathrm{LE}) < 3.84/2$ (Wilks' theorem[39]). However, random error represents only part of the total model uncertainty, and systematic errors in ERA5 parameters and Lagrangian plume modeling are quantified in SI section 6.1.3. At the kilometer scale, emission uncertainties are particularly high (see SI section 6.1.4), and SMDN entirely fails to capture hard-rock informal gold mining that often occurs in mountainous regions and targets dense gold veins rather than dispersed alluvial deposits (thereby avoiding widespread deforestation). SMDN similarly fails to account for mining of sediment dredged from the bottom of active rivers and sandbars, although this mining may be spatially correlated with nearby floodplain mining which does disturb forests and produce mining scars seen by SMDN.

2.2.6. Mining Concentration Impact Analysis

We calculated the probability density functions of the entire Amazon, Indigenous, conservation, croplands, and urban lands exceeding mercury exposure thresholds. For the Amazon's 20.9 million urban residents[40] (held fixed across years due to data availability) we proxied population density by nighttime light.[41] To correct for SMDN's

underestimation near point sources, we perturbed modeled exposure probability density functions (PDFs) by the log residuals between modeled and measured concentrations across 139 disaggregated field measurements. We restricted to residuals from urban centers (VIIRS > 0.6 $\mathrm{nW\ sr^{-1}cm^{-2}}$ after 2013[36] and CCNL > 3 DN before 2012[37]) for urban land analysis, restricted to non-urban residuals for other land types, and weighted residual resampling by nighttime light for urban-resident analysis.

2.2.7. Passive Mercury Sampling

We deployed passive air samplers (MerPAS©, Tekran Instruments Corp.) between 2023 and 2025 in Madre de Dios, Peru. These samplers sorb gaseous elemental Hg onto ~0.6 g of sulfur-activated carbon granules housed in a permeable membrane within inverted jars.[26] Samplers were deployed in duplicate at a 1.75 m height at sites listed in Table SI 6-1. Sampling rates for the MerPAS yellow and white jar models were calculated using a diffusion rate adjustment from average temperature and wind speed[42]; for this calculation, we used ERA5 10-m wind and 2-m temperatures averaged over the deployment period. Following deployment, activated carbon substrates were thermally desorbed using a stepwise heating program to 800° C for 2.5 hours using a dual furnace system.[43] Volatilized mercury was trapped in a 40% reverse aqua regia (3 nitric acid: 1 hydrochloric acid) solution. Dissolved mercury concentrations were then measured using U.S. Environmental Protection Agency Method 1631[44] using an automated analyzer (Brooks Rand, MERX-T). Coal fly ash reference material (National Institute of Standards and Technology [NIST] 2691) was run every 5 samples, and each run was accurate within 15%. Activated carbon blanks (MerPAS raw material) were run every 10 samples and one method blank was run; the total mass of desorbed mercury was less than 5% that of field samplers.

2.3. Results and Discussion

2.3.1. Model optimization, accuracy, and uncertainty

Our compiled air-mercury concentration dataset[15–17,38] includes mercury levels ranging from background in remote sites (approximately 0.68 $\mathrm{ng\ m^{-3}}$) to highly elevated levels in urban environments (35,000 $\mathrm{ng\ m^{-3}}$). By minimizing mean squared log-error between modeled downwind concentrations and measured atmospheric mercury levels used for calibration[15] from Madre de Dios (between 2017 and 2019), we estimated a constant area-based mercury emission rate of 156 kg per $\mathrm{km^2}$ of mining deforestation (95% confidence interval [CI]: [120, 197]) with 83% of emissions (95% CI: [77%, 88%]) occurring at mining sites and 17% occurring in nearby urban areas (see Figure **2-1**a). This result quantifies prior qualitative evidence[45] that mercury is vaporized at both rural mining sites and urban areas. The model also suggests that a constant emission rate per area mined closely estimates measured downwind concentrations, meaning that any variability in emission rates (see SI section 6.1.4) among point

locations is averaged out over the spatial scale relevant for Lagrangian plume modeling (i.e., multiple kilometers).

SMDN concentration footprints predict observed mercury concentrations in Madre de Dios substantially better than existing inventories with a log concordance correlation of 0.79, compared to 0.00 and 0.08 for EDGAR and GMA, respectively (see Figure **2-1**b and Figure **2-1**c). When observations are aggregated to the kilometer scale, SMDN's log concordance correlation improves to 0.85, suggesting that unresolved fine-resolution variability accounts for 30% of residual variance. Model performance was lower but still informative (log concordance correlation of 0.45) when validated against more recent Peruvian measurements (collected by authors) and across limited air-mercury data from Suriname,[17] Guyana,[16] Colombia, and Brazil[38] as seen in Figure **2-1**c. Chang & Hanna[46] suggest that good atmospheric models should predict true concentrations within a factor of 2 at least 50% of the time; SMDN meets the factor-of-2 criterion 83% of the time in calibration data and 79% of the time in limited validation data. Altogether, SMDN appears to be a robust model where data are available.

Confidence in SMDN's accuracy varies across time and space, as well as between concentrations and emissions. Emission confidence is low at the kilometer-scale (see SI section 6.1.4), but modeled concentrations, which smooth emissions via Lagrangian transport, appear to closely estimate measured concentrations. At a regional scale, confidence in emissions estimates and modeled concentrations is highest in Madre de Dios, Peru, where there is extensive calibration data between 2017 and 2019[15]; regional accuracy is supported by the authors' measurements between 2023 and 2025, validating the model's extendibility over time. Concentration-map accuracy is more difficult to assess elsewhere in the Amazon where only 4 non-Peruvian validation points were included from transects extending from a Guyana mining camp (2 points) and the mining district of Paramaribo, Suriname (2 points); the remaining non-Peruvian sampling locations were remote control sites. As was seen at the kilometer scale, confidence in SMDN's emissions inventories remains lower than that of concentrations due to additional uncertainties introduced by Lagrangian inverse modeling (see SI section 6.1.3).

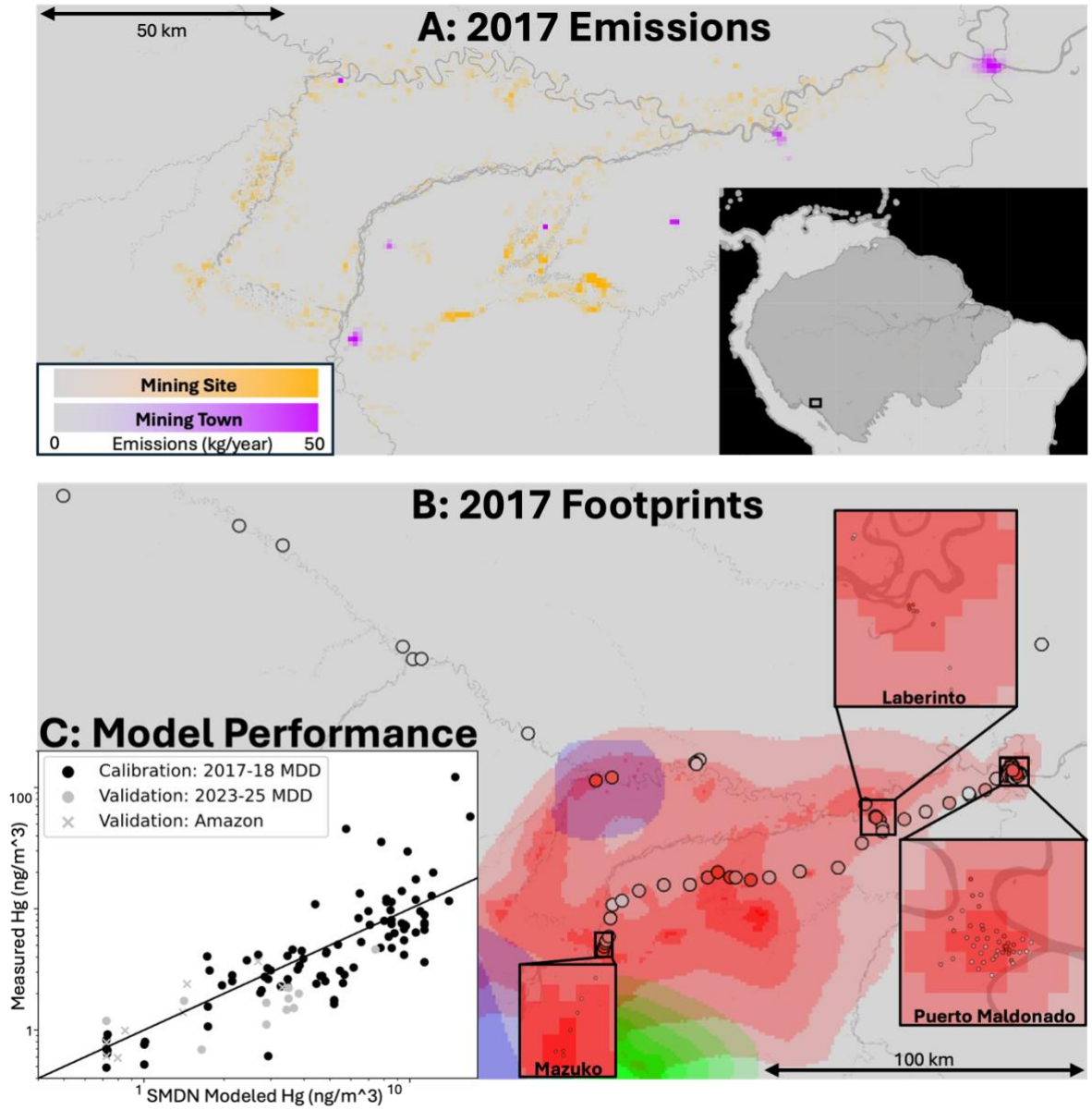

Hg ($\frac{ng}{m^3}$) = Background (0.68) +	0.5-1	1-2	2-4	4-8	8-16	>16	Calibration Log Conc Correlation	Validation Log Conc Correlation
On-the-ground								
SMDN (1 km scale)							0.79	0.45
EDGAR (0.1° scale ~ 11 km)						N/A	0.00	0.24
GMA (0.25° scale ~ 27 km)			N/A	N/A	N/A	N/A	0.07	0.34

Figure 2-1. Mercury emissions and concentration map for Madre de Dios, Peru. *Panel A displays modeled 2017 mercury emissions using the mining deforestation emissions model in Madre de Dios, Peru separated by mining site emissions (gold) and mining town emissions (purple). Panel B shows the modeled concentration increases due to mining that result from the SMDN, EDGAR, and GMA 2017 emissions estimates in Madre de Dios, Peru, alongside calibration data from 2017-2019 passive-mercury samplers.[15] Panel C displays on-the-ground Hg levels against SMDN's modeled concentrations; calibration data from 2017-2019 Madre de Dios, Peru[15] (shown in B) are included alongside validation data collected from 2023-2025 Madre de Dios (by coauthors), Brazil and Colombia in 2017-2019,[38] Suriname in 2006-2007,[17] and Guyana in 2023.[16] The bottom table offers a colormap legend for each model (which mix as an RGB composite in panel B) and log concordance correlations for calibration data and validation data.*

2.3.2. Comparing SMDN Emissions with Existing Inventories

Gold-mining emissions inventories are of particular interest for estimating mercury budgets and the global mercury cycle. EDGAR and GMA are the leading gridded inventories, relying on mining-location data and mining-activity proxies[2,47] to estimate informal gold production and associated mercury emissions. They were developed primarily for country-level estimation, and therefore their national and international totals may be more reliable than their gridded and regional spatial allocations. However, since informal gold production is often unreported, their accuracy at all scales remains uncertain. GMA estimates, based on expert opinion, that its inventories have an uncertainty of 50%, while EDGAR states that its gold-mining emission inventories carry too much uncertainty to report reliably. SMDN overcomes many of the shortcomings of the two existing inventories. It uses remote-sensing data to identify mining rather than unreliable mining-activity estimators and harnesses on-the-ground mercury measurements to estimate emissions, while providing more robust uncertainty estimation. Below we compare SMDN to EDGAR and GMA at regional, country, and Amazon-basin scales.

At the regional scale, in Madre de Dios, Peru, both existing inventories predict near-zero emissions despite well-documented mercury contamination from mining[13,15] (Figure **2-2**a). SMDN in contrast estimates an increasing trend in emissions over time, roughly following the price of gold, with periodic dips and plateaus that align with an El Niño event and the Minamata Convention; these trends are discussed further in section 2.3.3. SMDN performs well in Madre de Dios, because it identifies emissions from satellite data and utilizes an extensive regional calibration dataset. SMDN even offers emission information down to a 1-km scale which is unavailable at the coarser and highly uncertain gridded datasets for EDGAR (0.1°) and GMA (0.25°).

At the scale of the Brazilian Amazon, SMDN's emissions estimates agree with those of GMA and EDGAR prior to 2015 but exceed EDGAR in later years (Figure **2-2**b). EDGAR estimates a decrease in mercury emissions after 2015 even though gold prices tended to increase over this period. The divergence between SMDN and EDGAR in these later years could reflect the challenges, tradeoffs, and potential inaccuracies inherent in EDGAR's effort to interpolate and extrapolate sparsely available inventories across all years. After 2015, no inventories estimated Brazilian emissions for individual years, meaning that EDGAR was forced to interpolate using an average estimate[48] and extrapolate using imprecise proxies.[47] Because SMDN scales emissions with newly mined area, it offers a temporally consistent estimate grounded in the reality of gold mining, assuming that gold production rates per mined area and mercury-to-gold ratios in amalgam remain relatively constant over time. This analysis suggests that SMDN may offer an improvement over existing inventories, particularly when extrapolating across years, even at the country level where these existing inventories perform best.

Across the non-Brazilian Amazon, SMDN estimates lower emissions than EDGAR and GMA (Figure **2-2**c). With limited external validation data, it is difficult to ascertain whether these differences represent a bias in SMDN, a bias in existing inventories, or both. The lower estimate from SMDN could be explained by SMDN's failure to account for mercury emissions from hard-rock informal gold mining operations; hard-rock mining tends to occur in mountainous terrain and could be accounted for by GMA and EDGAR in the Guiana highlands or Andean foothills (in the Amazon). Alternatively, these existing inventories may misattribute hard-rock mining deeper in the Andes to the Amazon region due to their imprecise spatial proxies. Furthermore, SMDN's lower estimate could be correct if emissions scale with the number of miners. SMDN estimates that 52% of all Amazon mining emissions occur in Brazil, and Brazil houses 56% of the Amazon's informal miners.[49] EDGAR and GMA, in contrast, estimate that Brazil is responsible for 17% and 24%, respectively, of the Amazon's mercury emissions. It is contested whether mining production scales with the number of miners due to potential mining technological differences across countries that impact productivity per miner.[49] However, the fact that SMDN's modeled emissions, which are proportional to area mined, scale with the number of miners suggests mined area per miner is relatively constant across the Amazon; this result undermines the proposed explanation that technological development differences could cause emissions and miners to be disconnected.

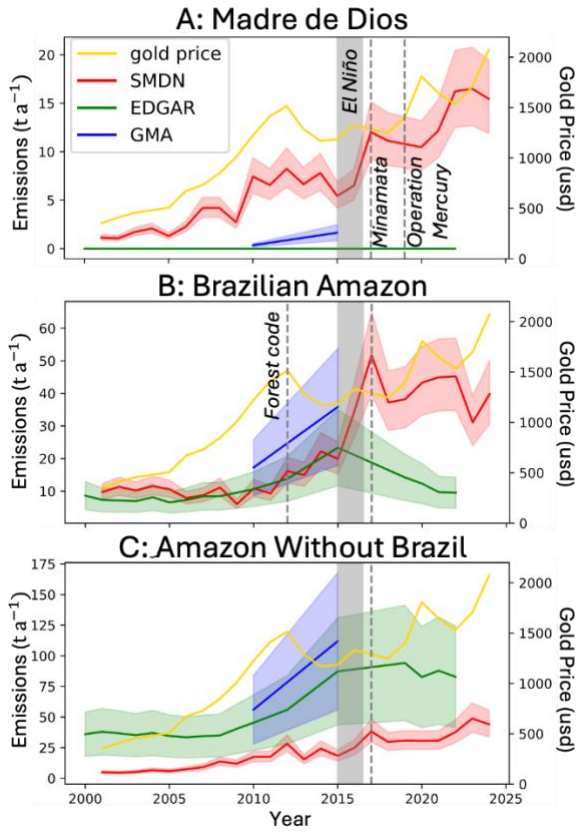

Figure 2-2. Mercury emissions estimates at different spatial scales. *Panels A, B, and C estimate mining emissions by year for Madre de Dios, the Brazilian Amazon, and the non-Brazilian Amazon, respectively, for SMDN, EDGAR, and GMA. We include 95%-CIs for SMDN and reported uncertainties of 50% for GMA estimates. EDGAR does not report gold-mining emission uncertainties, but we include a 50% uncertainty in this plot (matching GMA's uncertainties) to clarify that numbers are not precisely known. Gold price,[50] adjusted for inflation to 2010 US dollars, is also included in each panel. Dashed lines represent national (Brazil's Forest Code and Peru's Operation Mercury) or international (Minamata Convention) policy changes and the gray box represents the 2015-2016 El Niño years.*

2.3.3. Spatial and Temporal Trends in Emissions

SMDN emission time series illuminate the drivers of mercury emissions and downwind mercury concentrations, building on past studies on mining trends.[51,52] Increases in gold price have been previously documented as a driver of informal gold mining.[51,53] Acting as a safe-haven investment during times of economic and geopolitical instability,[54] the price of gold rose during the 2008 recession,[55] the 2018 US-China trade war,[56] and the outbreak of the wars in Ukraine[57] and Gaza.[58] Between 2005 and 2012, when gold prices increased threefold, SMDN's modeled mercury emissions increased 9-fold in Madre de Dios (Figure **2-2**a) and 5-fold in the entire non-Brazilian Amazon (Figure **2-2**c). During this same period, SMDN predicts that the Brazilian Amazon experienced a modest 1.6-fold increase, potentially limited by tighter forest regulation under the 2004 Action Plan for the Prevention and Control of Deforestation in the Legal Amazon[59] (Figure **2-2**b).

While gold price is a key driver of mercury emissions, the temporal trends produced by SMDN also reveal the impact of local and global regulations, as well as climate stress,

which occur as distinct events in time. The first event captured in the dataset was the 2012 Forest Code in Brazil, which pardoned past illegal deforestation, removed restoration requirements, shrunk reserve areas, and signaled a shift towards forest policy favoring agrobusiness.[60,61] After this deregulatory law, SMDN estimates that Brazilian mining emissions increased by 3-fold over the following five years while gold prices decreased and mercury emissions in the rest of the Amazon remained stagnant. Figure **2-3**a shows that this 3-fold increase in the Brazilian Amazon coincided with the migration of mining into conservation concessions and Indigenous lands[62] that previously were minimally impacted. This growth of emissions in response to deregulation indicates that the previous regulatory efforts (i.e., the 2004 Action Plan) were successful in stemming the expansion of mining activity.

The next notable event was the 2015-2016 El Niño, which brought drought to the Amazon. Modeled emissions rapidly increased during this two-year period while gold prices only minimally increased. The growth in emissions over this period exceeded that expected from gold price alone. Prior work has documented that this drought threatened Amazon livelihoods and food security,[63] and studies from other parts of the world have documented transitions into informal gold mining following climate-related livelihood disruption.[64] The increase in mining and associated mercury emissions documented here most likely resulted from this same pattern, with people turning to mining when the drought threatened their livelihoods. Climate projections indicate an increasing frequency of severe drought in the Amazon due to climate change.[65] If gold price remains high, increasingly frequent climate-fueled disasters may precipitate more regular and rapid transitions towards informal mining.

The next major event visible in SMDN's trends is the Minamata Convention, which was an international effort to reduce global mercury emissions that entered force in 2017. Signatory countries ratified laws aimed at restricting mercury import and use, with specific targets around informal gold mining. Between 2017 and 2018, SMDN estimates an initial 26% decline in gold mining emissions across the Amazon; however, over the subsequent six years emissions remained relatively stable, with 2024 and 2018 Amazon-wide estimates differing by less than 1% (Figure **2-2**b and Figure **2-2**c). Increased regulatory efforts following the Minamata Convention may have modestly reduced emissions, partially counteracting the spike associated with the preceding 2015-2016 El Niño drought. Alternatively, a relatively stable gold price between 2012 and 2019 confounds analysis of Minamata's true impact, and a recent rise in emissions in Madre de Dios could reflect the increase in gold prices between 2019 and 2024. Regardless, the post-Minamata mining landscape illustrates, at best, a plateau rather than a substantial decline in mercury emissions; the success of regulation and enforcement appears hindered by strong gold prices, which keep informal gold mining more economically attractive than other industries in mining regions.[66]

The final event considered is the 2019-2020 Operation Mercury, where over 1,000 police and soldiers[67] were deployed in Madre de Dios, Peru, to remove illegal mining operations in southern La Pampa bordering the Tambopata Reserve. Figure **2-3**b shows the effort redistributed where mining occurred but only resulted in a small and temporary net reduction in mining emissions (Figure **2-2**a), which is consistent with previous research into this event that tracked mining pond expansion.[52]

Gold price appears to be a primary driver of emissions, incentivizing mining activity. Livelihood disruptions like droughts can accelerate the transition to this informal industry as other livelihoods become less secure. Regulation has helped check the growth of mining, but it has not notably reduced existing mining activity, especially if miners can move from targeted zones into other areas. Complementary interventions including bottom-up formalization of the informal mining industry,[68] the promotion of mercury-free mining technology,[69] and interventions targeting reductions in global gold consumption[70] may be necessary to substantively reduce mercury emissions from informal gold mining.

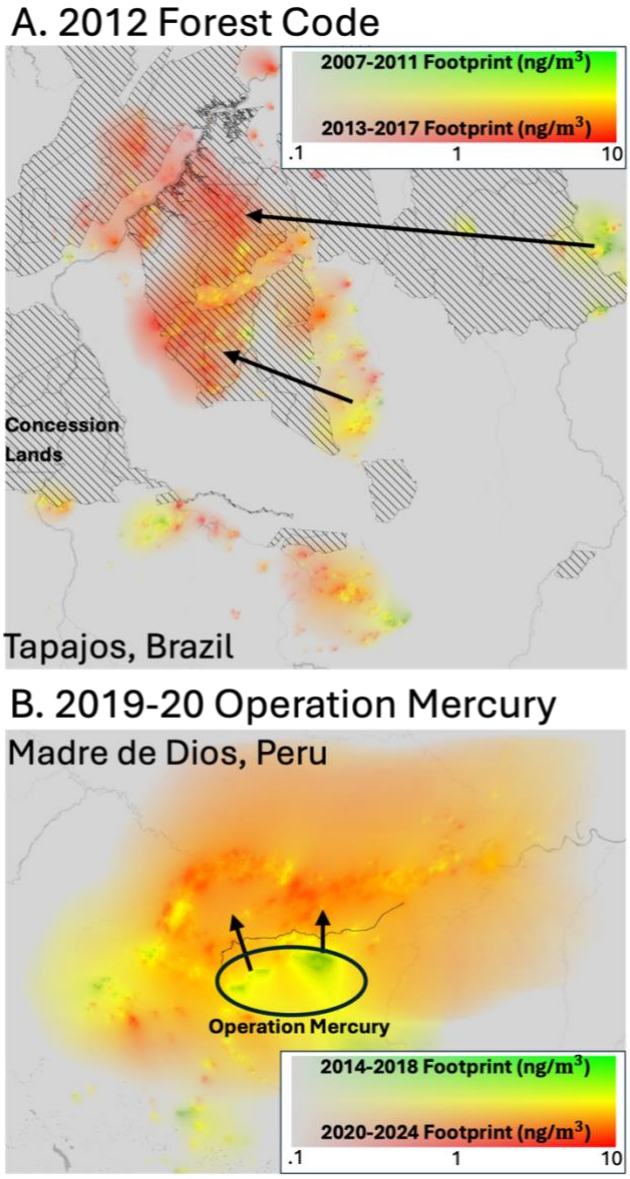

Figure 2-3. Modeled mercury concentration footprints before and after regulation events. *Modeled concentration footprints in Brazil's Tapajós basin (panel A) and Madre de Dios, Peru (panel B) during the five years before and after Brazil's 2012 Forest Code deregulating deforestation (panel A) and Peru's 2019-2020 Operation Mercury, an enforcement operation targeting illegal mining camps (panel B). Green shows the average concentration footprint in the five years preceding each event and red shows average concentration footprint during the five subsequent years. Red and green mix to form gradients of orange as an RG composite (mixing creates yellows). Panel A includes hatched shaded regions that show conservation and Indigenous land concessions. Panel B includes the Interoceanic highway and circles Operation Mercury's region of enforcement south of the highway bordering the Tambopata Reserve.*

2.3.4. Using Concentration Footprints to Understand Ecosystem and Human Exposure

SMDN's 1-kilometer resolution concentration maps allow us to identify potential impacts on ecosystems and people living near emission sites. In Figure **2-4**a we show percentiles of mercury exposure across the entire Amazon, conservation concessions, Indigenous land concessions,[62] croplands,[71] and urban areas (VIIRS > 0.6 $\mathrm{nW\ sr^{-1}cm^{-2}}$ after 2013[36] and CCNL > 3 DN before 2012[37]).

In 2024, 1.5% (100,000 km^2) of Amazon land area was exposed to double background mercury (> 1.36 ng m^{-3}) due to mining. Each assessed land type, other than urban areas, experienced similar relative exposures to mercury from mining in this year, including 1% (24,000 km^2) of Indigenous lands, 1.2% (27,000 km^2) of conservation concessions, and 1.7% (3,400 km^2) of croplands. Notably, the existence of above-background levels of mercury on Indigenous lands is consistent with prior research documenting mining encroachment into these protected areas.[72] Urban centers were disproportionately affected, with 17% of urban area (9,400 km^2) exceeding double background concentrations in 2024. These results suggest there are meaningful mercury increases across tens of thousands of square kilometers of the Amazon, with disproportionate impacts in urban areas.

This disproportionate impact on urban landscapes is of particular concern for the Amazon's 20.9 million urban residents.[40] We proxied Amazon urban resident density with nighttime light and estimated that approximately 7,800 people were exposed to an average of 1,400 ng m^{-3} in 2024, which is the concentration at which neurological effects have been observed in dental workers[73] (see Figure **2-4**b). For chronic exposure in the general population, the 24-hour average exposure limits[74,75] range from 30 ng m^{-3} to 300 ng m^{-3}. The general population includes children and pregnant people, who may experience toxic effects at lower concentrations, and the wide range reflects the challenges of extrapolating occupational-hazard research to understudied vulnerable populations. At these two thresholds (30 and 300 ng m-3), an estimated 220,000 and 30,000 Amazon urban residents, respectively, were at risk of mercury toxicity in 2024.

This analysis also allows us to track mercury exposure changes over time. Between 2001 and 2024, there was a 5-fold increase in total mercury emissions across the Amazon, which corresponded to a 4-fold increase in residents exposed to double background levels of mercury, a 7-fold increase in residents exposed to 30 ng m^{-3}, a 9-fold increase in residents exposed to 300 ng m^{-3}, and an 8-fold increase in residents exposed to 1400 ng m^{-3}. These results reveal a greater-than-proportional relationship in the fraction of people exposed to toxic levels of mercury as emissions increased.

To illustrate how future changes in mining activity and mitigation could affect exposure, we evaluated two simplified bounding scenarios for 2026 mercury emissions. Both scenarios estimate 2026 emissions from 2024 data. For the upper bound emissions estimate, we noted that gold prices doubled between 2024 and 2026[50] and assumed that the historical elasticity of modeled emissions to gold price holds (i.e., $\epsilon = \log_3(5) = 1.46$, based on the 3-fold increase in gold price that corresponded with the 5-fold increase in modeled emissions observed in section 2.3.3). Extrapolating the historic elasticity to a doubling of gold price implies a 2.8-fold increase in emissions. To model the resulting mercury concentration footprint in this scenario, we held the 2024 spatial distribution of emissions constant because post-2024 mining data are not yet

reliably available. Under these assumptions, the number of urban residents exposed to 30, 300, and 1,400 ng m^{-3} increased to 590,000, 71,000, and 18,000, respectively (see Figure **2-4**c), corresponding to 2.7-fold, 2.4-fold, and 2.3-fold increases relative to 2024.

In a contrasting lower-bound mitigation scenario, we assumed that mining remained at 2024 levels (i.e., net neutral growth in mining), mercury-capture technologies such as fume hoods and retorts were adopted universally, and these technologies had an 80% capture efficiency.[45] Under this scenario, the number of urban residents exposed to 30, 300, and 1,400 ng m^{-3} decreased to 55,000, 7,500, and 1,700, respectively, representing 4.0-fold, 4.0-fold, and 4.6-fold reductions relative to 2024 (see Figure **2-4**c).

Across all concentration thresholds, the estimated population exposed to dangerous mercury thresholds ranged by a factor of 9 to 11 between these two bounding scenarios. This result suggests that regulatory efforts aimed at limiting mining's expansion alongside bottom-up interventions promoting safer mercury practices could substantially reduce mercury toxicity experienced by future Amazon urban residents relative to taking no action.

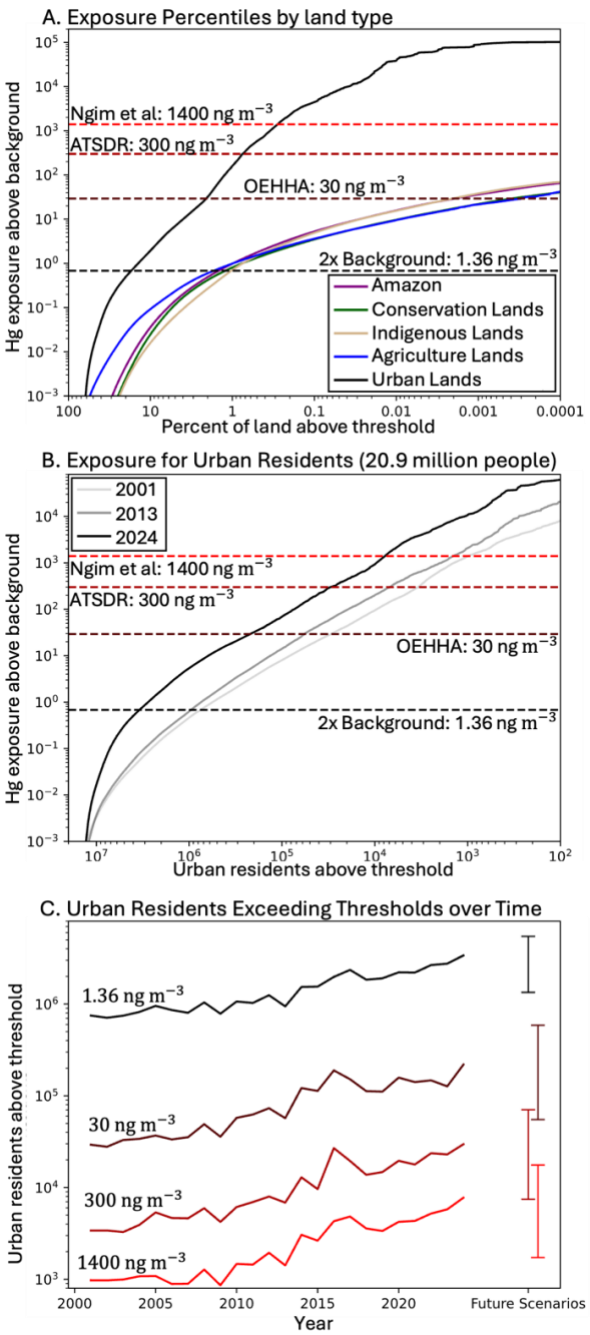

Figure 2-4. Exposure of land and people to mercury. *Panel A shows percentiles of modeled mercury exposure in 2024 due to mining across the entire Amazon, in conservation concessions, in Indigenous concessions, in croplands, and in urban areas for the SMDN model. Thresholds are marked matching where modeled concentrations are double background atmospheric Hg levels (2x 0.68 $ng\ m^{-3}$), the state of California Office of Environmental Health Hazard Assessment (OEHHA)'s chronic exposure threshold[74] (30 $ng\ m^{-3}$), U.S. Department of Health and Human Services Agency for Toxic Substances and Disease Registry (ATSDR)'s chronic exposure threshold[75] (300 $ng\ m^{-3}$), and a threshold at which neurological effects have been observed from chronic exposure[73] (1400 $ng\ m^{-3}$). Panel B shows percentiles of modeled Amazon urban resident exposure in 2001, 2013, and 2024 due to mining under the SMDN model, with the same toxicity thresholds included. Panel C shows the number of Amazon urban residents exposed to each exposure threshold in each year between 2001 and 2024. Future scenarios are bounded by a gold-price-elasticity scenario where production tracks the doubling in gold prices from 2024-2026 and a mercury-capture scenario where mining remains at 2024 levels, but all miners adopt mercury-capture technology with 80% efficiency.*

2.3.5. Synthesis and Outlook

SMDN represents the first high-resolution mercury emissions inventory for informal gold mining, derived from satellite mining identification and on-the-ground air-mercury measurements. By linking emissions to downwind concentration, SMDN offers a novel approach that jointly estimates both atmospheric mercury sources and their spatial concentration footprints using Lagrangian transport. Unlike existing inventories, SMDN generates temporally consistent emissions estimates that support trend analysis across time and space, while offering empirically calculated uncertainties. The mercury concentration footprints produced by SMDN provide concentration information where on-the-ground measurement is costly or infeasible. These concentration footprints can be used to assess exposure risk in urban and remote populations in gold-mining regions.

In a globalized world, distant human and natural systems are coupled.[76] Trends observed by SMDN indicate that global geopolitical drivers are linked with mercury emissions, downwind concentration footprints, and human exposure. Emission inventory analysis corroborates past findings[52,68] that top-down formalization and enforcement approaches constrain mining in the short term yet fall short of delivering long-term reductions. Complementary bottom-up approaches that promote mercury-free mining and secure alternative livelihoods may therefore be critical for long-term mitigation. Conversely, consumer-based interventions[70] can target gold demand, limiting the industry's long-term growth.

Concentration footprint analysis highlights the scale of mercury impacts felt by urban residents. Ultimately, reducing the use of mercury and expanding the use of mercury-capture technologies offer the most direct path to reduced human-health impacts, but other interventions can also help mitigate mercury's harmful effects. Inadequate ventilation in mining shops has been linked to elevated levels within these shops and surrounding streets,[13] and the use of chimneys could address these issues by diluting the most acute nearby exposure.[11] In addition, replacing any nighttime burning with daytime burning would utilize the greater dispersion resulting from daytime convective mixing and reduce concentrations, which would help in all areas but could be particularly impactful in urban locations.

Despite years of international attention, mercury emissions from informal gold mining remain a persistent and growing problem in mining regions concentrated in the tropics and Global South. Our analysis suggests that limiting the harmful effects of mercury from gold mining will require an integrated approach targeting each potential intervention point including reducing global gold demand, supporting alternative livelihood security, promoting mercury-free mining, improving the accessibility of mercury-capture technology, and taking steps to mitigate exposure where mercury is emitted. Further cross-regional research that connects mining's mercury

concentration footprints with the global geopolitical, economic, and environmental drivers of mining and downwind exposure can help link the human, regional, and global scales and target interventions at each level.

Chapter 3. Mercury Emissions from Amazon Gold Mining Reduce Forest Productivity and Carbon Stocks

3.1. Introduction

The Amazon is a key, yet shrinking, terrestrial carbon sink,[8] but deforestation and drought have pushed parts of the Amazon into becoming a net carbon source.[77] This transition is considered a critical climate tipping point, fueling positive forest die-off feedback loops.[78] Informal gold mining is a key driver of Amazon deforestation,[25] accelerating this transition. However, we hypothesized that mercury emissions from informal gold mining further reduce the carbon-uptake capacity of Amazon forests beyond the immediately visible mining scars.

Modeling has shown that this released gaseous elemental mercury travels dozens of kilometers, contaminating nearby forests (see Chapter 2). In forests downwind from mining, this gaseous mercury can absorb through plant stomata and elevate canopy leaf concentrations.[19]

Mercury is known to limit an aquatic species' photosystem performance at a 0.2 μM water concentration,[79] impact Amazon agricultural plant traits at a 2 μM soil concentration,[80] and reduce net photosynthesis in *maize* leaves at a 50 $\mathrm{ng\ m^{-3}}$ air concentration.[81] These previous findings indicate mercury from mining could pose a threat at high concentrations, but it remains unknown whether long-term low-dose mercury exposure from mining non-negligibly affects contaminated downwind forests.

Using a combination of satellite remote sensing and on-the-ground sampling, we show that mercury from millions of hectares of Amazon gold mining induces photosystem toxicity and broader physiological changes at chronic low doses. This degradation reduces overall forest productivity downwind of mining regions, exceeding the productivity declines from actual mining deforestation. Combined with mining deforestation, mercury degradation from gold mining introduces a host of potential impacts to regional hydrology, food security, and livelihoods, and the associated substantial carbon stock declines that have a social valuation approaching the market value of the gold produced.

3.2. Methods

3.2.1. Leaf Sampling

Field samples were collected at 6 sites along a mining contamination gradient in Madre de Dios, Peru during September of 2025, the end of the dry season (see Figure 3-1 for sampling sites). Pioneer species *Cecropia peltata* and *Gynerium sagittatum* were sampled due to their importance in ecosystem succession, their straightforward species identification, and abundance across the Madre de Dios region.[82] Leaves were collected near the edge of rivers at 5 sites and the edge of a mining camp at the La Pampa site. The third newest leaf on the branch (from the tip where new leaves grow) was selected for *Cecropia* and the tenth newest leaf for *Gynerium;* these selections were approximately half the average total number of leaves per branch meaning that samples captured the middle of leaves' lifecycles. Ten leaves of each species were collected from individual plants at each site, stored on ice, and then freeze dried.

The diameter at breast height of each sample plant was measured. Photographs were taken of leaves on a fixed area reference tarp to isolate leaf area, to estimate leaf size. Chlorophyll content was measured using a SPAD meter averaged over four segments of each leaf.

We measured OJIP Chlorophyll fluorescence Kinetics using an Opti-Science OS30P+ fluorometer. To maintain leaf freshness during chlorophyll analysis, whole branches were cut and placed immediately in water for a 20–30-minute dark adaptation process. After dark adaptation, three segments of each leaf were saturated with light and analyzed for their fluorescence response curve. We recorded the fluorescence response at the following time lags after light saturation: O=0 ms, K=0.3 ms, J=2 ms, I=30 ms, and P referring to the peak observed fluorescence (it is not a priori known when this peak will occur). Following prior studies,[83,84] we proxied for general photosystem II (PSII) disruption with reductions in maximum quantum efficiency: (P-O)/P (no impact was observed by this measurement); we proxied oxygen evolving complex (electron source for PSII) limitations with increases to K-step: (K-O)/(J-O); and we proxied disruptions to photosystem I (PSI) performance with decreases to IP-rise: (P-I)/(P-O).

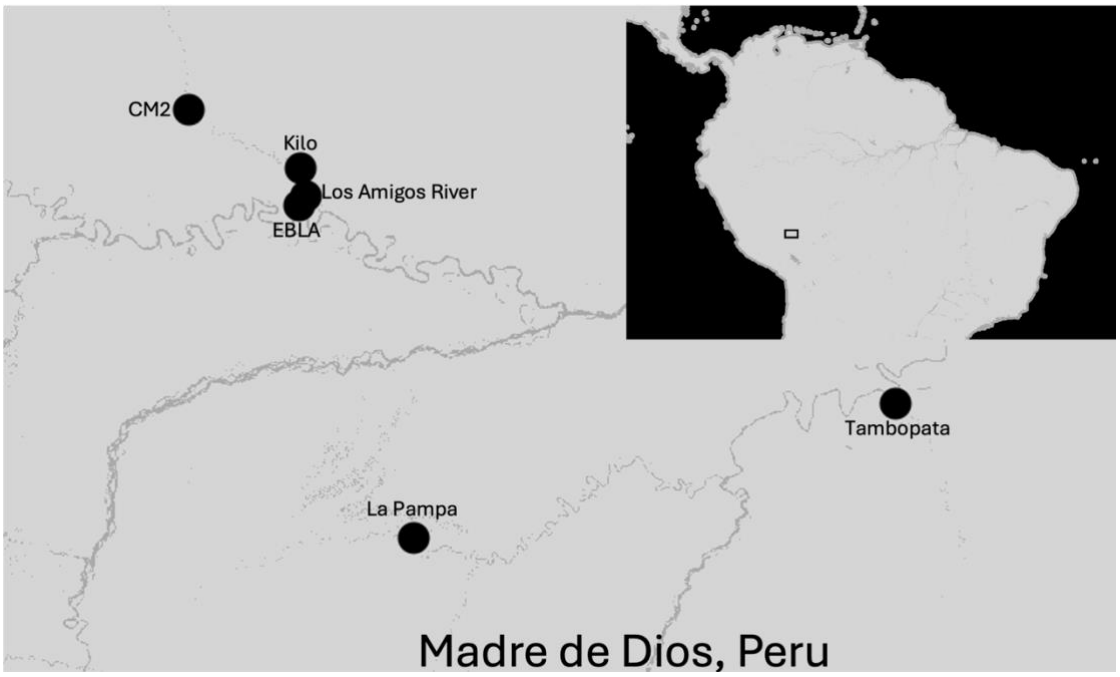

Figure 3-1 shows the leaf sampling sites used in this study.

3.2.2. Total Mercury Analysis

Freeze dried leaves were homogenized and analyzed with a direct combustion mercury analyzer (Nippon MA-3000).[85] Three blanks and three National Institute of Standards and Technology (NIST) 1575A (pine needles) were run during daily instrument startup, and an additional three blanks, 1 triplicate, and 1 NIST 1575A standard was run for every 10 samples analyzed. Triplicates were accepted if they had less than 15% standard deviation, standards if they were within 20% of their known concentration, and blanks if they showed concentration less than 10% of the minimum mercury mass in the surrounding sets of 10 samples. Upon any failures to meet these criteria, the surrounding sample batches were rerun.

3.2.3. Building MODIS Annual De-Seasonalized NIRv Greenness Composites

This section describes the development of a 1-kilometer resolution satellite greenness dataset for forested pixels across the Amazon, which will be compared to modeled mining-concentration footprints from Chapter 2. To estimate greenness, we use $NIRv = NIR \times (\frac{NIR-RED}{NIR+RED} - .08)$ defined from satellite red and near-infrared bands.[86] NIRv has been found to outperform other greenness measures including NDVI and EVI and is on par with the less readily available SIF in estimating plant productivity.[87] Due to the frequent cloud cover in the Amazon and our need for precise estimates to deduce a relatively small mercury effect on plant health, we sacrificed the high spatial resolution of Landsat and Sentinel satellites for the daily temporal resolution of MODIS Terra Daily Surface Reflectance 250m (MOD09GQ.061).[88]

Before calculating annual averages, we removed pixels from images where the quality assurance bands indicated low reliability in either the RED or NIR band (including due to cloud effects). We further eliminated pixels outside of typical ranges we observed in forested Amazon ecosystems: RED $\in [.012, .04]$ and NIR $\in [.2, .4]$, which functioned to delete false-positive cloud-free pixels, and some false-negative deforested pixels.

A direct average of pixel values from cloudless days for each pixel throughout the year may introduce additional noise or bias. Despite MODIS providing daily images for every pixel, frequent clouds mean that pixels have relatively few available days where high-quality reflectance can be retrieved. Given that pixel greenness tends to be higher in the wet season than the dry season, a direct average introduces additional noise driven by the seasonal availability of each pixel. Furthermore, if microclimates affect seasonal availability per pixel, this would differentially bias pixel averages.

To address this potential bias, we first de-seasonalize greenness before taking annual averages. To de-seasonalize pixels, we assigned each pixel a fixed effect for each month and for each year in the sample period (with one year removed to prevent the regression from being underdetermined). We then define annual averages by adding the average fixed effect across months to the fixed effect for the given year.

We excluded likely deforested sites by removing all 250-meter MODIS pixels containing any 30-meter pixel where the Global Forest Change dataset[30] identified any forest loss between 2001 and 2025 or an initial forest cover below 95%. We further excluded 250-m MODIS pixels neighboring an identified deforested pixel, where prior validation[30] has found that Global Forest Change is most likely to mistakenly identify deforested pixels as forested. We also removed all pixels with NIRv more than 0.04 (unitless reflectance) below any neighbor within 500 meters; these pixels show greenness substantially below neighbors, which could indicate deforestation.

After deleting potentially deforested pixels, we aggregated the dataset to a 1000m resolution. This was necessary for computational feasibility given the millions of square kilometers in the Amazon rainforest. Averaging out fine-resolution signal in the dependent variable of this regression analysis may reduce the signal-to-noise ratio, but it will not introduce bias.

To improve the signal-to-noise ratio in this analysis, we control for inter-annual variability in greenness (e.g. from El Niño-Southern Oscillation) by dividing greenness values by the median of all forested pixels within a 300-kilometer-radius bounding box in the given year. This offers the added benefit of translating surface reflectance to more physically meaningful units: a pixel's fractional greenness relative to an "average" forested pixel in surrounding Amazon forests.

3.2.4. Mercury Concentration Footprint Selection

This chapter utilizes the mining concentration footprints from Chapter 2. Mining sites differ year to year, allowing us to compare pixels before and after nearby mining begins; on the other hand, gold shops in mining towns remain stationary over time, with modeled emissions only changing based on variability of total mining aggregated over nearby regions. We focused our analysis on only the mining site component of the downwind concentration footprints, allowing us to investigate year-to-year changes within the same pixels as mining sites form and are abandoned upwind.

3.2.5. Regression Methodology

To understand the impacts of downwind mining concentration footprints, *F(X, t),* on forest greenness, *G(X, t)*—where X is a pixel's location and t is a year—consider the simplified model:

$$\boldsymbol{G}(X,t) = \gamma + \alpha \times \boldsymbol{F}(X,t)$$

Note that $G(X,t)$ is unitless reflectance (normalized so that 0 represents no reflectance and 1 represents a typical forested pixel), γ is similarly unitless, $F(X,t)$ is a concentration ($\mathrm{ng\ m^{-3}}$), and α is an inverse concentration ($\mathrm{ng^{-1}\ m^{3}}$).

We further reduce noise from pixel fixed effects by comparing the year-to-year temporal gradient year-to-year of greenness and footprints rather than their total values. To control for region-level biases, we compare the spatial gradient of both sides of the regression:

$$\frac{d\boldsymbol{G}(X,t)}{dx\ dt} = \alpha \frac{d\boldsymbol{F}(X,t)}{dx\ dt}$$

This equation compares how greenness changes along the mining concentration footprint gradient (but remove any region-to-region comparison). Note that the γ constant disappears when taking the derivatives of both sides.

To understand the shape of the 1-year footprint impact on greenness (in Figure SI 6-8), we discretize F into categorical bin variables with $F_{(C,C+\delta)}(X,t)$ marked as 1 for a pixel-year combination if the footprint in that pixel year lies within that interval concentration interval $(C, C+\delta)$ and 0 otherwise. We then consider the regression:

$$\frac{d(\boldsymbol{G}(X,t))}{dxdt} = \sum_{-5}^{24} \alpha_i \frac{d(\boldsymbol{F}_{(2^{0.2*i}, 2^{0.2*(i+1)})}(X,t))}{dxdt}$$

In this model, regression coefficients α_i ($\mathrm{ng^{-1}\ m^{3}}$) correspond to the average greenness impact from a concentration footprint ($\mathrm{ng\ m^{-3}}$) in the range $\left(2^{0.2*i}, 2^{0.2*(i+1)}\right)$. By excluding all pixels below $0.5\ \mathrm{ng\ m^{-3}}$ (corresponding to $i < -5$), we normalized greenness impacts to the uncontaminated pixels. Pixels above $32\ \mathrm{ng\ m^{-3}}$

(corresponding to $i \geq 25$) were also excluded since the sparsity of concentration footprints led to high uncertainties.

For lagged impact and recovery analysis (see Figure 3-3b), we include regressors for concentration footprints in each of the 15 years leading up to the year in which greenness is measured.

$$\frac{d(\boldsymbol{G}(Year, X))}{dxdt} = \sum_{i=0}^{14} \alpha_i \frac{d(\boldsymbol{F}(Year - i, X))}{dxdt}$$

In this analysis α_i ($\mathrm{ng}^{-1}\ \mathrm{m}^3$) represents the impact of concentration footprints ($\mathrm{ng\ m}^{-3}$) on greenness (unitless) looking i years into the future.

Note that both greenness and concentration footprints were available between 2001 and 2025. We only included greenness years between 2005 and 2025 in the regression to ensure there were at least 5 prior years of concentration footprints that could inform the observed greenness change. For greenness years between 2005 and 2015, the full 15 years of past footprint data were unavailable, in which case we set the missing prior years' footprint change to 0. By setting the unknown footprint change in prior years to zero, earlier years do not impact the regression's calculation of the corresponding α_i (and will not impact other α_j as long as there is negligible temporal autocorrelation in the growth rate of concentration footprints).

3.2.6. Regression Uncertainty

Naïve uncertainty estimation for these regression coefficients is negligible due to millions of pixel years used to calibrate a small number of variables, even after applying standard spatial auto-correlation adjustment techniques. The regression model's spatial gradient approach allows us to produce more conservative uncertainty estimates. We compared regression coefficients produced along the longitudinal spatial gradient against the values produced along the latitudinal axis. We assume that large-scale regional spatial correlates of both (modeled) mercury concentration footprints and greenness occur relatively independently along the two spatial axes; we also assume that such hypothetical correlations with hidden spatial features occur independently across different lag years after mining began upwind.

Given these two assumptions, the difference between the longitudinal and latitudinal gradient's regressions offer us 15 differences of pairs of random samples (one per year of 0 to 14 years of lag) for potential spatial autocorrelation and other hidden variables that are directional in nature. These 15 differences appear to be homoscedastic with the lag year corresponding to each regression coefficient and were therefore treated as sample-pairs drawn from the same variance and an unknown (variable) mean. The maximum likelihood estimator of this shared variance offers a conservative statistical error in regression coefficients. This produced wider confidence intervals than direct

regression statistical error even accounting for spatial auto-correlation adjustment statistical error calculation.[89] Furthermore, these conservative errors appear to be robust, as they are sufficient to smooth jagged point estimates for the lagged effect across years after mining (see Figure 3-3), which is consistent with an underlying smooth curve for forest's recovery over time.

3.2.7. Isolating Downwind Mercury Impacts from Confounding Variables

To justify that observed greenness impacts were due to mercury toxicity, we needed to carefully account for potential confounding variables. A failure to exclude deforested pixels that could spatially correlate with mining represents one potential confounder (see section 3.2.3 on the exclusion process for deforested pixels), but microclimatic effects and satellite image smearing are also worth consideration. The following empirical tests were also run to isolate mercury effects from other confounding variables.

We considered the greenness impacts observed downwind of non-mining deforestation in the Amazon to justify that the observed impacts are specific to mining regions. Specifically, we assigned a pseudo-mercury emission to non-mining deforested pixels (where we do not expect substantial true emissions) at the same per-area emission rate as identified from mining deforestation pixels (see Chapter 2). These pseudo-emissions were then distributed with Lagrangian transport modeling (see Chapter 2) across the landscape, producing non-mining pseudo-concentration footprints. We then followed the same 15-year lag regression framework for these non-mining pseudo-concentration footprints as for mining concentration footprints (see section 3.2.5). If confounders like satellite smearing, a failure to exclude deforestation, and microclimatic effects were to explain the observed greenness impacts downwind of mining, they would also be expected to show up downwind of non-mining deforestation in this pseudo-footprint analysis. However, since these non-mining areas do not have substantial mercury emissions, true mercury impacts would not be observed. Therefore, this pseudo-concentration footprint analysis downwind of non-mining deforestation acts as an effective negative control[90] for these likely confounders.

To isolate the specific wind-directional component of mining impacts on greenness, we subtracted a proximity-based mining concentration footprint from Chapter 2's modeled footprint and regressed greenness against the resulting difference. Specifically, we applied an angular averaging function, A, to Lagrangian plume sensitivities, Plume, to make them isotropic. The resulting isotropic plume sensitivities were then convolved against mining-site emissions as in Chapter 2 to produce proximity-based mining concentration footprints, P:

$$P(\mathrm{X},\mathrm{t}) = \left(E_{\mathrm{site}} \times \delta_{\mathrm{site}}(\mathrm{X},\mathrm{t})\right) \otimes A(\mathrm{Plume}(\mathrm{X},\mathrm{t}))$$

Subtracting these proximity-based mining concentration footprints from Chapter 2's footprints, we are left with the wind-directional component of these footprints. Subtracting isotropic plumes from the original plumes results in directional plumes with, on average, 0 sensitivity at all distances from an emission, meaning that all proximity-based impacts on greenness are excluded from this analysis; however, any wind-directional impacts are preserved. By regressing greenness change against this directional footprint, we confirmed that there is an effect from mining on downwind greenness that cannot be explained by proximity alone.

3.2.8. Gross Primary Productivity and NPP impacts

To calculate a modeled gross primary productivity (GPP) impact on a pixel X in a given year, we multiplied a pixel-year's predicted fractional greenness loss by an estimated baseline forested productivity. Specifically, a pixel's baseline NIRv (for a given year) was estimated as the median NIRv value in forested pixels within 200 km of that pixel with a modeled concentration footprint less than $0.1\ \mathrm{ng\ m^{-3}}$ (i.e., uncontaminated nearby pixels). The fractional greenness change was calculated by multiplying the prior 15 years of modeled concentration footprints (see Chapter 2) by the respective lagged regression coefficients (see section 3.2.5) and summing the results. To estimate the corresponding change in GPP, this fractional greenness change was multiplied by a 44.5 $\mathrm{tC\ km^{-2}\ day^{-1}}$ NIRv-to-GPP slope for evergreen broadleaf forests estimated by past research.[91]

3.3. Results and Discussion

3.3.1. Amazon Plant Toxicity during Moderate Air-Mercury Exposure

Across a mercury contamination gradient in Madre de Dios, Peru, chlorophyll fluorescence kinetics measurements indicated decreasing photosystem performance with increasing mercury exposure for two different species, a C3 grass (*Gynerium sagittatum*) and a pioneer tree (*Cecropia peltata*).

When dark adapted and subsequently exposed to light, contaminated leaves exhibited a greater increase in fluorescence in the first 0.3 ms (see Figure 3-2a) indicating an initial photosystem II (PSII) limitation, which has been previously associated[83] with reduced oxygen-evolving complex performance. In *Gynerium* (but not *Cecropia*), contaminated sites exhibited a smaller fraction of fluorescence rise occurring after 30 ms (see Figure 3-2b), indicating a downstream redox limitation that past research[84] has found to occur under photosystem I limitation. Both species experienced an initial oxygen evolving complex limitation (which supplies electrons to photosystem II), as this early photosystem stage is more immediately exposed to any mercury absorbed through stomata. However, we observed differential downstream photosystem impacts, suggesting that *Cecropia* may be more able than *Gynerium* to protect

photosystem I (PSI); furthermore, prior research[92] has noted an absence of PSI repair mechanisms that mean mercury toxicity is permanent during a leaf's lifecycle.

These limitations in a leaf's maximum photosystem activity may explain the following observed physiological changes. For both *Cecropia* and *Gynerium*, we observed reductions in diameter at breast height (Figure 3-2c) and leaf size (Figure 3-2d) as leaf mercury levels increased, indicating that carbon expenditure reduces with mercury exposure. Reductions in chlorophyll content were observed for *Gynerium* but not *Cecropia* (Figure 3-2e). In aggregate, the results indicate cross-species mercury toxicity in Amazon plants, but *Gynerium* experienced a larger effect size and had more traits affected than *Cecropia*.

These results extend established literature documenting photosystem toxicity from aquatic[79] to terrestrial plants. These findings build on prior soil-spike experiments documenting physiological changes,[80] and offer the first Amazon-field study documenting plant mercury toxicity along an air-contamination field-gradient. We identified toxic effects at an order of magnitude lower concentration than prior controlled-field study results[81] where physiological impacts occurred at 20-50 $\mathrm{ng\ m^{-3}}$ air concentrations. If substantially lower contamination levels measurably affect plant growth, then photo-toxicity can be expected to extend across a much wider land area downwind of mining than was previously known.

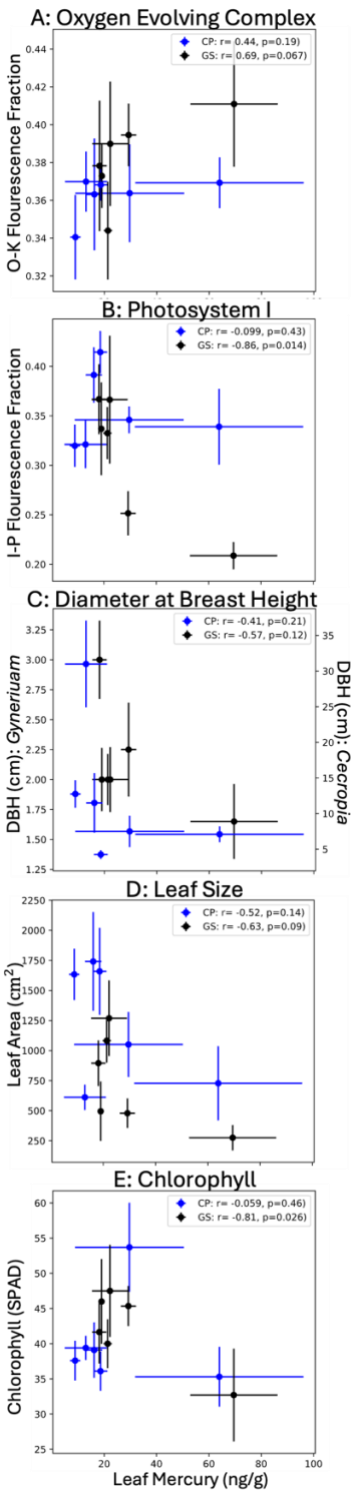

Figure 3-2 shows plant physiological changes for Gynerium sagittatum (GS) plotted in black and Cecropia peltata (CP) plotted in blue versus leaf mercury concentrations along an air-contamination gradient that includes LP (4.62 $ng\ m^{-3}$), MDD (2.23 $ng\ m^{-3}$), LAR (1.45 $ng\ m^{-3}$), TAM (1.74 $ng\ m^{-3}$), KILO (1.68 $ng\ m^{-3}$), and CM2 (near background). Panels a-e show in order: oxygen evolving complex efficiency (proxied by the fraction of initial 2 ms fluorescence rise occurring during the first 0.3 ms), photosystem I efficiency (proxied by the fraction of fluorescence variable fluorescence occurring after 30 ms), diameter at breast height, leaf size, and chlorophyll content (proxied by SPAD measurements which combines infrared and red reflectance bands). Site level correlations (r) and Pearson one-tailed p-values of those correlations are included in each panel. The main text notes likely mercury stress for measured physiological parameters if p<0.05 for the leaf level mercury comparison (n=60 leaves) and (due to the underpowered nature of a 6-site mercury-gradient study) p<0.1 for site level average comparison; for reporting cross-species significance, the Stouffer combined p-value was required to meet those criteria.

3.3.2. Using Satellite Greenness to Estimate Amazon GPP Declines

Chapter 2 identified tens of thousands of square kilometers experiencing more than double background mercury levels due to mining, primarily in Madre de Dios, Peru; Tapajos, Brazil; and the Guiana Shield. To understand the forest productivity impact of this widespread low-dose exposure, we compared changes (over time and space) in satellite-measured greenness against modeled atmospheric footprints from mining sites. We observe declining Near Infrared Reflectance of Vegetation (NIRv) between 2005 and 2024 within the mining footprint hotspots of Madre de Dios, Peru (see Figure 3-3a). Furthermore, NIRv declines appear to increase linearly with mercury exposure (see Figure SI 6-8). Aggregated over 15-years of lagged impact, we estimate a $3.7 \pm 0.09\%$ reduction in NIRv per $\mathrm{ng\ m^{-3}}$ of ground-height air-mercury exposure (assuming long-term exposure at that concentration) and found that forests require 10 to 15 years to recover after mercury exposure (see Figure 3-3b).

We confirmed the impacts are specific to sites downwind of mining and negligibly occur downwind from deforestation in general: $0.4 \pm 0.2\%$ per $\mathrm{ng\ m^{-3}}$ when we applied a pseudo-non-mining site emission rate that matches the per-square-kilometer rate at mining sites. Therefore, the observed impact is specific to pixels downwind of mining deforestation and not deforestation in general.

We also considered the possibility that we failed to fully exclude all deforested pixels downwind of mining. This could occur due to either micro-deforestation not captured by our forest exclusion protocol or potential smearing of nearby deforested pixels (into forested pixels) when MODIS images were collected at a high angle to the ground. In either case, the effect would depend only on proximity and be uncorrelated with a region's predominant wind direction. Removing the isotropic proximity-based component of concentration footprints (see section 3.2.7), we found that greenness still decreases significantly ($p=0.02$) with the remaining directional component of footprints (aggregating regression coefficients over 15 years of modeled lag impact). Therefore, the effect acts according to wind direction and not just proximity, which is consistent with mercury contamination but not with a failed exclusion of deforestation or MODIS image smearing.

Hydro-climatological feedbacks and dust generated from mining present other possible mechanisms that could be consistent with the wind-specific directional influence on greenness, if they were to exhibit larger impacts from mining than other types of deforestation. However, we observed a similar change in land-surface heating downwind of both non-mining and mining deforestation (see Figure SI 6-7), suggesting that hydro-climatology does not substantially differ between sites downwind of mining versus sites downwind of other types of deforestation. Therefore, climatological feedbacks from deforestation are unlikely to explain the uniquely decreasing greenness downwind of mining areas (see section 3.3.4 for potential impacts on precipitation at

greater distances). On the other hand, the observed 10–15-year recovery time after initial mining scars form (see Figure 3-3b) is inconsistent with dust mobilization during the initial land clearing process (dust quickly washes off leaves as throughfall). Together, these controls suggest that a unique aspect of mining areas is degrading downwind forests, and alternate explanations of dust or microclimates appear inconsistent with the observed trends.

This 10–15-year recovery time could indicate that the footprint model incorrectly attributes emissions to the first year when an area is cleared for mining rather than modeling continuous emissions on this multi-year timescale; alternatively, the recovery timeline is consistent with mercury inducing longer-term physiological changes that reduce carbon assimilation beyond when direct mercury exposure ceases. Either way, the regional effects of mining appear to last long beyond when mining scars first appear.

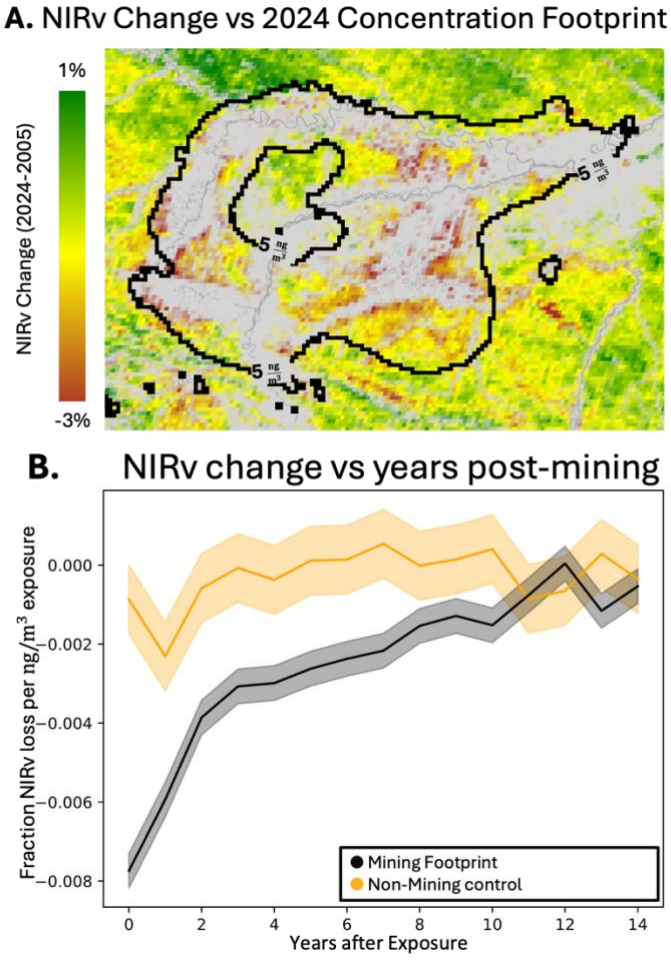

Figure 3-3. Plot A displays normalized NIRv change (normalized by the average NIRv of forested pixels within 300 km) between 2005 and 2024 overlaid with modeled 5 ng m^{-3} mercury exposure contours for 2024 (see Chapter 2). Plot B displays estimated multiple-linear regression coefficients of normalized NIRv versus footprints for 0-15 years after modeled footprints (black) and for the non-mining control pseudo footprints (orange).

3.3.3. Aggregate Amazon Forest Productivity Loss

Combining results from satellite analysis with on-the-ground measurement strengthens causal inference. Field measurements establish a physiological impact and control for confounding variables that satellite data cannot distinguish. On the other hand, satellite data confirms the impacts extend across Amazon mining regions and integrates the canopy species that drive Amazon productivity. Together, these results support the hypothesis that mercury from gold mining drives productivity loss across the Amazon.

To estimate Amazon gross primary productivity declines from mercury degradation, we multiplied each pixel's estimated percent decline by a 2001 GPP[93] estimate and found a 23.2 ± 0.6 MtC a^{-1} reduction in Amazon gross primary productivity in 2024 (see Figure 3-4a). Productivity losses from mercury toxicity are 28% larger than the 18.1 Mt a^{-1} GPP reductions resulting from direct mining deforestation (see Figure 3-4a), and these two losses represent 0.20% and 0.16% of the 11.4 Gt a^{-1} total Amazon GPP[94]. The fractional change in Amazon net carbon flux may be even larger, since GPP nearly equals respiration making the net flux highly sensitive to changes in either term.

Approximately 10% of Amazon GPP stores in medium term woody biomass[95] with a residence time of 50 years.[96] We therefore estimate that mercury reduced Amazon woody carbon storage by 2.32 ± 0.06 Mt a^{-1} in 2024 and a 20.9 ± 0.5 Mt a^{-1} in aggregate since 2001 (see Figure 3-4b). We assume that informal alluvial gold mining's slash-and-burn deforestation followed by excavation of the top few meters of soil rapidly—within the year of mining—release all carbon stored in above and below-ground biomass. We calculate the pre-mining biomass stock at each pixel by averaging 2010 gridded biomass estimates[97] across all forested pixels within 120 kilometers of the target mined pixel. We thereby estimate that direct mining scars account for a 7.39 Mt a^{-1} reduction in carbon stored in Amazon biomass and a 93.8 Mt reduction over the study period (see Figure 3-4b).

Whereas annual GPP reductions due to mercury toxicity (which reflect a 10–15-year weighted average of mining activity) exceed those due to direct mining deforestation (which reflect the aggregated mining history), the immediate net carbon emissions pulse in the year of deforestation exceeds the net carbon emissions from mercury degradation. Our estimates for carbon storage loss due to Amazon mercury degradation represent approximately 6% of an estimated 42 Mt a^{-1} biomass storage loss from all Amazon degradation sources (excluding deforestation); on the other hand, mining deforestation accounts for 13% of an estimated 55 Mt a^{-1} biomass stock loss from all Amazon deforestation sources.[98] Together, the combined net carbon emissions associated with mining deforestation and mercury degradation represent 9% of an estimated 100 Mt a^{-1} net carbon flux due to all Amazon land use change.[98]

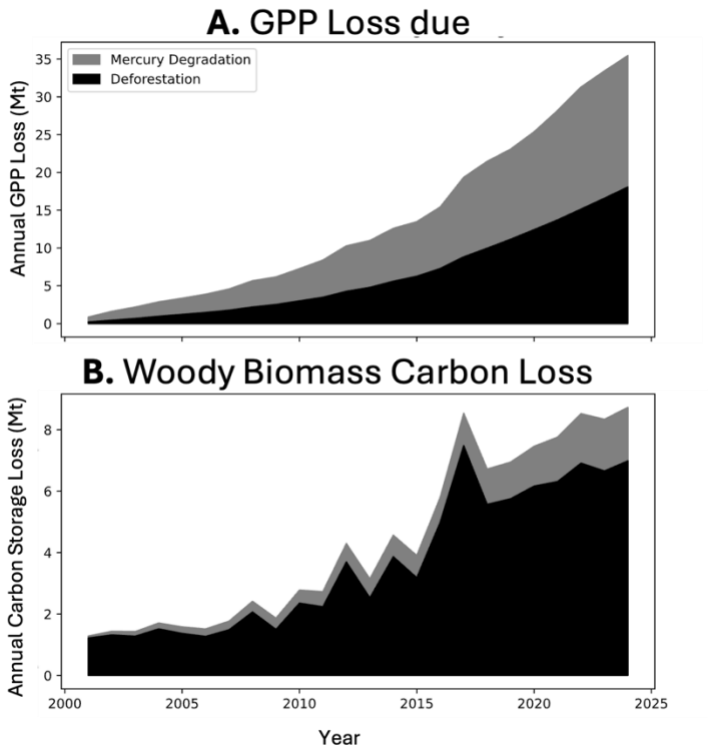

Figure 3-4. This figure shows gross primary productivity (GPP) loss in panel A and lost biomass carbon storage in panel B due to Amazon gold mining between 2001 and 2024. The impacts of direct mining deforestation are shown in black, and the impacts of mercury degradation are shown in grey.

3.3.4. Additional Predicted Environmental Impacts

The mercury-induced plant productivity disruptions established in this paper may have further consequences that extend beyond lost carbon assimilation. The 0.20% of Amazon forest GPP loss found in section 3.3.3 may induce an even larger percent reduction in the forest's fruit production, as observed in a soil-mercury study of tomato plants[99]; this differential effect could reflect plants prioritizing survival over reproduction during times of stress. Cropland productivity and associated food security may also be threatened, if they experience similar percent physiological limitations at the same mercury doses as seen in forests (see SI section 6.2.1 for speculated cropland impacts). Productivity impacts may extend beyond the Amazon; a proportion of mining emissions enter the global mercury cycle and could reduce aggregate global productivity by nearly double Amazon productivity losses, if the same toxicity response occurs in global plants (see SI section 6.2.2).

Additionally, interruptions to plants' carbon assimilation may reduce transpiration threatening downwind forests that depend on the resulting rainfall. We quantify the approximate impact of this potential hydrologic feedback under the simplifying assumption that plants behave according to optimal stomatal model theory[100]; this theory stipulates that declines in the rate of carbon assimilation trigger a mix of short-term stomatal closure and long-term stomatal density downregulation over multiple

leaf life-cycles. This theory further predicts that transpiration will therefore decrease at the same rate as carbon assimilation loss, which has been confirmed by empirical measurements for other types (not mercury) of carbon assimilation limitations.[101] We therefore hypothesize that transpiration declines due to mercury degradation and mining deforestation deplete the atmospheric rivers that drive up to 70% of downwind Amazon precipitation during dry months[102] with the impacts concentrated in the most vulnerable drying forests (see Figure 3-5).

We predict that these mining-related precipitation declines will accelerate the Amazon towards a die-off tipping point.[103] We follow past research[104] that estimated the forest-to-savannah transition zone occurs between -350 and -450 maximum cumulative water deficit (MCWD) beyond which soils and biomass dry to the point that fire ignitions spread to potentially irreversible stand-level conversion into savanna.[105] We further assume a continuous 1% per mm MCWD reduction in the long-term probability that a pixel is forested between -350 and -450 mm—note that MCWD regimes speak to long term stability of an ecosystem and actual transition depends on intermittent ignition events, potentially allowing a forest to remain below this range for years before it converts to savanna. Under these assumptions, we estimate that direct mining deforestation (44% of the estimated impact) and mercury degradation (56% of the estimated impact) push approximately 1500 km^2 of Amazon to rainfall regimes that can no longer sustain rainforest (see SI section 6.2.3). The scale of impact may accelerate as the Amazon moves towards tipping point, previously estimated 22-28% forest loss,[103] where cascading hydrological feedback has been predicted to accelerate forest loss to savanna.

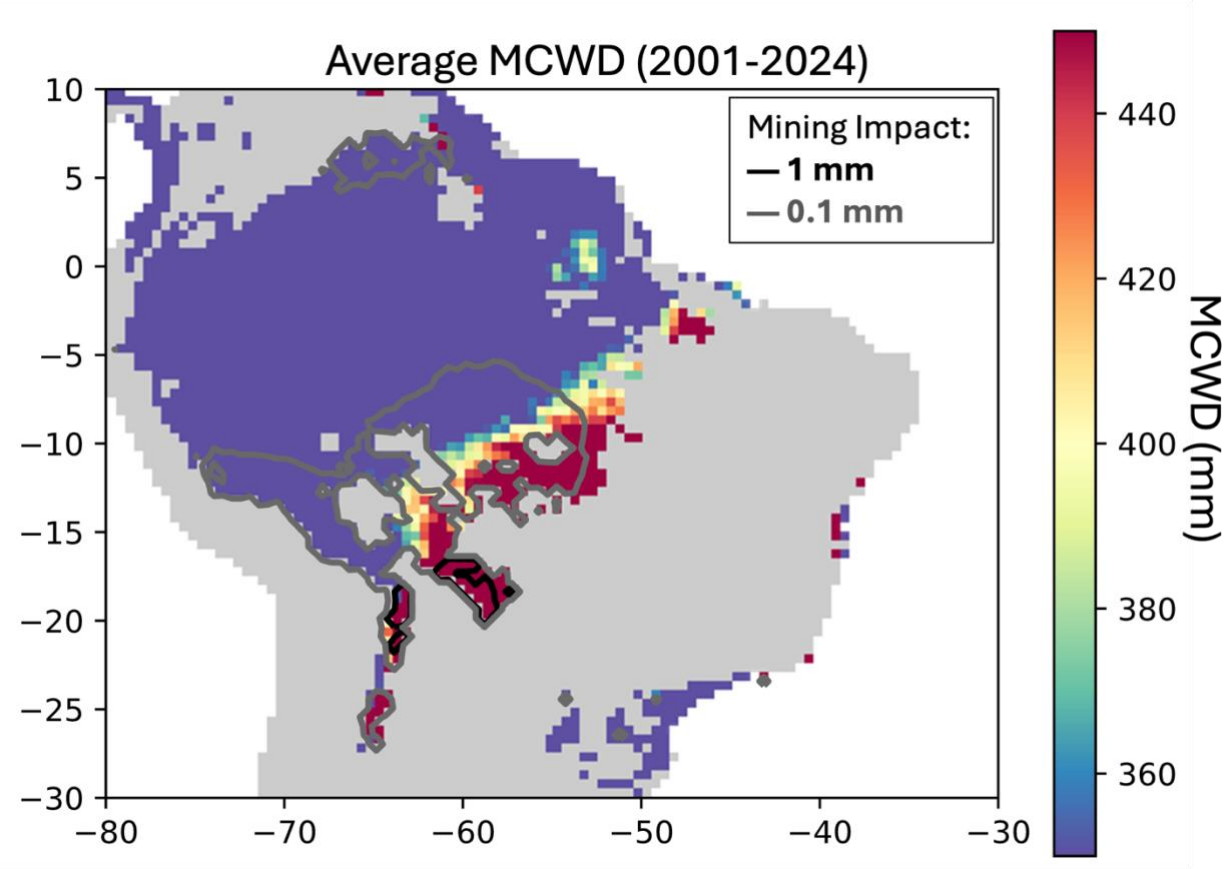

Figure 3-5: This plot shows the average 2001-2024 Maximum Cumulative Water Deficit (MCWD) in South American forests with grey indicating non-forested pixels, red indicating pixels exceeding water deficits that support forests, blue indicating deficits that forests can sustain, and the blue-purple-red gradient indicating the predicted transition zone where forests transition to savanna.[104] Grey and black contours represent speculated average MCWD increases of 0.1 and 1 mm (restricted to forested areas where it was calculated) resulting from upwind reductions in transpiration from mining deforestation and mercury degradation.

3.3.5. The Regional and Global Costs of Productivity Loss

Plant productivity loss from informal gold mining may profoundly impact communities living nearby. We hypothesize that GPP losses in Amazon forests propagate up the food chain, potentially impacting the abundance of fruits for foraging, fauna for hunting, and other ecosystem services; furthermore, these forest impacts on food security may be compounded by reduced crop yield if agricultural plant productivity is affected at a similar rate as forest productivity is impacted (see SI section 6.2.1). The hydrological feedbacks discussed in section 3.3.4 present short-term hazards, where worsened droughts can affect river navigability and increase wildfire risk. These externalities threaten regional livelihood security, which has in turn been shown to drive people towards gold mining,[64] potentially creating a self-reinforcing socio-ecological feedback loop.

Section 3.3.3's estimated 9.7 Mt a^{-1} lost biomass storage due to mining deforestation and mercury degradation represents a net CO_2 emission of 35.6 Mt a^{-1} (one gram of carbon is contained in 3.67 g of CO_2). This net emission accelerates climate change,

carrying a portion of gold mining's externalities to the global scale. The social cost of lost long-term carbon storage loss has been estimated at $185 (CI: [$44, $413]) per ton of CO_2.[106] Applying this valuation to the combined 35.6 Mt a^{-1} of net annual CO_2 storage loss, we estimate a $6.1 (CI: [$1.4, $14]) billion per year social cost from this net emission.

This social cost turns out to be comparable with the market valuation of gold produced. Amazon alluvial gold mining produces approximately 80 tonnes of gold per year—calculated by applying a 1-to-1 mercury-to-gold ratio in amalgam[45,107] to Chapter 2's 80 tonnes per year mercury emissions from mining. At gold's (approximate 2026) price of $4000 per troy ounce, this mining produces $10.3 billion per year (in market valuation) of gold production or $137 billion for the aggregate 1,050 tonnes of gold extracted between 2001 and 2024. The $6.1 billion per year social-cost-of-carbon externality therefore accounts for approximately 59% of the market valuation of gold produced annually. If we incorporate the social cost of further speculated impacts (see section 3.3.4), the social cost of gold-mining-associated productivity declines is an even larger fraction of the valuation of gold produced. Indirect global GPP declines due to mercury introduced into the global atmospheric cycle could account for an additional 26% of gold's market valuation, Amazon forest die-off due to downwind hydrologic stress could account for an additional 18% of gold's market valuation (aggregating both metrics across the 25 year mining history as described in SI section 6.2.3), the GDP value of speculated agricultural productivity loss could account for an additional 0.3% of gold's market valuation (see SI section 6.2.1), and other ecosystem service loss could account for an additional (unquantified) externality. Together, the social externalities of gold-mining-related productivity declines in the Amazon are on par with the total market valuation of the gold it produces. Furthermore, these social costs add on top of other regional externality estimates[108] that were previously calculated to alone rival the value of gold produced.

Furthermore, market valuation may overestimate gold's true social value. Approximately 60% of 2025 gold purchases were made by investors and national banks, 33% went towards jewelry[109], and only 7% purchased for technology; as a result, gold demand and price are driven primarily by its investment value rather than acting as a productive commodity.[110] Furthermore, gold investment is not productive in the sense of supporting the generation of future goods and services, and therefore produces little social value; instead, it offers private value based on its speculated future valuation[111] where one investor's gain is another's loss. Even if gold does not offer broader social value, the economic development it brings mining regions might be argued to support regional economic growth (effectively redistributing social value from wealthy countries that buy gold to marginalized mining communities). However, the value for the mining communities themselves is contested, as the short-term economic growth offered by extractive industries has been found to breed a "resource-curse" dependence that

inhibits long-term development.[112] If the market valuation of gold overstates its societal value, the externalities calculus on the net social value of gold becomes even less favorable.

Our findings illuminate impacts of gold mining that extend beyond dietary mercury exposure and deforestation. The regional impacts of associated mercury emissions combine with direct deforestation to threaten forest productivity, ecosystem services, and food security. Our carbon analysis connects these regional impacts to the global climate impacts of mining, highlighting that the externalities from gold mining do not remain local. The forest productivity impacts from mining join a growing body of literature questioning if gold consumption is worth the associated human and ecological costs.

Chapter 4. Terrestrial Cycling and Fate of Mercury in the Amazon

4.1. Introduction

Amazon gold mining releases approximately 80 tonnes per year of mercury into the atmosphere, with a particularly high density of emissions in the Madre de Dios mining region of Southeast Peru (see Chapter 2). This emitted mercury vapor elevates nearby air concentrations,[15] increases mercury levels in foliage,[19,113] and augments litterfall loading rates into Amazon soils.[18,19] Counterintuitively, prior Amazon studies have not been able to explain the variation in soil mercury concentrations from differential mining inputs, either not directly quantifying this impact[19,113] or finding it to be insignificant with available data.[18]

Soils represent the largest terrestrial mercury sink[114] and provide anoxic conditions that allow microbial mercury methylation, acting as a source for bioaccumulation within the terrestrial food chain.[115] Soils can further erode mercury into rivers[116] threatening aquatic food chains.[117] These accumulation pathways may introduce human-exposure risk, where elevated human-hair concentrations have been previously associated with both mining proximity and the frequency of fish consumption[118] (the connection to meat consumption remains less studied). Assessing the human and ecosystem risks of soil mercury contamination requires an accurate spatiotemporal characterization of soil loading, soil-mercury retention, and the pathways of soil-mercury loss into the regional and global mercury cycle.

This chapter reconciles measured soil mercury concentrations with the inflowing and outflowing fluxes that drive them. We hypothesized that combining a gradient flux method and an isotope mixing model would allow us to improve prior estimates of Amazon foliar uptake and offer the first Amazon estimate of soil evasion and nonstomatal dry deposition; we further hypothesized that the frequently overlooked nonstomatal dry deposition represents the leading input flux into Amazon forests, as has been seen in temperate deciduous forests.[119] We extended these flux estimates across the Amazon, producing annual 1-km resolution loading estimates; these maps allow us to estimate the fraction of emissions depositing back into the Amazon rather than entering the global mercury cycle. We hypothesized that these atmospheric loading maps can predict observed surficial soil-mercury enrichment, but that intra-site variation is also driven substantially by local topographic features and deforestation. Specifically, we hypothesized that deforestation increases evasion, resulting in Amazon-wide mercury emissions relevant to mercury budgeting. By quantifying these different fates of loaded mercury, our results can support regional risk assessment of

terrestrial and aquatic exposure while informing global mercury budgeting by clarifying how regional emissions enter the global cycle.

4.1.1. Graphical Abstract

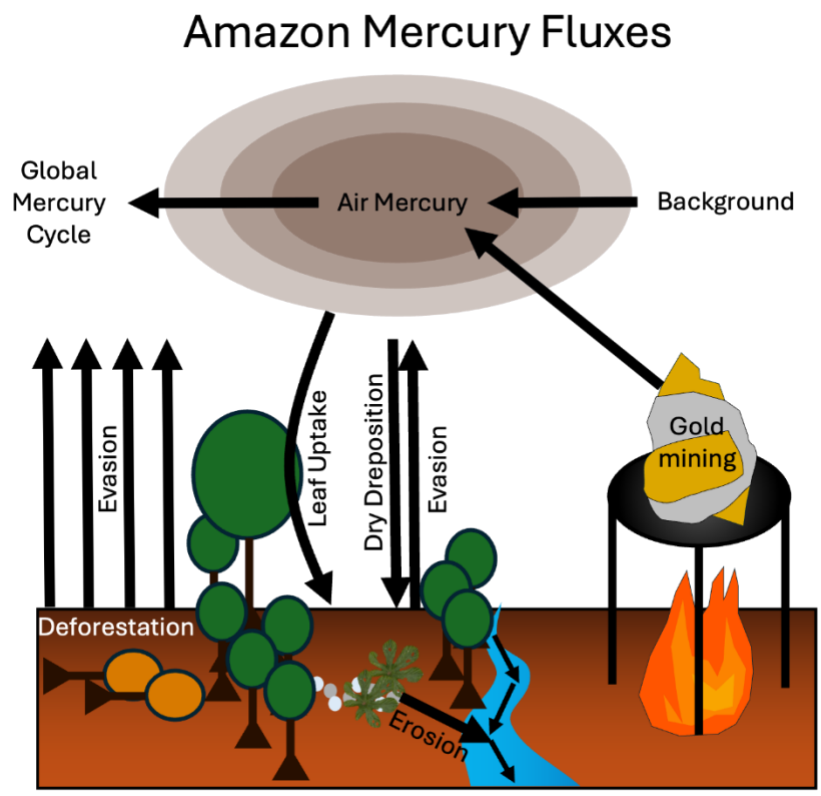

4.2. Methods

4.2.1. Field Sampling and Prior Dataset Inclusion

We collected soils at 3 depths (0-5 cm, 5-10 cm, and 10-15 cm) along with bulk litter during the end of the dry season (September 2025) at 6 forested sites across Madre de Dios, Peru (see Figure 4-1 for sampling sites and measurements sampled). At 4 of 6 sites, we also sampled neighboring deforested plots. We collected five replicates of bulk litter and soil at each depth per forested and deforested plot. We analyzed all soil and litter samples for total mercury (see section 4.2.6) and loss on ignition (see section 4.2.7); we measured surficial-soil pH using a digital soil pH meter (Lawnfull, an industrial grade meter that combines frequency domain reflectometry for soil moisture and alternating current detection for conductivity); and we aggregated each plot's five samples per depth (leaf litter, 0-5 cm, 5-10 cm, and 10-15 cm) to measure a plot-level mercury isotope average (see section 4.2.6). We deployed passive air mercury samplers (MerPas) between 3 and 15 months between 2023 and 2025 at 5 of 6 sites (samples were not successfully recovered at the near-background CM2 tower site) from which we measured the average air-mercury concentration during the deployment period as well as mercury isotopes; at 3 of 6 sites, we deployed passive air samplers at

a 58-m height during the corresponding sampling period, allowing us to compare between ground-level and above-canopy air.

To extend our spatial coverage in the Madre de Dios region, we combined our six measurement sites with 2018-2019 soil, litter, and air measurements from 7 prior study sites.[19,113] Figure 4-1 shows the location of our study sites alongside these prior sites, along with a list of the data collected at each site and where data was sourced.

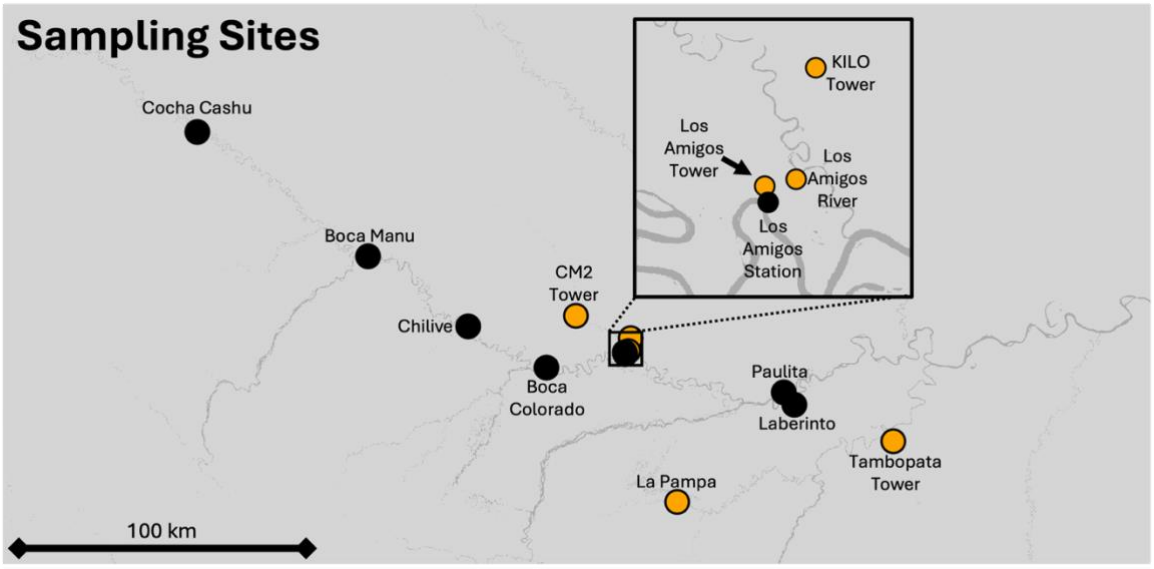

Site	1.75 m Air Hg (ng m^{-3})	Above Canopy Air Hg (ng m^{-3})	THg source	Isotope Source	Deforested Plot
Boca Colorado	18.0	N/A	Gerson et al	Szponar	Yes
Laberinto	9.6	N/A	Gerson et al	Szponar	Yes
La Pampa	4.4	N/A	Authors	Authors	Yes
Los Amigos Station	2.7	N/A	Gerson et al	Szponar	Yes
Los Amigos Tower	2.2	3.5 (58 m)	Authors	Authors	Yes
Tambopata Tower	1.7	2.8 (53 m)	Authors	Authors	Yes
Paulita	1.7	N/A	Szponar	Szponar	No
Kilo Tower	1.7	2.9 (58 m)	Authors	Authors	No
Los Amigos River	1.5	N/A	Authors	Authors	No
CM2 Tower	N/A	N/A	Authors	Authors	Yes
Chilive	0.8	N/A	Gerson et al	Szponar (surficial only)	Yes
Boca Manu	0.8	N/A	Gerson et al	Szponar	Yes
Cocha Cashu	0.5	N/A	Szponar	Szponar	No

Figure 4-1. This figure shows the sampling locations and their site names where soils, litter, and air mercury measurements were taken by authors (in orange) and prior studies[19,113] (in black). Below we include a list of the sites, the ground-level (1.75-m height) air concentrations; the above-canopy air-mercury concentrations (53 or 58-m height depending on the site); the source of total mercury (THg) measurements: either authors, Gerson et al,[19] or Szponar[113]; the source of air, soil, and litter isotopes: either authors or Szponar[113]; and whether total mercury concentrations from a neighboring deforested plot are available (from the same source as THg measurements).

4.2.2. Flux Tower Measurements Collected

Flux measurements were collected at the Los Amigos flux tower (-12.5603, -70.1031), which sits within the Los Amigos Conservation Concession. The tower consists of a metal bar lattice, minimizing potential wind disruption, and the inlets were installed on rods set 1 meter away from the tower. An approximate 5–10-meter radius clearing surrounds all sides of the tower, which otherwise sits within pristine forests. The tower is positioned approximately 1 kilometer to the northwest of the Los Amigos Biological Station, 700 meters north of the Madre de Dios River, and 1 kilometer north of active mining sites—which are largely restricted to the southern bank of the river.

To quantify the vertical movement of mercury into and out of soils, we deployed a continuous gaseous mercury analyzer (Tekran 2537A) on the Los Amigos flux, alternating measurements at 16 m (below canopy) and 58 m (above canopy) for 10 minutes each. This 10-minute period corresponded to one 5-minute reading for each of the instrument's two gold traps (we ignore the first trap's readings due to a potential stagnant-air bias noted below).

Air sampled at 16-m passed through approximately 40 meters of tubing, which could bias instrument readings if stagnant past air was measured (the 58-m inlet only needed a few meters of tubing). We minimized the bias by sampling at a 5 $\mathrm{L\ min^{-1}}$ flow rate through 0.1875-inch Teflon tubing. As a result, only 0.8 L air remained in the tube fed to 16 meters when it was not being sampled, representing 3% of the total air volume sampled for each 5-minute measurement. We further corrected any potential stagnancy bias by ignoring the first measured concentration measurement at each height (which always excluded the same gold trap ensuring cross-height consistency).

For analysis, we averaged concentrations at both heights to the hourly timescale. This allowed us to compare mercury gradients with average mixing rates derived from hourly ERA5[120] meteorological data (see section 4.2.3).

Prior to deployment, we manually calibrated the instrument by injecting a known volume of air equilibrated to liquid mercury at a known temperature (using a Tekran 2505 mercury vapor primary calibration unit). Automatic calibrations were initially run daily, but an instrument computer-chip issue interrupted calibrations during deployment. Between calibrations across an 8-month initial deployment period (Sept 2023-May 2024), we observed a drift of less than 1% across calibrations including after a 5-month period of instrument downtime; therefore, we accepted 1% as the instrument precision for the purpose of our analysis. Since both heights were measured in alternation, any drift would scale equally for both, meaning that gradient comparisons are scaled by the same drift factor meaning inter-height comparisons can still be made. Furthermore, in extending tower estimates to other regions, we scaled

fluxes by 58-m concentrations which cancels out any theoretical additional bias in regional modeling.

Mercury gradient data was collected during June 2024 and September 2024 through January 2025 with occasional outages due to power or instrumentation issues. An average mercury gradient between 16 and 58 meters, *dC(t)/dz*, was calculated by dividing the difference of mercury across heights by the 42 m height differential; we then averaged measured gradients over an hour aggregation period.

We converted gradient data to fluxes (see section 4.2.3) by backing out mixing rates from heat gradient and heat flux data collected at the same flux tower. Heat fluxes were measured with an eddy flux covariance system (Licor 7500) deployed at 58 meters. This eddy flux setup averages the covariance in vertical wind speed with temperature, quantifying the heat flux by analyzing the differential temperature of upward versus downward drafts.[121] We measured temperature at 16- and 58-meter heights using Hobo pendant temperature sensors, with the temperature gradient similarly averaged to the hour. Both the heat flux and heat gradient data were measured hourly between June 2 and December 15, 2024, providing a large dataset to calibrate vertical mixing estimates.

4.2.3. Gradient Flux Calculation

The 5-minute measurement time for mercury concentrations precluded the application of the eddy-flux-covariance method[121] to estimate mercury fluxes (this method requires approximately 10 measurements per second). Instead, we used a gradient-flux method[122], which estimates the net flux (of mercury, heat, or other tracers) moving across the measured air column with only the average vertical mercury gradient, $dC(t)/dz$, and the eddy diffusivity (mixing rate), *K*:

$$\text{Flux}(t) = -K(t) * dC(t)/dz.$$

For heat, both the flux and the concentration gradient were measured (see section 4.3.1), allowing us to estimate the eddy diffusivity, *K*, for heat. We assume the Reynolds' analogy[123] holds, which says that the vertical mixing of a tracer of interest (mercury) follows the same turbulent air movements as the mixing of heat. Under this assumption, we can apply the eddy diffusivity for heat to the vertical mercury gradient to calculate the mercury flux for each hour where gradients were measured.

Unfortunately, a naïve approach that directly divides the heat flux by the temperature gradient produces non-physical diffusivities during times when the temperature gradient and flux approach their (approximately coinciding) zero crossings. Slight deviations or noise in flux and gradient estimates push the hourly diffusivity estimates negative (when flux and gradient have opposite signs near zero) or towards infinity (as the concentration gradient approaches 0 but with small non-zero flux). However, true eddy diffusivities are always positive and bounded (Fick's law for mercury and the

second law of thermodynamics for heat). The unphysical diffusivity estimates near zero-crossings lead to unbounded estimates for mercury flux around these transition points.

To address this non-physical diffusivity issue, we follow an amended process of calculating heat fluxes. Instead of directly calculating the diffusivity by dividing the flux by the gradient, we use the flux and gradient to calibrate a diffusivity model, which depends on relevant ERA5[120] meteorological data. In addition to correcting non-physical diffusivity calculations, this additional calibration step may be extended to estimate mixing across other Amazon sites (see section 4.2.9). This model utilizes the Obukhov similarity theory,[124] where eddy diffusivities are modeled by:

$$K = k\,\mu_* z_g \frac{1}{\phi(\frac{z_g}{L})}$$

In this model, k=0.4 is the Van Kármán constant, μ_* is the friction velocity, z_g is the geometric mean of 16-m and 58-m sample heights with respect to a zero-displacement height, z_d, where wind speeds are theorized to be 0, L is the Obukhov length, and ϕ is a stability function that measures the stability of air columns to thermal-induced cycling. We estimate the friction velocity μ_* and the Obukhov length L from hourly ERA5 data following ERA5's recommended method.[125] Stability functions have been empirically modeled[126] as:

$$\phi(\frac{z_g}{L}) = \begin{cases} \left(1 - c_1 \frac{z_g}{L}\right)^{-p_1} & : L < 0 \\ \left(1 + c_2 \frac{z_g}{L}\right)^{p_2} & : L > 0 \end{cases}$$

where c_1, c_2, p_1, and p_2 are unitless empirical parameters derived from flux and gradient data. Unfortunately, prior modeling[126] has assumed that the measurement height is substantially above a zero-displacement height, which is assumed to be approximately 2/3 of the canopy height. At the Los Amigos site, the canopy is approximately 30 meters tall, meaning that our lower 16-meter measurement height is below the theorized 20-meter displacement height.

This lower measurement height ensured that there was a greater observed gradient, improving the gradient's signal-to-noise ratio for analysis. However, the low measurement height also means that we cannot directly apply existing empirical coefficients; instead, we calibrate diffusivity parameters c_1, c_2, p_1, and p_2 with the geometric mean height, z_g, in reference to the ground and an additional α accounting for model divergence from an unknown effective zero-displacement height (the Van Kármán constant is also wrapped into this α coefficient):

$$K_{modeled}(t, \alpha, c_1, c_2, p_1, p_2) = \frac{\alpha\ \mu_*(t)}{\phi(\frac{z_g}{L(t)}, c_1, c_2, p_1, p_2)}$$

To calibrate these 5 parameters, we minimize the least squared error in predicting the hourly sensible heat flux, $F_{Heat}(t)$, from the heat gradient, $\frac{d\theta(t,z)}{dz}$, and the modeled diffusivity, $K_{modeled}$, by minimizing the time-averaged least squared error of:

$$F_{Heat}(t) = K_{modeled}(t, \alpha, c_1, c_2, p_1, p_2)\frac{d\theta(z,t)}{dz}$$

SI section 6.3.1 presents the calibrated parameters, compares them to prior Obukhov similarity theory parameterizations at higher measurement heights,[126] and discusses model accuracy in predicting heat flux (to justify this method being applied for mercury flux calculations).

4.2.4. Using the Gradient Flux Method to Estimate Mercury's Dry Deposition, Stomatal Uptake, and Evasion

We estimate the average gaseous elemental mercury flux across available data (June 2024 and September 2024-January 2025). We break this net flux estimate into its (negative) evasion component, its stomatal uptake component, and its direct dry deposition component by calculating the former two and backing out the latter from the total flux.

We estimated the evasion flux by first calculating the mercury concentration where there is net neutral flux; at this concentration, the magnitude of evasion equals dry deposition plus litterfall. The neutral-flux concentration is equivalent to the zero-gradient condition, which we calculated as the x-intercept of a regression of air-gradient, $\frac{dC}{dz}$, versus concentration, $C(58\ \mathrm{m})$:

$$\frac{dC}{dz} = \beta\ C(58\ \mathrm{m}) + C$$

In this regression, β is the concentration-to-gradient conversion slope, C is a constant (the air-mercury gradient at zero 58-m mercury concentration), and the x-intercept is $-C/\beta$. As 58-m concentrations rose, the gradient rose in a predictable linear manner and the residuals of the regression had negligible covariance with eddy diffusivity. This negligible covariance means that the average predicted gradient can be directly multiplied by the average eddy diffusivity (see section 4.2.3) to calculate the evasion flux, without having to worry about the prediction error interacting with the diffusivity values.

To estimate the stomatal uptake flux, we followed a similar procedure as used for soil evasion. We measured the difference between the zero-flux condition (x-intercept) for day versus night (6 AM to 5 PM and 6 PM to 5 AM, respectively, which remains relatively

consistent across the year at this near-equatorial site). We assume this difference is driven only by differential stomatal uptake (i.e. dry deposition depends only on air-mercury concentrations and soil evasion is relatively independent of the diel cycle), which allows us to estimate the stomatal uptake flux using the following steps. The difference between the daytime and nighttime x-intercepts is multiplied by the daytime gradient-versus-concentration β coefficient to predict the (daytime) increase in the vertical-mercury gradient due to stomatal uptake at the (daytime) x-intercept concentration. Assuming stomatal uptake scales proportionally with daytime air concentrations (see section 4.2.5), the average gradient increase at actual observed concentrations is calculated by multiplying the gradient at the (daytime) x-intercept by the ratio of average 58-meter mercury concentration divided by that x-intercept concentration. This daytime stomatal-uptake-induced gradient increase is further multiplied by the average daytime eddy diffusivity to calculate the daytime stomatal uptake flux, which is divided by two (averaging daytime stomatal uptake with no nighttime uptake) to calculate the average stomatal uptake across day and night.

Finally, we calculated the dry deposition flux by subtracting the stomatal uptake flux and evasion flux, with errors calculated in quadrature. All standard errors were calculated with a Newey-West[127] temporal correlation adjustment (correcting for autocorrelation with up to a 1-day lag time).

One potential limitation of this method is that it only accounts for leaf mercury that travels through stomata, and it would label any gaseous mercury absorption (or reemission) on the leaf surface (e.g. wax) as dry deposition (or evasion respectively). However, a prior temperate forest study[128] found that 90-96% of leaf mercury is continued inside leaf tissue rather than on the surface; assuming that result extends to the Amazon, these other gaseous uptake pathways may be negligible. This assumption was validated by comparing the gradient flux estimate that only included stomatal uptake to total litterfall flux estimates that include all leaf pathways (see sections 4.2.8 and 4.3.2).

4.2.5. Extending Fluxes to the Broader Amazon.

We extended estimates from the Los Amigos site to the broader Amazon by considering the drivers of each flux. Dry deposition and stomatal uptake fluxes were assumed to be proportionally based on air mercury concentrations, consistent with a conceptual model that there is an abundance of receptors where mercury can bind across the range of mercury loading rates. In that case, for each fractional increase in available atmospheric mercury near the uptake interface, we anticipate the same fractional increase in mercury that actually binds via that pathway. The assumption is corroborated with inter-site data in section 4.3.2 for stomatal uptake and based on the proportional air-gradient to concentration relationship witnessed in Chapter 2 for the net flux.

We model stomatal uptake growing proportionally with air mercury concentrations, $\mathrm{Hg_{air}}$, and with a deposition rate β_{stom}:

$$\text{Stomatal Uptake}(\mathrm{Hg_{air}}) = \mathrm{Hg_{air}} * \beta_{stom}$$

We similarly model dry deposition as growing proportionally with air concentrations above the canopy, $\mathrm{Hg_{air}}$, with a deposition rate, β_{dd}:

$$\text{Dry Deposition}(\mathrm{Hg_{air}}) = \mathrm{Hg_{air}} * \beta_{dd}$$

Whereas dry deposition and stomatal uptake were modeled to depend only on air-mercury levels, soil evasion may depend on a variety of factors including surficial mercury concentrations (if all surficial mineral soils have a similar rate of evasion), loading rates (if recently deposited mercury evades more quickly than long term stores), or other soil properties. Due to multiple confounding potential loss pathways (e.g. erosion and evasion) that depend on several parameters, we do not directly quantify total evasion across sites. We only provide this total evasion flux for the Los Amigos tower site, but we offer an order of magnitude for equilibrium soil residence times at other sites (see SI section 6.3.2). We also evaluate spatial drivers of spatial variation for two loss pathways: evasion (see section 4.3.7) and erosion (see 4.3.5 and 4.3.6).

For the purposes of extrapolating overall flux rates from the Los Amigos tower site to other regions, we assume that an increase in 58-m air concentration induces the same increase in vertical mercury gradient regardless of the site. This simplification allows for an unknown baseline mercury evasion rate (that could depend on soil-mercury concentrations or other soil properties) but assumes that an increase (due to nearby mining) of atmospheric loading predictably increases evasion.

4.2.6. Total Mercury and Mercury Isotope Analysis

Air samples were prepared and analyzed for total mercury as noted in Chapter 2. The same reverse aqua-regia traps (4:3:1 milli-Q water: nitric acid: hydrochloric acid) used for total mercury analysis were used to analyze air isotopes.

Soil and litter samples were freeze dried, homogenized, and analyzed on a Nippon MA-3000 direct mercury analyzer for total mercury as in Chapter 3. Soil and leaf litter isotope analysis required separate preparation steps than for total mercury analysis. Dried samples from each site and depth (0-5 cm, 5-10 cm, 10-15 cm, and leaf litter) were aggregated (5 samples per aggregation). Aggregate samples were microwave digested at approximately $55°C$ for 4 hours in a 3:1 nitric acid: hydrochloric acid solution. After digestion, bromine chloride (10% of solvent volume) and milli-Q water (100% of prior solvent volume) were added to further oxidize and dilute the sample. To pre-concentrate and purify the digested mercury matrix for isotope analysis, we followed a previously established protocol[129] that reduced the samples in

hydroxylamine and tin chloride, vaporized the solution, and sorbed the resulting mercury onto gold traps. Gold traps were subsequently desorbed into a 30% nitric acid, 10% bromine chloride, 60% milli-Q water solution. To avoid bias due to potential fractionation during the purification step, we only included samples with 85-115% recovery; this resulted in the exclusion of La Pampa litter samples, so we used aggregated live-leaf (*Cecropia* and *Gynerium*) samples in place of bulk litter for isotope fractions (but not total mercury) at that site.

Mercury isotopes were analyzed following prior methods and quality control procedures.[119] A multi-collector inductively coupled mass spectrometer (MC-ICP-MS) was used to determine mercury isotope values. After every 5 samples, a NIST RM 8610-UM standard was run; standard measurements off by more than $0.1‰$ were rejected and required a rerun of surrounding samples, and accuracy of standards was used to calculate the precision of sample isotope concentrations (ranging from $0.01‰$ to $0.07‰$ depending on the sample). Note that isotope fractionations are reported in per mille (‰) units which means a multiplication by 1000 is built in.

Mass dependent fractionation (MDF) for air, soil, and leaf litter was calculated in comparison to reference material NIST-3133:

$$\delta^{202} = \frac{\left(^{202}\mathrm{Hg}/^{198}\mathrm{Hg}\right)_{\mathrm{sample}}}{\left(^{202}\mathrm{Hg}/^{198}\mathrm{Hg}\right)_{3133}} - 1$$

For passive air samplers, a 1.18 ‰ correction was applied to δ^{202} estimates to account for a mass dependent fractionation when air passes through the passive sampler membrane[113] that would otherwise bias results (for mass independent fractionation, this effect cancels out, and no correction was necessary).

Mass independent fractionation (MIF) for air, soil, and leaf litter was calculated as:

$$\Delta^{199} = \delta^{199} - (\delta^{202} * 0.252)$$

$$\Delta^{201} = \delta^{201} - (\delta^{202} * 0.752)$$

4.2.7. Soil Organic Carbon Analysis

To proxy for soil organic matter concentrations, we measured loss on ignition. First, we oven dried soils at $105°$ C for 12 hours (to remove additional water post-freeze drying), placed heated soils immediately in a desiccator to cool and then weigh as a baseline. Dried soils were then burned at $550°$ C for 12 hours, cooled to between 100 and 200° C in the oven, placed in a desiccator to cool further, and weighed again. Comparing pre-burn dry-weight to post-burn weight allowed us to calculate loss-on-ignition. A known limitation of this method is the potential for crystal water to persist during oven drying and burn off at 350-650° C,[130] meaning that the LOI results could overestimate true soil organic matter concentrations.

4.2.8. Leaf Endmember Modeling from and Soil and Air Inputs

We consider a two-end member model for leaf mercury where it may absorb air-mercury through stomata (proportional to atmospheric mercury levels) and soil mercury through roots and stems (proportional to soil mercury levels). Leaf litter mercury concentration, $\mathrm{Hg_{leaf}}$, is modeled to increase with average air mercury concentration, $\mathrm{Hg_{air}}$, at a rate of β_{air} and with soil mercury concentration, $\mathrm{Hg_{soil}}$, by a rate of β_{soil}

$$\mathrm{Hg_{leaf}} = \mathrm{Hg_{air}} * \beta_{air} + \mathrm{Hg_{soil}} * \beta_{soil}$$

This implies isotope mixing ratios of

$$\delta^{202}{}_{\mathrm{leaf}} = \frac{(\delta^{202}{}_{\mathrm{air}} + \mathrm{MDF_{leaf}}) \times \mathrm{Hg_{air}} \times \beta_{\mathrm{air}} + \delta^{202}{}_{\mathrm{soil}} \times \mathrm{Hg_{soil}} \times \beta_{\mathrm{soil}}}{\mathrm{Hg_{air}} \times \beta_{\mathrm{air}} + \mathrm{Hg_{soil}} \times \beta_{\mathrm{soil}}}$$

and

$$\Delta^{199}{}_{\mathrm{leaf}} = \frac{(\Delta^{199}{}_{\mathrm{air}} + \mathrm{MIF_{leaf}}) \times \mathrm{Hg_{air}} \times \beta_{\mathrm{air}} + \Delta^{199}{}_{\mathrm{soil}} \times \mathrm{Hg_{soil}} \times \beta_{\mathrm{soil}}}{\mathrm{Hg_{air}} \times \beta_{\mathrm{air}} + \mathrm{Hg_{soil}} \times \beta_{\mathrm{soil}}}$$

Where Δ^{199} and δ^{202} with leaf, air, and soil subscripts correspond to the respective measured mass-independent and mass-dependent fractionations for each medium. $\mathrm{MDF_{leaf}}$ and $\mathrm{MIF_{leaf}}$ are the a priori mass-dependent (δ^{202}) and mass-independent (Δ^{199}) fractionation offset that occurs during air-uptake into leaves. Leaf litter, passive air samplers, and soil samples were used for the respective total mercury, mass dependent, and mass independent fractionation measurements.

We estimated the uptake rate from air, β_{air}, and soil, β_{soil}, along with $\mathrm{MDF_{leaf}}$ and $\mathrm{MIF_{leaf}}$ using a likelihood estimator that combines log total mercury, δ^{202}, and Δ^{199} data. For total mercury, we used a log-least-squares likelihood estimator and for isotopes we used a standard least-squares estimator. We normalized each least squares estimator by the variance of (log) total mercury, (unlogged) δ^{202}, and (unlogged) Δ^{199} so that likelihood was comparable across the three mercury data types; we then estimated the model parameter values (β_{air}, β_{soil}, $\mathrm{MDF_{leaf}}$, and $\mathrm{MIF_{leaf}}$) that minimized the sum of normalized least-squares errors. This minimization corresponds to the maximum likelihood estimator (MLE) if residual variance is both normally distributed and represents a similar fraction of sample variance for each of log total mercury, δ^{202}, and Δ^{199}.

To calculate 95% confidence intervals, we applied Wilks' theorem,[39] comparing the resulting log likelihood estimator with the χ^2 distribution; to apply Wilks' theorem, we divided other parameterizations' sum of least-squares errors for log total mercury, δ^{202}, and Δ^{199} by the sum of squared error under the MLE parameterization. Under this method, the confidence interval includes any value for the selected parameter (β_{air}, β_{soil}, $\mathrm{MDF_{leaf}}$, and $\mathrm{MIF_{leaf}}$) where any parameterization produces a log likelihood estimate within $3.84/2$ of the maximum likelihood estimate.

4.2.9. Applying Lagrangian Transport to Estimate the Fate of Emissions

To estimate the regional uptake versus global atmospheric fate of mercury emissions, we couple a Lagrangian transport model (following Chapter 2's method) with ecosystem uptake rates. For each hour, we emit mercury based on emission sites and rates identified in Chapter 2. We advected particles based on their 100-m height ERA5[120] wind velocities. We distribute particles across the planetary boundary layer (PBL), ignoring initial vertical dispersion analysis that was relevant in Chapter 2—to better capture the high concentrations near to emission sites—but is not relevant on the longer timescales when most ecosystem uptake occurs. As in Chapter 2, particles leave the planetary boundary layer during deep convection, but we also accounted for particles exiting air columns due to ecosystem uptake.

We calculated the ecosystem uptake for any modeled hour by first converting the modeled 58-meter concentration to a modeled 16-to-58-meter vertical gradient, which we multiplied by a modeled eddy diffusivity. Depending on the hour of day when ecosystem uptake is being modeled, we applied the regression slope calculated from gradient data from only that hour of the day (accounting for differential stomatal uptake noted in section 4.2.4). We assumed that net ecosystem uptake scales proportionally with average 58-meter mercury concentrations over space (discussed in section 4.3.1 and evidenced by the relatively proportional concentration-to-gradient slope noted in Figure SI 6-5). We computed the eddy diffusivity with the parameterization from ERA5[120] data computed in section 4.2.3. Together these steps allowed us to model ecosystem uptake for each modeled hour after modeled mercury emissions from any pixel in the Amazon.

To estimate the total fraction of emitted mercury that loads into the Amazon, we track emitted particles for up to 2 weeks. We excluded any theoretical loading to pixels outside the Amazon. Modeled error included both error in gradient flux estimation rates (ste = 9%) and error in ERA5[120] planetary boundary height estimates (ste = 4.5% as seen in Chapter 2).

For loading maps, we followed this same analysis but with the added step of tracking advective position at a higher (1-km) resolution. Due to the storage and computational requirements in tracking loading at this high resolution, we only modeled loading occurring within the first day after emission. Sensitivity analysis revealed that 85% of total Amazon loading occurs in the first 24 hours, which was deemed sufficient for producing ecosystem loading maps (the remaining 15% that disperses after a day will be a small quantity spread over a wide distance).

4.2.10. Soil Mercury Prediction: Loading, Topography, and Deforestation

To predict the soil mercury gradient from loading data, we aggregated all modeled downwind loading from mining between 2001 and 2025. We distributed that cumulative loading estimate uniformly across the top 5 cm of soil assuming a 1.2 g cm^{-3} bulk density, consistent with past Amazon research.[131,132] To account for mercury

concentration footprint model error (see Chapter 2), we applied a correction factor (where noted in results) that divided observed air-mercury concentrations by modeled concentrations in the year measurements were taken. This correction factor was less than a factor of 2 at all sites except Boca Colorado, which is an urban emission site; Chapter 2 found that pixels near urban centers are particularly sensitive to model misspecification (from using night-time light as a proxy) of where gold shop emissions occur. We compared uncorrected and corrected predictions of soil accumulation with the observed gradient between 0-5 cm and a baseline 10-15 cm (5-20 cm for past study data[19,113]), via an ordinary least squared regression. We hypothesize that the two quantities will match provided that our atmospheric transport model accurately predicts soil loading, loading enriches only the top 5 cm of soil, and loaded mercury mostly remains in soils during the decadal timescale since mining began contaminating the region.

Loading was assumed to drive the soil-mercury gradient but not the inter-site variation in mercury at the 10-15 cm horizon. We compared that deeper horizon mercury concentration to pH, loss on ignition (soil organic matter proxy), and a relative elevation parameter to determine what drives baseline (pre-mining) mercury concentrations. The relative elevation parameter, hypothesized as a proxy for overland flows that may erode soil, was calculated as the elevation of a 30-m pixel[133] minus the minimum elevation of any pixel within 1 kilometer. The minimum pixel elevation within 1-km was often a river pixel, pixels approaching 80 m of relative elevation typically reflected hills and local high points, and pixels in between could be drainages during extreme rain events.

To understand the impact of deforestation on soil-mercury retention we compared neighboring forested and deforested plots at 0-5 cm, 5-10 cm, and 10-15 cm depth horizons. We estimated the number of years since deforestation at deforested plots based on local expert knowledge, visual identification on satellite images, and the Global Forest Change dataset.[30] We calculated the rates of change in evasion and lost deposition using an ordinary least squared regression comparing the difference in forests and deforested soil mercury concentrations at each depth against two variables: air-mercury levels and soil mercury levels, each multiplied by the length of time a plot has been deforested. Lost deposition was expected to scale with air-mercury concentrations and time, whereas increased evasion was expected to scale with soil-mercury concentrations and time.

Combining predicted soil gradients, estimated baseline levels due to topography, and modeled deforestation impacts, we modeled surficial (0-5 cm) soil concentrations across Madre de Dios and the broader Amazon. River pixels were excluded from baseline modeling. For regional modeling, the year of deforestation was sourced from global forest change[30]; however, the dataset fails to resolve the year of pre-2000

deforestation so for simplicity we assigned all those pixels to the year 2000 to estimate modern soil concentration. This simplifying modeling step likely overestimates true concentrations in pixels that were deforested long before 2000.

4.3. Results and Discussion

4.3.1. Estimating Fluxes at the Los Amigos Biological Station

Using the gradient flux method (see section 4.2.3), we find that the net (downward) gaseous elemental mercury flux at the Los Amigos flux tower is $184 \pm 25\ \mu g\ m^{-2}a^{-1}$ (see Figure 4-2 a, b, and c). This total flux is broken down into dry deposition: $248 \pm 31\ \mu g\ m^{-2}a^{-1}$, stomatal uptake: $64 \pm 27\ \mu g\ m^{-2}a^{-1}$, and soil evasion: -128 $\pm 8\ \mu g\ m^{-2}a^{-1}$. We derive each of these fluxes below.

At a $1.06 \pm 0.07\ ng\ m^{-3}$ air-mercury concentration, there is on average a zero vertical mercury gradient (see Figure 4-2d), meaning that average evasion equals average loading at that concentration. Applying the observed $0.0098\ m^{-1}$ slope of vertical mercury gradient versus 58-m mercury (see Figure 4-2d), the evasion flux equals the average loading flux from a $0.0109 \pm 0.0007\ ng\ m^{-4}$ gradient. Since the residuals of the gradient-versus-concentration regression were uncorrelated with eddy diffusivities (r=0.06), we calculated the average evasion flux by multiplying this average gradient by the average eddy diffusivity, estimating evasion at $-128 \pm 8\ \mu g\ m^{-2}a^{-1}$ (see section 4.2.4 for the full explanation of this method).

A modified method allowed us to calculate the stomatal uptake flux, assuming the diel variation in this zero-gradient condition was driven by stomata opening only during daytime. We found evasion equaled loading at a daytime concentration ($0.90 \pm 0.10\ ng\ m^{-3}$), which was $0.45 \pm 0.19\ ng\ m^{-3}$ lower than the corresponding nighttime equilibrium air concentration ($1.35 \pm 0.10\ ng\ m^{-3}$) as seen in Figure 4-2e. This difference likely reflects the added stomatal uptake flux during daytime compared with nighttime when stomata are closed; specifically, a higher nighttime concentration is required for dry deposition alone to equal evasion, compared with the lower daytime concentration at which the combined dry deposition and stomatal uptake collectively equal evasion (see section 4.2.4 for method details and assumptions). The difference between net-zero flux concentrations allowed us to estimate a Los Amigos net stomatal uptake flux of $64 \pm 27\ \mu g\ m^{-2}a^{-1}$. Subtracting the stomatal uptake and evasion fluxes from the total flux, we estimated the direct dry deposition flux of gaseous elemental mercury as $248 \pm 31\ \mu g\ m^{-2}a^{-1}$ (see section 4.2.4 for method details).

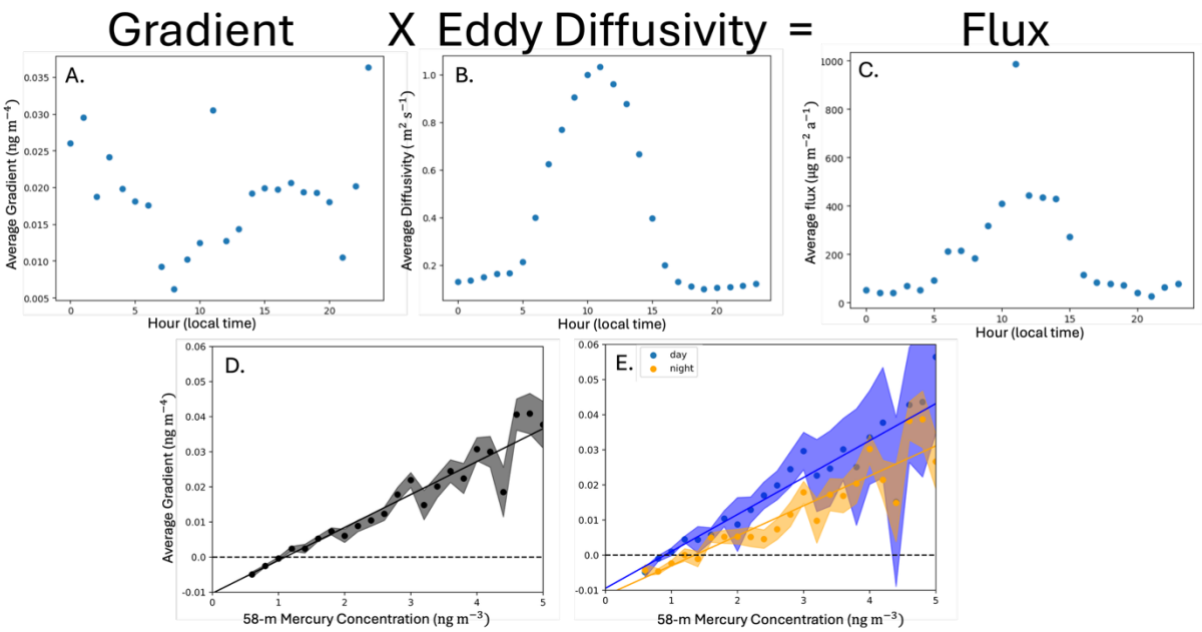

Figure 4-2. This figure shows the air-mercury gradient between 16m and 58m (Panel A), modeled eddy diffusivities (Panel B), and net mercury flux into soils (Panel C), averaged by hour of day from continuous mercury data collected at the Los Amigos Flux tower in June 2024 and September 2024 through January 2025. Panel D and E display the average vertical mercury gradient between 16 and 58 m for different 58-m air-mercury concentrations for all times of day in Panel D and separated by day (blue) and night (orange) in panel E.

This inclusion of dry deposition results in a total loading estimate more than 4-times larger than a prior study's calculation[19] of 71 $\mu g\ m^{-2}a^{-1}$, which accounted only for litterfall at the same study site (we exclude the prior estimate's rainfall and throughfall fluxes, since they move particulate rather than gaseous elemental mercury). Our finding that dry deposition is the leading flux is consistent with a recent study[134] in a deciduous forested site, highlighting that mercury budgeting should include this commonly ignored[135] but leading flux. In section 4.3.2, we consider the stomatal uptake flux in greater detail and compare it to litterfall measurements. Assuming loading scales with air-concentrations (see section 4.2.5), an average 3.0 $ng\ m^{-3}$ 58-m air concentration across continuous mercury measurements implies a stomatal uptake rate of β_{stom}=0.68 $\pm$ 0.29 $mm\ s^{-1}$ and a dry deposition rate of β_{dd}=2.62 $\pm$ 0.32 $mm\ s^{-1}$ (these depositional velocities represent the flux per concentration and have units of length per time).

Using these estimated fluxes, we evaluate whether evasion is in equilibrium with pre-industrial loading, modern loading, or a loading rate between the two. The evasion flux, -128 $\pm$ 8 $\mu g\ m^{-2}a^{-1}$, represents almost half of the total loading flux at a 58-m air concentration of 3.0 $ng\ m^{-3}$. If evasion were to stay constant and deposition scales with air concentrations, then the system would be in equilibrium at a 1.23 $\pm$ 0.04 $ng\ m^{-3}$ air concentration. This suggests that this site's soils are evading in equilibrium with the post-industrial background (Chapter 2 calculated this 58-m background at approximately 1.22 $ng\ m^{-3}$). However, post-industrial loading explains at most 20% of

the site's soil concentrations (previously estimated[136] at approximately $150\ \mathrm{ng\ g^{-1}}$ down to 50 cm). If evasion scaled only with soil concentrations, then pre-industrial evasion would look similar to modern evasion ($128 \pm 8\ \mathrm{\mu g\ m^{-2} a^{-1}}$), which is 3 to 7 times pre-industrial loading (implied by pre-industrial background air estimates[137] of 0.27 CI: [0.18, 0.40] $\mathrm{ng\ m^{-3}}$). Pre-industrial evasion exceeding loading presents an apparent contradiction, since soils should have been in equilibrium over pedogenic timescales. Therefore, we deduce that evasion cannot scale only with soil-mercury concentrations.

Elevated evasion due to photoreduction in the 5-10 m clearing around the tower (see section 4.3.7 for general post-deforestation evasion dynamics) is unlikely to explain the gradient flux evasion estimate, since we did not observe elevated evasion between 10 AM and 2 PM hours when sun was able to directly reach this bare soil—in fact, these hours exhibited the highest downward flux into soils as seen in Figure 4-2. Particulate mercury inputs are unlikely to explain the difference, as prior estimates of these particulate loading at the Los Amigos site[19] are less than 25% of our estimated gaseous elemental mercury flux. Instead, we argue that the data indicates a flaw in the assumption that a site's evasion rate scales only with soil-mercury concentrations. If recently deposited mercury is preferentially emitted, then modern evasion could far exceed pre-industrial evasion despite soil concentrations being similar. In that case, evasion likely scales with some combination of soil concentrations and modern loading rates.

4.3.2. Soil and Air Mercury Co-Determine Leaf Mercury

Prior studies[138–141] in other regions have argued that stomatal uptake of atmospheric mercury drives leaf mercury levels, with minimal translocation from soils to roots to shoots to leaves. Amazon studies[19,113] have assumed this result holds in the Amazon, although soil's negligible role has not been verified in tropical forests. A recent Peruvian Amazon study[113] measured that mass independent fractionation (Δ^{199}) in leaves was depleted compared to air; they hypothesized that this -0.2 ‰ fractionation reflects preferential reemission of odd isotopes during photoreduction[113] (see section 4.2.6 for the definition and calculation method of isotope fractionations). However, this prior study also noted the variability in this proposed mass independent fractionation unexpectedly correlated with a site's air contamination.[113] We propose that a two endmember (air and soil) mixing model offers a simpler explanation that fits leaf isotope data without requiring this unexplained preferential fractionation. We observed a larger difference between air and leaf Δ^{199} at sites where soil has more depleted Δ^{199} than air (see Figure 4-3); this preferential depletion suggests that leaves absorb at least some of their mercury from soils resulting in Δ^{199} fractionations in between the two sources.

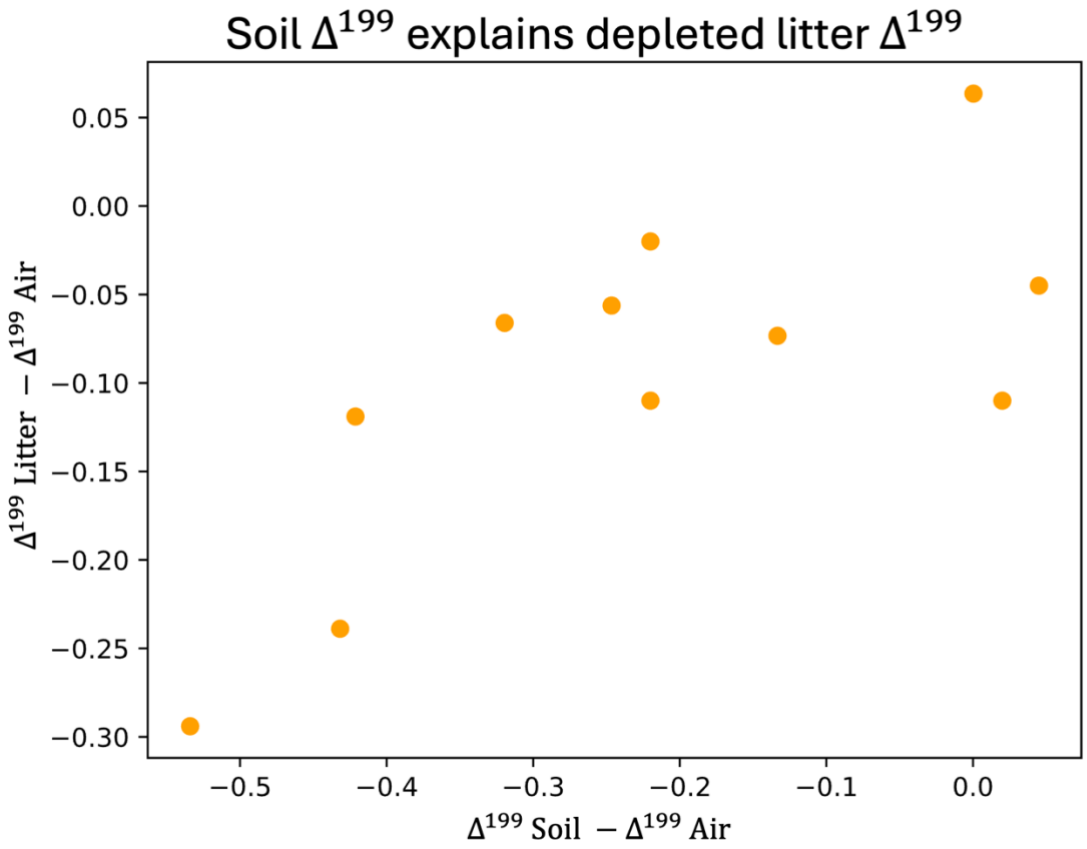

Figure 4-3. This figure plots the difference of Δ^{199} in litter versus soil, normalized by Δ^{199} in air.

This trend is confirmed by a two-endmember soil-and-air mixing model, where we jointly minimize prediction error for total mercury, δ^{202}, and Δ^{199} (see section 4.2.8 for the optimization methodology). This two-endmember model better predicts leaf litter isotope fractionation (δ^{202} and Δ^{199}) than an air-uptake-only model but performs similarly well in predicting total mercury (see Figure 4-4). Our two-endmember model estimated that bulk litter mercury concentrations increase by 45 (CI: [35, 60]) $\mathrm{ng\ g^{-1}}$ per $\mathrm{ng\ m^{-3}}$ of air-mercury exposure (measured at a 1.75-m height) and by 0.46 (CI: [0.25, 0.69]) $\mathrm{ng\ g^{-1}}$ per $\mathrm{ng\ m^{-3}}$ of soil mercury exposure (measured at a 10-15 cm depth which we assume is representative of soil mercury available to root uptake).

This endmember analysis illuminates the presence of soil uptake, which cannot be seen from total mercury levels alone. Without soil uptake, the mass-dependent fractionation (δ^{202}) during net stomatal uptake was modeled at -3.3‰ (CI: [-3.6‰, -3.0‰]), which is consistent with prior research.[15] However, when we included soil uptake—which requires more depletion during stomatal uptake to balance the less depleted δ^{202} entering from soil stores—this estimated mass-dependent fractionation increased to -3.7‰ (CI: [-4.1‰, -3.4‰]). Additionally, we found that previously speculated[113] mass independent fractionation (Δ^{199}) during net stomatal uptake disappears—estimated at -0.04‰ (CI: [-0.10‰, 0.02‰])—when we accounted for soil

uptake (soil Δ^{199} explains the depletion observed in leaves). There was a potential (though not statistically significant) correlation between residual Δ^{199} and pH (r=-0.37); if confirmed in future research, such a correlation could indicate that a high pH increases the bioavailability of soil mercury, thereby increasing the soil-uptake rate (see Figure 4-4c).

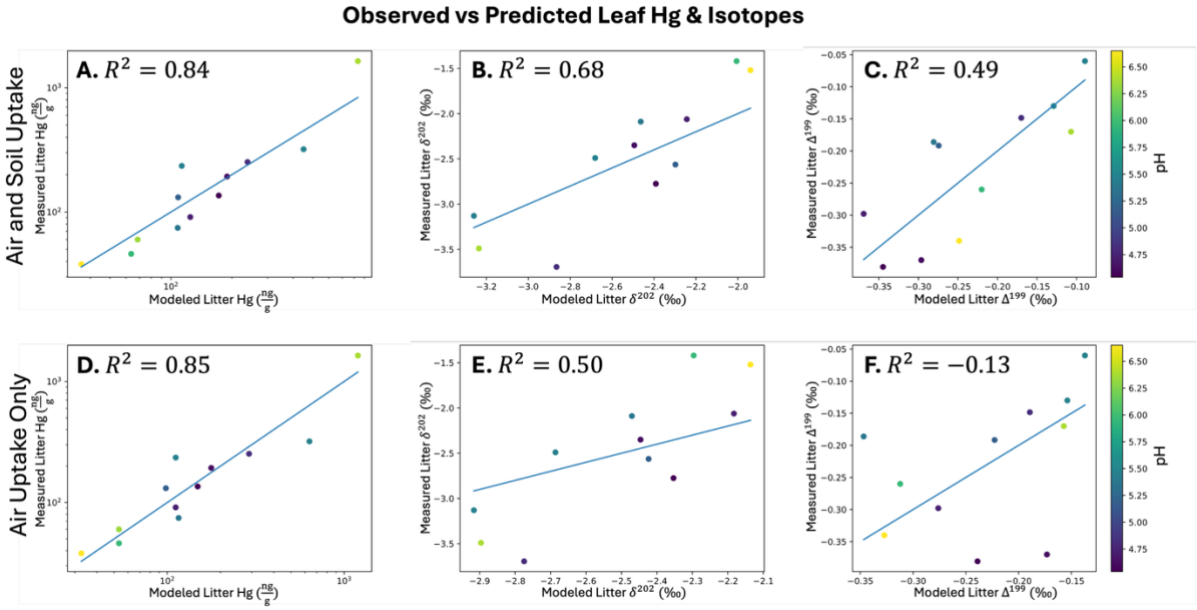

Figure 4-4 displays measured versus predicted total mercury (panels A & D), δ^{202} (panels B & E), and Δ^{199} (panels C & F) for a two endmember model with air and soil uptake into leaves (panels A, B, & C) and a one endmember model with only air uptake (panels D, E, & F). In each panel, we included a pseudo-R^2 representing the fraction of measured variance explained by the two endmember model in the given parameter.

Our mixing model analysis indicates that only a fraction of mercury observed in leaf litter originated from the atmosphere. The soil uptake component carries mercury from soils into leaves, which fall back as litter and either recycle mercury back into soils or evade it into the atmosphere during decomposition.

Applying a 417 g $m^{-2}a^{-1}$ litterfall rate from a prior Amazon study,[142] we estimate, at the Los Amigos tower site, that stomatal uptake of atmospheric mercury contributes a 41 (95%: [32, 55]) μg $m^{-2}a^{-1}$ flux into soils and soil uptake recycles 28 (95%: [15, 42]) μg $m^{-2}a^{-1}$ from soil to leaves and back into soil. The total mercury in litterfall entering soil (including both atmospheric inputs and soil recycling) at the Los Amigos site is 69 (CI: [47, 97]) μg $m^{-2}a^{-1}$, which is consistent with the prior 71 μg $m^{-2}a^{-1}$ estimate,[19] which assumed all litterfall mercury came from atmospheric uptake. However, when we exclude soil recycling this atmospheric loading flux shrinks to 58% (95%: [45%, 77%]) of the prior estimate.[19] Therefore, the prior assumption that litterfall mercury originated from atmospheric inputs has likely led to an overestimation of the actual leaf uptake flux.

Lastly, we find that this section's two-endmember model's litterfall flux estimate at the Los Amigos site of 41 (95%: [32, 55]) μg $m^{-2}a^{-1}$ has overlapping confidence intervals

with section 4.3.1's stomatal-uptake flux estimate of 64 ± 27 $\mu g\ m^{-2} a^{-1}$. The higher point estimate from the gradient flux method is consistent with measurement noise, but it could also reflect a difference in what each method measures. The gradient-flux estimate includes all (net) mercury absorption through stomata, whereas the litterfall analysis only captures what remained in leaves rather than translocating to other parts of plants. If some of the low but non-zero mercury concentrations that prior research has noted in woody tissue[143] arrived via stomatal uptake, then we would expect a slightly larger stomatal uptake flux than what is deduced from leaf litterfall alone.

4.3.3. Quantifying the Regional and Global Fate of Amazon Mercury Emissions

To understand the long-term fate of emitted mercury, we combined ecosystem loading rates with Lagrangian transport modeling to estimate the fraction of Amazon emissions that end up entering Amazon soil pools. On average approximately $39 \pm 4\%$ of mercury emitted uniformly across all pixels is absorbed regionally; weighting pixels by actual 2024 mining emissions does not significantly change this fraction: $43 \pm 4\%$ (see Figure 4-5a). The remaining 61% (57%, respectively) of emissions enter the free troposphere and global circulation before they can sorb locally. The split between Amazon soil deposition and entry into the global mercury cycle suggests that the exposure burden of Amazon emissions is roughly shared between regional ecosystems and the global mercury cycle, but spatial and temporal variability in meteorology determine the exact proportion going to each.

Deep convection events are the only modeled mechanism (see Chapter 2) to mix air from the planetary boundary layer into the free troposphere, effectively resetting concentrations to atmospheric background in the process. Most of the Amazon experiences frequent deep convection events, but they tend to occur more frequently in the central Amazon than the Northeast Amazon and Andean foothills.[144] As a result of differences in this frequency, the fraction of emitted mercury absorbing regionally varies widely from near 0% to 80% depending where in the Amazon it is emitted (see Figure 4-5a).

The fate of emitted mercury also depends on when emissions occur. More frequent convective mixing during the wet season (October-April) drives down the average (horizontally aggregated) ground-level concentration footprint to half that in the dry season (residing for 2.0 and 4.5 minutes, respectively, per vertical meter of air column), as shown in Figure 4-5c. These reduced air concentrations lead to half the ecosystem uptake per emission ($29 \pm 3\%$ and $62 \pm 6\%$, respectively), as shown in Figure 4-5c.

Ground concentrations are even more impacted by the time of day that emissions occur, because the collapsed night-time planetary boundary layer concentrates ground-level mercury plumes for hours before the layer expands in the morning. We

find that nighttime emissions result in five times the (horizontally aggregated) downwind concentration impact as daytime emissions (5.4 and 1 minutes per vertical meter for daytime and nighttime emissions, respectively) as shown in Figure 4-5b. However, dampened night-time vertical mixing results in only a 1.8-fold difference in loading rates ($53 \pm 5\%$ and $29 \pm 3\%$ for nighttime and daytime emissions, respectively) as shown in Figure 4-5b. The diel cycle suggests that interventions promoting daytime over nighttime burning could lead to substantial reductions in both air and ecosystem exposure that threatens ecosystems and communities in the Amazon.

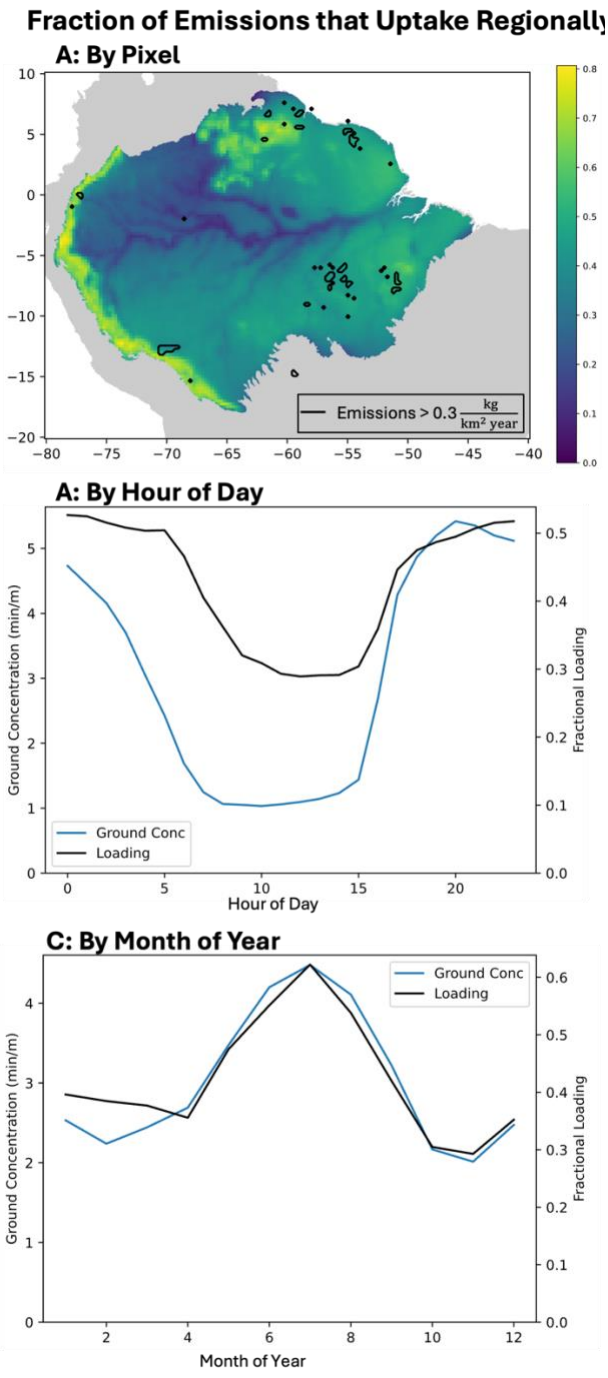

Figure 4-5. ***Air-concentration and soil loading impacts of emissions.*** *Panel A displays the fraction of emitted mercury depositing in Amazon soils, depending in which pixel the emissions occurred; black contours denote* $0.25°$ *grid cells where emissions exceeded, on average,* $0.3\ kg\ km^{-2}\ year^{-1}$*. Panel B and C display fraction of emitted mercury absorbing into Amazon soil stores along with the modeled time (minutes) an average emitted mercury-vapor atom resides in the lowest meter of air (before either absorbing into soils or entering the free troposphere) by the hour of day (panel B) and month of the year (panel C) in which the emission occurred.*

4.3.4. Mercury Loading Explains the Soil-Mercury Enrichment

We translate atmospheric mercury loading from 2001-2025 mining to predict the surficial (0-5 cm) soil mercury enrichment compared with deeper (10-15 cm) soils at forested sites (see Figure 4-6). The model appears to match observed soil gradients at several contaminated sites: La Pampa, Laberinto, and Paulita; additionally, most

minimally impacted sites exhibit a negligible gradient (see Figure 4-6a). However, modeled enrichment at two outlier sites, Boca Colorado and Kilo, was substantially lower than observed surficial enrichment which lowered the model's R^2 from 0.46 (excluding those two sites) to 0.08. At the highly contaminated Boca Colorado site, the air-concentration footprint model (see Chapter 2) underestimates 2018 observed concentrations by a factor of 4.5—a known limitation estimating concentrations near urban centers—explaining the modeled underestimation of the soil gradient. Scaling a site's modeled historical loading by an adjustment factor—observed air mercury divided by modeled air concentrations in the year of measurement—increases model predictive power across all sites from 0.08 to 0.62 (no adjustment was applied for CM2 where air-mercury data is missing) as shown in Figure 4-6b.

The observed negative mercury gradient at the Kilo tower site suggests that some mechanism other than loading is at play. During sampling, we observed the site contained many patches of bamboo, which grows after disturbances such as fire.[145] A single large disturbance or a periodic disturbance history (e.g. fire) could explain the depleted surface mercury compared to deeper soils due to increased rates of evasion associated with deforested soil (see deforestation impacts in section 4.3.7). If the Kilo site is removed from analysis, the corrected (by air-mercury adjustment factor) model predicts soil gradients with an R^2=0.74. It is unsurprising that mining enrichment increases surficial mercury concentrations, but we found that our loading model, which only depends on air-mercury data, was (with corrections applied) able to explain much of the actual observed enrichment.

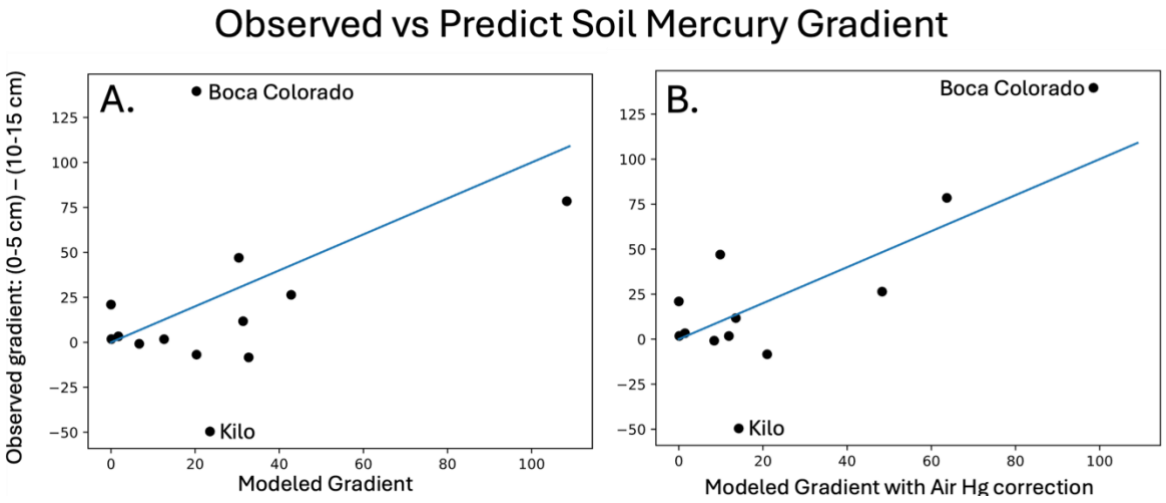

Figure 4-6. This figure compares the observed and modeled soil mercury gradient between 10-15 cm and 0-5 cm depths. The modeled soil mercury gradient is presented as is (panel A) and after correcting by the site's ratio of observed to modeled air-mercury concentration (panel B). The sites of Boca Colorado and Kilo tower were marked to highlight the substantial air-mercury model correction required (for Boca Colorado) and a negative mercury gradient indicating some other process is present (for Kilo).

4.3.5. Topography Explains Baseline Soil Mercury

Section 4.3.4 demonstrated how elevated atmospheric deposition from nearby mining helps us explain the surficial soil mercury enrichment compared with respective deeper soil horizons, where we assumed there was minimal mining enrichment. However, the deeper horizons (10-15 cm) themselves exhibited highly variable soil mercury concentrations between sites. We observe higher baseline (10-15 cm) soil mercury levels (Adjusted R^2=0.79) and depleted Δ^{199} (Adjusted R^2=0.71) at sites at a high elevation relative to the local minimum within a 1-km radius (see Figure 4-7). We find that baseline soil mercury increases by 1.5 ± 0.2 ng g^{-1} per additional meter of relative elevation—defined as how high a pixel is above the lowest pixel within a 1-km radius. Across sampled relative elevations, we estimate that baseline (10-15 cm) soil mercury concentrations vary from 27 ± 9 ng g^{-1} at local low points to 144 ± 9 ng g^{-1} at an 80 m relative elevation. Similarly, we find that Δ^{199} ranges from -0.15‰ at local minima to -0.61‰ at relative high points. For the rest of this subsection, we consider potential explanatory mechanisms that topography could proxy for, producing the observed differences across relative elevations.

We argue that pH, which prior work has associated with soil-mercury stability,[146] is unlikely to mediate the observed correlation with topography. We found that pH explains substantially less variation of 10-15 cm mercury concentrations (adjusted R^2=0.51 for total mercury and adjusted R^2=0.45 for Δ^{199}) than the baseline mercury variation explained by relative elevation (see previous paragraph). Furthermore, pH adds minimal additional explanatory power on top of relative elevation alone with adjusted R^2 increasing from 0.79 to 0.87 for total mercury and 0.71 to 0.73 for Δ^{199} (see Figure SI 6-10). In fact, the observed correlation between pH and baseline mercury is likely to indicate that the pH proxies for relative elevation (r=-0.50) since pH tends to be lower in terra firme than floodplains.[147]

A second potential mediator is soil organic matter, which prior work has positively associated with mercury retention.[146] However, soil organic matter, proxied by loss on ignition, is an even worse predictor than pH of 10-15 cm mercury across the 6 sites we measured with an R^2 = 0.16 (see Figure SI 6-9). Any other hidden variable (or a combination of multiple hidden variables) that mediates the observed relationship between relative elevation and soil mercury would have to be closely associated with both soil-mercury concentrations and topography, with a product of R^2 equaling 0.79. We expect that such highly correlated mediating variables would likely be supported by multiple lines of converging evidence. Based on our data and a synthesis of available literature, converging lines of evidence support erosion as a plausible explanatory mechanism, for at least some of the observed trend (see section 4.3.6).

We hypothesize that high relative elevation sites have longer mercury-residence times in soils (see SI section 6.3.2 for site level residence time estimates) than seen at low

relative elevations. These high elevation sites exhibit an odd-isotope mass-independent fractionation most consistent with photoreduction during the pedogenic timescales of soil formation, although dark abiotic reduction and microbial reduction may also be present (see SI section 6.3.3). The next section considers potential hydrologic processes that could explain the lower concentrations and non-depleted Δ^{199} observed at low relative elevations.

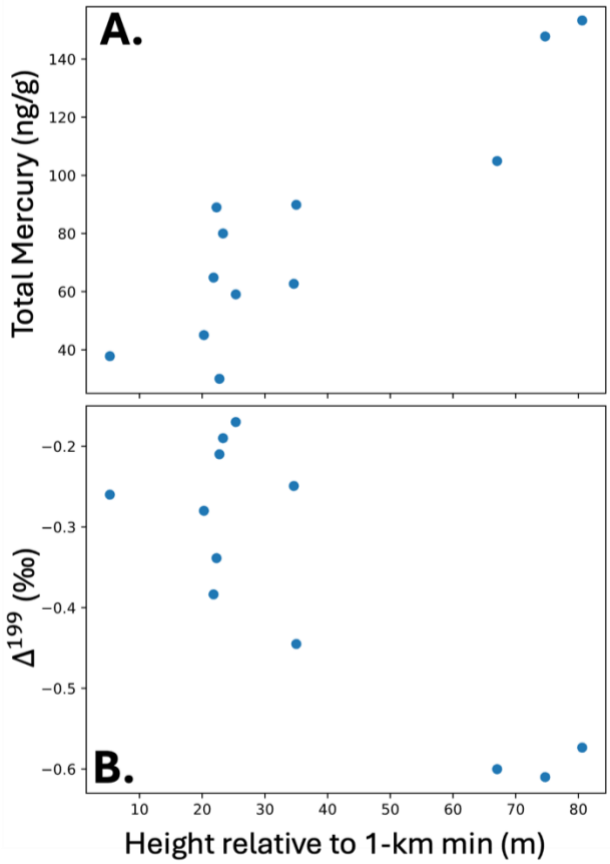

Figure 4-7 plots total mercury (panel A) and Mercury Δ^{199} (panel B) for the baseline (10-15 cm) horizon against the relative elevation above the minimum of all pixels within 1 km.

4.3.6. Eroded Mercury Depletes Soils and Enriches Rivers

In section 4.3.5 we observed that high-elevation sites primarily lose mercury through an evasion pathway inducing Δ^{199} fractionation, but some other pathway is present at low-points that reduces soil-mercury residence times (see SI section 6.3.2) without a Δ^{199} fractionation. This pattern is consistent with erosion at lower relative elevations, where greater overland flows may physically transport entire organic and soil particles. If erosion at low relative elevations outpaces other loss pathways (i.e. evasion), then those low elevations would experience substantially depleted mercury (compared to relative high elevations) and would not experience any Δ^{199} fractionation (compared with atmospheric inputs) since no fractionation occurs during the physical transport of entire particulates. To test this hypothesis, this subsection compares the mercury

erosion flux required to explain "missing" soil mercury at low relative elevations and the mercury erosion flux required to explain river mercury.

The missing soil mercury calculation assumed the observed linear trend of baseline soil mercury with relative elevation (Figure 4-7a) holds across Madre de Dios. We do not have calibration data above a relative elevation of 80 m, but we assume that elevations at and above 80 meters experience negligible erosion meaning that their concentrations will look like 80-meter soils. Under this assumption, we calculated average Madre de Dios 10-15 cm soil-mercury concentration as $96\ \mathrm{ng\ g^{-1}} \pm 9\ \mathrm{ng\ g^{-1}}$, representing a $34 \pm 4\%$ depletion compared to 80-meter relative elevation soils where we assumed no erosion is present. If 10-15 cm total-mercury concentrations reflect the (pre-industrial) equilibrium between loading and evasion, then $34 \pm 4\%$ is also the fraction of atmospheric loading that ultimately needs to leave soils via erosion for erosion to explain the observed baseline impact.

Next, we estimated the river mercury flux utilizing a prior Madre de Dios study[20] that measured wet-season suspended particulate mercury concentrations ranging from $7.0 \pm 1.7\ \mathrm{ng\ L^{-1}}$ in a headwater reach to $21.6 \pm 1.7\ \mathrm{ng\ L^{-1}}$ near Puerto Maldonado, corresponding to mercury concentrations within suspended solids of 13.3 ± 3.3 to $42.0 \pm 4.9\ \mathrm{ng\ g^{-1}}$, respectively (see Table SI 6-3). Andean headwaters tend to exhibit high suspended solid levels but low mercury concentrations within those solids (see SI section 6.3.4); therefore, for simplicity we assume that the observed Puerto Maldonado reach observed river mercury arrives only from Amazon forested pixels (43% of total watershed runoff per ERA5Land[120] data between 2001 and 2025) rather than Andes headwaters (57% of watershed runoff). Given this assumption, Madre de Dios rainforest runoff would have to carry an average of $52.7 \pm 4.1\ \mathrm{ng\ L^{-1}}$ to explain river mercury levels. In the Madre de Dios region (rainforest only), the average runoff rate is 1.3 m per year (based again on ERA5[120]). Multiplying the Madre-de-Dios-rainforest runoff mercury concentration estimate by the annual runoff rate, we estimate an average erosion mercury flux of $68.5 \pm 5.3\ \mathrm{\mu g\ m^{-2}\ a^{-1}}$ in the region. This flux represents $45 \pm 7\%$ of the average 2024 modeled Madre de Dios loading (including both background and mining sources).

The fraction of modern input loading lost to erosion calculated from river mercury concentrations ($45 \pm 7\%$) is consistent with the fraction of pre-industrial loading that the topographic model hypothesizes as "missing" at low relative elevations due to erosion ($34 \pm 4\%$). Furthermore, this missing soil mercury explains most ($76 \pm 15\%$) of the observed river mercury concentrations. For this comparison to make sense, the erosion flux grows with modern loading rates rather than aggregate mineral soil concentrations; this assumption is supported by existing literature on the drivers of river-mercury concentrations (see SI section 6.3.4).

That erosion plays a large role in driving soil mercury levels is further corroborated by a prior Brazilian Amazon study,[18] which found that soil mercury levels were negatively correlated with terrain slope. Low relative elevation and high slope increase erosion through distinct mechanisms offering complementary evidence that erosion is a driver of observed soil mercury variation: relative elevation proxies for higher overland flows during extreme rain events whereas high slope decreases the turbulence required for a particle to be carried downslope. Additionally, the slope finding distinguishes between erosion and leaching: leaching decreases with slope (due to lower water residence times) thereby increasing concentrations (not observed), whereas erosion increases with slope as particles can more easily move down steeper gradients decreasing concentrations (that study's observed trend).

Combined with section 4.3.5, the erosion hypothesis helps us interpret the drivers of observed baseline (10-15 cm) soil-mercury concentrations. In floodplain sites like Laberinto (only 4-5 m above the river 30 m away), frequent inundation during high wet season flows more readily carries away deposited mercury, resulting in a low baseline. Mid-elevations (20-40 m above the 1-kilometer radius minimum) are also depleted compared with higher terra firme (although less so than floodplains), which may be explained by extreme rain events resulting in turbulent overland flows that erode sediment from mid-elevations. Local high points are likely subject to less overland flow (in the absence of upgradient pixels that flow through them), resulting in lower total erosion rates.

4.3.7. Deforestation: A Leading Amazon Mercury Emission Source

Deforestation has also been found to increase evasion due to photo-reduction depleting soil mercury.[148] In this section, we quantify this increase across 3 soil depths, noting substantial increases to evasion, but find that atmospheric loading negligibly changes following deforestation. Specifically, we compared neighboring deforested and forested plots; these plots were within a few hundred meters of each other and generally sat within a few meters of relative elevation, meaning that loading rates and topographic influences were similar across plots. We observe that total mercury concentrations in surficial (0-5 cm) soils decrease by $1.5 \pm 0.3\%$ (adjusted $R^2 = 0.76$) per year since deforestation (see Figure 4-8). Adding an air-loading as an exogenous regression variable (accounting for changes in dry deposition and litterfall) results in an insignificant regression coefficient (-0.03 ± 0.03 mm s^{-1}) while worsening the adjusted R^2 (0.75), suggesting that evasion rather than changing inputs is the primary driver of declining concentrations in deforested plots' surface soils. At 5-10 cm and 10-15 cm depths we observe a $1.2 \pm 0.3\%$ and $0.6 \pm 0.3\%$ loss per year respectively (see Figure SI 6-12), suggesting that some of the impact extends to deeper depths.

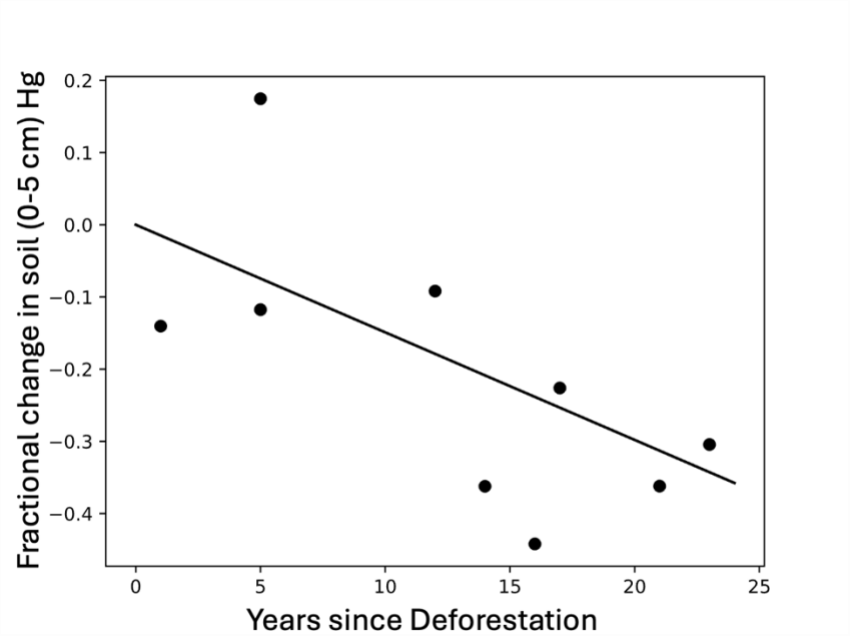

Figure 4-8 shows the fractional loss of surficial (0-5 cm) mercury at deforested versus neighboring forested plots against the estimated number of years since deforestation.

This yearly depletion rate requires a 583 ± 35 $\mu g\ m^{-2} a^{-1}$ evasion rate for deforested plots at the Los Amigos site, almost 5 times the 128 $\mu g\ m^{-2} a^{-1}$ evasion estimate from the site's flux tower—this increase is consistent with past findings[148] that have demonstrated that deforestation can increase mercury evasion by orders of magnitude. Across the 620,000 km^2 of the Amazon deforested since 2000, we modeled an average evasion increase of 130 ± 18 $\mu g\ m^{-2}\ a^{-1}$. This is a smaller evasion difference than at Los Amigos, due to the Amazon's lower average modeled baseline mercury concentration (65 $ng\ g^{-1}$) than at the Los Amigos site.

Our post-deforestation evasion estimate is consistent but on the higher end of a prior Amazon post-deforestation net-emission estimate[149] of 72 [CI: (45, 200)] $\mu g\ m^{-2}\ a^{-1}$. However, unlike this past estimate's 3:1 breakdown of lost biomass uptake to increased evasion, we find that the evasion term explains almost all the observed increase in net emissions. Our breakdown makes sense given that stomatal uptake—which is lost after deforestation—represents only a small fraction of total loading to Amazon forests (see section 4.3.1).

Aggregated across 620,000 km^2 of the Amazon deforestation since 2000, our modeled post-deforestation evasion rate implies a background (excluding mining enrichment) evasion rate of 81 ± 22 $t\ a^{-1}$. If we extend the modeled evasion rate to pre-2000 deforestation beyond where Figure 4-8 was fit—similar to extrapolation conducted in prior post-deforestation emission estimation[149]—we speculate the associated emissions rise by 87 ± 24 $t\ a^{-1}$ to 168 ± 45 $t\ a^{-1}$. Modeled reemission of soil mercury enriched by mining only marginally contributes an additional 1.5 ± 0.4 $t\ a^{-1}$. Forests deforested through fire (a common method of clearing Amazon forests for agriculture

and development) have been found to release an initial pulse of mercury emission during burning,[150] which may increase annual emission rates. Our soil emission estimates from Amazon deforestation are one to two times the 80 tonnes of mercury emissions from Amazon alluvial gold mining (see Chapter 2), with implications for regional mercury emission reduction priorities.

4.3.8. Mapping Surficial Soil-Mercury Concentrations

Combining the estimated topographic baseline, enrichment from loading downwind of mining, and deforestation impacts, we predict surficial mercury levels across forested plots with $R^2 = 0.37$; excluding outliers at Kilo (based on disturbance history) and Boca Colorado (based on inaccurate modeled concentrations) as in section 4.3.4, the predictive power increases to $R^2 = 0.74$ (see Figure 4-9a). The largest source of model error comes in modeling soil gradients where on-the-ground knowledge was necessary to correct for outliers, and R^2 was similarly 0.74 even with outliers excluded.

Using this 0-5 cm soil model, we generated (2026) surficial soil maps across Madre de Dios (see Figure 4-9b). Local air mercury corrections and manual identification of site-specific gradient outliers were necessary to predict soil mercury. Therefore, these predictions should not be interpreted as high-fidelity estimates of soil mercury. Instead, the prediction map indicates areas where mercury is more likely to be elevated and are more likely to be correct as aggregate spatial averages than for each individual pixel. We estimate that mercury enrichment from gold mining enriches soil mercury by at least 100 $\mathrm{ng\ g^{-1}}$ across 560 $\mathrm{km^2}$ of the Madre de Dios region and more than doubles soil mercury in 2200 $\mathrm{km^2}$ of the region's soils.

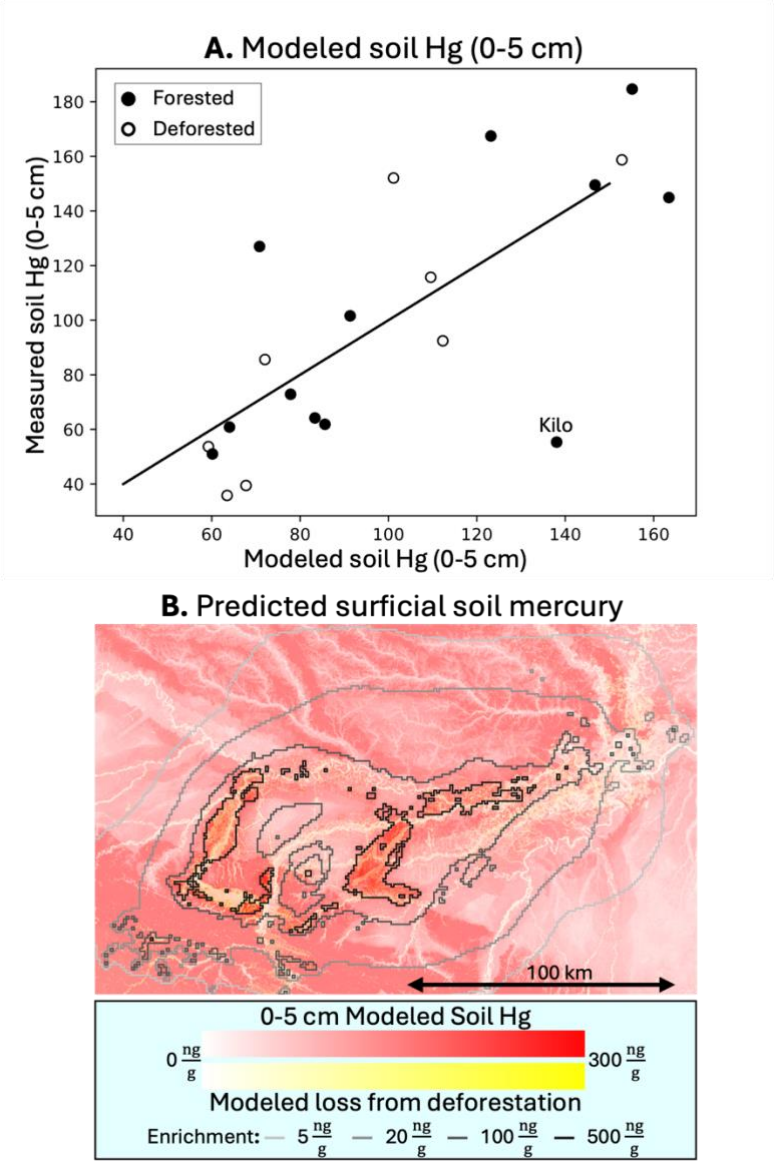

Figure 4-9. Panel A displays measured vs modeled mercury levels at 12 forested (filled points) and 9 deforested plots (unfilled points) in Madre de Dios, Peru. The Kilo site is labeled in Panel A, to highlight the model's poor prediction accuracy at that site, reflecting the site's potential disturbance history (discussed in section 4.3.4). Panel B displays the spatial predictions of surficial (0-5 cm) soil mercury in Madre de Dios, Peru, accounting for mining enrichment (contours), depleted surface mercury due to deforestation (yellow), and the sum of topographic baseline plus enrichment minus deforestation loss (red). Note that red and orange mix to form oranges, indicating that predicted soil mercury and predicted lost surficial soil mercury due to deforestation are on the same order of magnitude.

4.3.9. Broader Implications

The fate of mercury released from Amazon emission sources (e.g. mining) into the atmosphere determines whether emitted mercury's impacts concentrate largely at the regional scale after absorbing into ecosystems or if they distribute globally into the global mercury cycle. This fraction has been contested in scientific literature with some studies measuring substantial increases in regional loading near mining,[18,19] while others have noted negligible differences in sediment cores near mining.[151] Corroborated by on-the-ground air and soil data, we quantified that approximately 40% of Amazon emissions deposits regionally and characterized the spatial and temporal

variation in this fraction. This finding can support modeling efforts that have previously suffered from a 2.6-fold variation in the fraction of mercury emissions for any given Amazon country and bounded this fraction between 3.4% and 22.8% depending on the selected country where emissions occurred.[152] Our results correct a systematic underestimation in this prior modeling due to their exclusion of the direct dry deposition flux pathway, which turns out to be the leading Amazon ecosystem uptake flux.

The long-term fate and transport pathways of Amazon soil mercury carry regional and global consequences. Whether mercury deposited in soils eventually evades into the atmosphere or erodes into rivers has profound implications for regional and global humans and ecosystems. Our erosion estimates indicate that a substantial fraction (approximately 40%) of Amazon forested soil mercury eventually travels into rivers, and approximately 40% of atmospheric emissions reach regional soils. These estimates imply that approximately 16% of atmospheric emissions reach rivers, where it threatens bioaccumulation up the aquatic food chains and into people who consume upper-trophic level fish.[20]

The fate of mercury in deforested regions differs substantially from Amazon forests. Post-deforestation soil evasion appears to introduce an Amazon mercury flux one to two times the emissions from Amazon alluvial gold mining. The fraction of anthropogenic mercury emissions composed by deforestation may be even larger at the global scale, where soil-mercury concentration (30-100 $\mathrm{ng\ g^{-1}}$ range[153]) is not substantially different than the modeled average at Amazon deforested sites (65 $\mathrm{ng\ g^{-1}}$) and where there is less spatial density of gold mining emissions per area. It is plausible that prior underestimation of Amazon post-deforestation evasion could extend to global estimates[149] that relied on only a few global soil emission studies. Furthermore, the past estimate[149] projected extratropical grassland soil-emission rates to extratropical deforested sites, which could lead to a further global downward bias if recently deforested sites may emit substantially more mercury than naturally occurring grasslands—the former may take decades of rapid mercury loss to equilibrate to photodegradation from direct sunlight exposure that grasslands have equilibrated to over millennia. If future research confirms this potential global underestimation of post-deforestation soil-mercury evasion, deforestation could represent the leading global mercury emissions source, which would reframe global mercury budgeting and future policy priorities.

The model's surficial soil mercury predictions may support future research as an input to model soil methylation, terrestrial food chain accumulation, and transport from soils into rivers. These predictions can support environmental, health, and community organizations in identifying on-the-ground locations where levels are likely to be elevated; model predictions can support spatial risk profile analysis, interventions, and further data collection in identified areas of potential risk. This chapter highlights the

far-reaching human and ecosystem implications that can come from combining on-the-ground sampling, novel statistical methods, and regional modeling. At the same time, it illuminates the limitations of extending a model from a small calibration dataset to observed site-level soil enrichment measurements. More global scale data can improve modeling of average behavior (as evidenced by limited global post-deforestation soil-emission data), but local knowledge remains critical to predict soil accumulation and flux pathways at a local scale.

Chapter 5. Conclusion

5.1. Key Findings and Implications

This dissertation tracked Amazon mercury's emission from the site of mining, movement into downwind forests, impact on those forests' productivity, loading into soils, and long-term fate once in soil.

Chapter 2 generated annual high-resolution gold-mining emission and concentration footprint maps across the 21st century. The development of these maps required novel modeling techniques that diverged from established bottom-up gold-activity inventories; this methodology can support future researchers in building inventories from on-the-ground mercury data and remote sensing of mining sites. The model's temporal and spatial consistency enabled interannual comparisons, which have previously been challenging with shifting inventory methods; analyzing these emission time-series highlighted the global drivers of this seemingly regional problem. The model's spatial consistency offers a more accurate spatial attribution of emissions than existing inventories by building the first high-resolution Amazon-scale air-mercury model that tracks exposure in urban mining towns, rural mining regions, and remote forests. These maps offer a tool useful for community organizations and non-profits aiming to reduce mining's harm to nearby people and ecosystems.

Chapter 3 identified a widespread forest-productivity impact from mining's mercury emissions, which was previously only known to occur at high concentrations. The satellite-greenness analysis at low mercury exposures required extensive data cleaning and careful causal identification that was in some cases novel and in other cases borrowed from other fields. Our research suggests the potential for further regional and global downstream impacts that can be speculated, but not conclusively shown, from our data. The regional-to-global scale of impacts reframes mining as a global rather than purely regional issue.

Chapter 4 quantified where mercury goes after it's emitted from gold mines. We found a shared burden between regional loading and direct entry into the global atmospheric cycle, but with temporal and spatial variation that suggests opportunities for simple exposure-mitigation steps miners can implement. We developed spatial maps estimating soil-mercury concentrations, influenced by natural and anthropogenic factors. Whereas these modeled concentration maps may be of greater interest to regional risk mitigation, the implied fate of mercury has regional and global significance. We determined that emissions from deforestation are larger than previously known and rival gold mining emissions as the leading Amazon mercury emission source. On the other hand, substantial erosion from low relative-elevation sites likely drives a substantial fraction of aquatic exposure. Therefore, atmospheric loading into terrestrial Amazon soils appears to be highly connected to the oft-studied

human-exposure pathway of methylation, bioaccumulation up the aquatic food chain, and human consumption of fish. As a result, the same interventions that aim to mitigate direct air exposure are likely to also address both terrestrial and aquatic food chain exposure.

Together, this dissertation tracked where Amazon gold mining emits mercury and how that mercury moves through the atmosphere (Chapter 2), how mercury influences plant physiology and Amazon forest productivity (Chapter 3), and the regional fate of this mercury in Amazon soils and the global atmosphere (Chapter 4). This methodology offers a template for connecting atmospheric pollutants to their regional and global impacts. The results and their framing offer an approach for situating natural science in the complex sociopolitical landscape that is informal gold mining.

5.2. Closing Thoughts: Addressing Gold Mining's Impacts

Gold has been a primary global currency traded historically across much of the world, and it played an important role in facilitating western economic development and driving colonial relations.[154] South America's colonial legacy profoundly affected its economic and institutional development,[155] and ongoing extractive relations continue to feed disparities in economic development.[156]

Ongoing geopolitics reinforce declines in the region's socio-economic well-being and regional sovereignty via western-sponsored coups,[157] conditional humanitarian aid,[158] and Structural Adjustment programs.[159] These outside pressures have been tied to livelihood transitions towards informal gold mining,[160] resulting in widespread socio-environmental harms. Informal gold mining is typically distinguished from larger-scale industrial gold mining operations (which typically do not use mercury), but both are situated within extractive capitalism,[161] jointly reproducing historical colonial relations of gold extracted from the Global South.

However, recognition of gold extraction's ongoing colonial legacy, regional harms, and role within the global economy does not immediately translate to tangible change. Strategies to address the socio-environmental crises resulting from gold mining have often prioritized local interventions in the countries where the mining occurs. Chapter 2 discussed how regulation can limit mining's growth, but once it is entrenched in regional economies, costly (in money and lives) regional enforcement operations and international regulatory efforts (e.g. Minamata) have struggled to reduce the rate of mining. Unfortunately, mining and mercury-use continue to be a reality with no sign of imminent decline. Ample prior evidence of gold mining's harmful effects has not halted its continued expansion, suggesting that researchers must consider more transformative research approaches that support meaningful change.

I propose a few additional directions of research that can fit into theories of change[23]:

1. Exposure mitigation: This type of research goes beyond identifying harms from mining and identifies behaviors that miners, environmental organizations, or community members can modify to reduce emissions or exposure. This research direction accepts that mining and mercury's use may continue for the foreseeable future and generates methods to mitigate harm amidst that reality. Campaigns around mercury-capture technologies[45] have received focus in this vein; however, their substantial attention has not yet transformed the informal gold mining industry. This dissertation research suggests that interventions and educational campaigns targeting the time of day and month of the year that burning occurs could offer a low-cost harm-reduction strategy that miners could more readily employ. Prior research has identified improving urban mining shop ventilation as another potential low-cost, high-impact harm-reduction strategy for both the miners and their immediate neighbors.[13]
2. Alternative livelihoods: Livelihood insecurity pushes people towards gold mining (see Chapter 2 and prior research[64]). Many regional economies have become dependent on mining, potentially feeding cycles of underdevelopment,[112] and degrading the surrounding environment that could otherwise support other industries and livelihoods; however, the path by which mining regions can escape this dependence on gold extraction remains unclear. Efforts to increase the attractiveness and sustainability of other industries and livelihoods may lead people to choose them more frequently over mining. Further research into transition pathways, potentially informed by just transition frameworks from regional economic dependence on fossil-fuel industry jobs,[162] may shed light on regional policies and interventions that support broader development rather than targeting the mining industry directly. An appealing aspect of this approach is its focus on advancing regional well-being—for miners, the community, and the broader environment—rather than criminalizing already vulnerable mining communities.
3. Gold consumption: Global gold-consumption has driven extractive gold mining from the colonial to the modern era, with impacts that extend from the regional to the global scale. Fair gold movements have attempted to track the gold supply chain and support the consumption of mercury-free gold. However, sophisticated supply networks have introduced substantial challenges in conclusively identifying gold's source, and it is contested whether traceable,[163] conflict-free,[164] and fair[165] gold are beneficial frameworks. Therefore, I propose that a broader boycott and divestment (economically and culturally) from all gold is worth consideration—which avoids distinguishing industrial extractive economies as preferable to informal ones. Such a campaign can respond to gold's ongoing colonial history, while also addressing gold's developing geopolitical landscape that includes aiding in the evasion of sanctions[166] and supporting industries of war.[167] As touched on in Chapter 3, gold primarily

serves the amassing of investment wealth rather than broader social or industrial value; furthermore, the fact that its price responds almost entirely to its perceived value rather than some underlying industrial function introduces unique opportunities for boycott and divestment movements. A hypothetical gold divestment movement can be supported by research on systemic-change pathways that consider gold's similarities to and differences from other divestment targets. In the natural science realm, research connecting regional gold production to global drivers and global harms can support advocacy and educational campaigns as a part of a global divestment movement to diminish gold mining's underlying incentive and build a global transition away from this extractive industry.

Combining all these approaches, along with existing regulatory methods, may best position mining communities and global citizens to mitigate harm and build sustainable change at the local, regional, and global scales. Academic research that connects natural science and human-centered disciplines can help identify practical steps towards building each of these approaches. However, research only advances societal change insofar as it supports on-the-ground campaigns that engage with mining communities, global gold buyers, and everyday stewards of our shared world. We intend to share the thesis's high-resolution exposure maps on platforms accessible to Amazon-based community and environmental organizations, while sharing with western communities the local-to-global connections of gold mining's drivers and risks. Doing so requires continually fostering and deepening relationships with partners based in the Amazon and activist networks in Seattle and around the world. At the same time, the research framework of building anticolonial science requires that I critically examine how my developing research program sits within community goals and broader theories of change that will allow me, as a natural scientist, to better position my research in supporting collective social-environmental wellbeing in a more liberated global community.

REFERENCES

(1) Schuster, P. F.; Krabbenhoft, D. P.; Naftz, D. L.; Cecil, L. D.; Olson, M. L.; Dewild, J. F.; Susong, D. D.; Green, J. R.; Abbott, M. L. Atmospheric Mercury Deposition during the Last 270 Years: A Glacial Ice Core Record of Natural and Anthropogenic Sources. *Environ. Sci. Technol.* **2002**, *36* (11), 2303–2310. https://doi.org/10.1021/es0157503.

(2) UNEP. *Global Mercury Assessment 2018*. https://www.amap.no/documents/doc/global-mercury-assessment-2018/1757 (accessed 2025-07-17).

(3) UNSD. UN COMTRADE Database: International Merchandise Trade Statistics. https://comtrade.un.org/.

(4) Ban Toxics! *The Price of Gold: Mercury Use and Current Issues Surrounding Artisanal and Small-Scale Gold Mining in the Philippines*; 2011. http://www.takagifund.org/admin/img/sup/rpt_file20152.pdf (accessed 2025-08-06).

(5) Cordy, P.; Veiga, M.; Crawford, B.; Garcia, O.; Gonzalez, V.; Moraga, D.; Roeser, M.; Wip, D. Characterization, Mapping, and Mitigation of Mercury Vapour Emissions from Artisanal Mining Gold Shops. *Environmental Research* **2013**, *125*, 82–91. https://doi.org/10.1016/j.envres.2012.10.015.

(6) Verbrugge, B.; Besmanos, B. Formalizing Artisanal and Small-Scale Mining: Whither the Workforce? *Resources Policy* **2016**, *47*, 134–141. https://doi.org/10.1016/j.resourpol.2016.01.008.

(7) UNEP, A. *Technical Background Report for the Global Mercury Assessment 2013 | AMAP*. https://www.amap.no/documents/doc/technical-background-report-for-the-global-mercury-assessment-2013/848 (accessed 2025-07-16).

(8) Brienen, R. J. W.; Phillips, O. L.; Feldpausch, T. R.; Gloor, E.; Baker, T. R.; Lloyd, J.; Lopez-Gonzalez, G.; Monteagudo-Mendoza, A.; Malhi, Y.; Lewis, S. L.; Vásquez Martinez, R.; Alexiades, M.; Álvarez Dávila, E.; Alvarez-Loayza, P.; Andrade, A.; Aragão, L. E. O. C.; Araujo-Murakami, A.; Arets, E. J. M. M.; Arroyo, L.; Aymard C., G. A.; Bánki, O. S.; Baraloto, C.; Barroso, J.; Bonal, D.; Boot, R. G. A.; Camargo, J. L. C.; Castilho, C. V.; Chama, V.; Chao, K. J.; Chave, J.; Comiskey, J. A.; Cornejo Valverde, F.; da Costa, L.; de Oliveira, E. A.; Di Fiore, A.; Erwin, T. L.; Fauset, S.; Forsthofer, M.; Galbraith, D. R.; Grahame, E. S.; Groot, N.; Hérault, B.; Higuchi, N.; Honorio Coronado, E. N.; Keeling, H.; Killeen, T. J.; Laurance, W. F.; Laurance, S.; Licona, J.; Magnussen, W. E.; Marimon, B. S.; Marimon-Junior, B. H.; Mendoza, C.; Neill, D. A.; Nogueira, E. M.; Núñez, P.; Pallqui Camacho, N. C.; Parada, A.; Pardo-Molina, G.; Peacock, J.; Peña-Claros, M.; Pickavance, G. C.; Pitman, N. C. A.; Poorter, L.; Prieto, A.; Quesada, C. A.; Ramírez, F.; Ramírez-Angulo, H.; Restrepo, Z.; Roopsind, A.; Rudas, A.; Salomão, R. P.; Schwarz, M.; Silva, N.; Silva-Espejo, J. E.; Silveira, M.; Stropp, J.; Talbot, J.; ter Steege, H.; Teran-Aguilar, J.; Terborgh, J.; Thomas-Caesar, R.; Toledo, M.; Torello-Raventos, M.; Umetsu, R. K.; van der Heijden, G. M. F.; van der Hout, P.; Guimarães Vieira, I. C.; Vieira, S. A.; Vilanova, E.; Vos, V. A.; Zagt, R. J. Long-Term Decline of the Amazon Carbon Sink. *Nature* **2015**, *519* (7543), 344–348. https://doi.org/10.1038/nature14283.

(9) Lapola, D. M.; Pinho, P.; Barlow, J.; Aragão, L. E. O. C.; Berenguer, E.; Carmenta, R.; Liddy, H. M.; Seixas, H.; Silva, C. V. J.; Silva-Junior, C. H. L.; Alencar, A. A. C.;

Anderson, L. O.; Armenteras, D.; Brovkin, V.; Calders, K.; Chambers, J.; Chini, L.; Costa, M. H.; Faria, B. L.; Fearnside, P. M.; Ferreira, J.; Gatti, L.; Gutierrez-Velez, V. H.; Han, Z.; Hibbard, K.; Koven, C.; Lawrence, P.; Pongratz, J.; Portela, B. T. T.; Rounsevell, M.; Ruane, A. C.; Schaldach, R.; Da Silva, S. S.; Von Randow, C.; Walker, W. S. The Drivers and Impacts of Amazon Forest Degradation. *Science* **2023**, *379* (6630), eabp8622. https://doi.org/10.1126/science.abp8622.

(10) Lapola, D. M.; Pinho, P.; Quesada, C. A.; Strassburg, B. B. N.; Rammig, A.; Kruijt, B.; Brown, F.; Ometto, J. P. H. B.; Premebida, A.; Marengo, J. A.; Vergara, W.; Nobre, C. A. Limiting the High Impacts of Amazon Forest Dieback with No-Regrets Science and Policy Action. *Proceedings of the National Academy of Sciences* **2018**, *115* (46), 11671–11679. https://doi.org/10.1073/pnas.1721770115.

(11) Brown, S. T.; Bandoo, L. L.; Agard, S. S.; Thom, S. T.; Gilhuys, T. E.; Mudireddy, G. K.; Eechampati, A. V.; Hasan, K. M.; Loving, D. C.; Seney, C. S.; Kiefer, A. M. A Collaborative Training Program to Assess Mercury Pollution from Gold Shops in Guyana's Artisanal and Small-Scale Gold Mining Sector. *Atmosphere* **2020**, *11* (7), 719. https://doi.org/10.3390/atmos11070719.

(12) Brown, S. T.; Hasan, K. M.; Moody, K. H.; Loving, D. C.; Howe, K. E.; Dawson, A. G.; Drace, K.; Hugdahl, J. D.; Seney, C. S.; Vega, C. M.; Fernandez, L. E.; Kiefer, A. M. Method for Mapping Hg0 Emissions from Gold Shops in Artisanal and Small-Scale Gold Mining Communities. *MethodsX* **2020**, *7*, 101060. https://doi.org/10.1016/j.mex.2020.101060.

(13) Moody, K. H.; Hasan, K. M.; Aljic, S.; Blakeman, V. M.; Hicks, L. P.; Loving, D. C.; Moore, M. E.; Hammett, B. S.; Silva-González, M.; Seney, C. S.; Kiefer, A. M. Mercury Emissions from Peruvian Gold Shops: Potential Ramifications for Minamata Compliance in Artisanal and Small-Scale Gold Mining Communities. *Environmental Research* **2020**, *182*, 109042. https://doi.org/10.1016/j.envres.2019.109042.

(14) Marins, R. V.; Andrade, J. B. de; Pereira, P. A. de P.; Paiva, E. C.; Paraquetti, H. H. M. Sampling Techniques for the Assessment of Anthropogenic Vapour and Particulate Mercury in the Brazilian Amazon Atmosphere. *J. Environ. Monit.* **2000**, *2* (4), 325–328. https://doi.org/10.1039/B000608O.

(15) Szponar, N.; Vega, C. M.; Gerson, J.; McLagan, D. S.; Pillaca, M.; Delgado, S.; Lee, D.; Rahman, N.; Fernandez, L. E.; Bernhardt, E. S.; Kiefer, A. M.; Mitchell, C. P. J.; Wania, F.; Bergquist, B. A. Tracing Atmospheric Mercury from Artisanal and Small-Scale Gold Mining. *Environ Sci Technol* **2025**, *59* (10), 5021–5033. https://doi.org/10.1021/acs.est.4c10521.

(16) Watmough, S.; Osborne, C. Environmental Contamination Associated with Artisanal Gold Mining in Guyana. In *Goldschmidt2025 abstracts*; European Association of Geochemistry: Prague, Czech Republic, 2025. https://doi.org/10.7185/gold2025.29674.

(17) Wip, D.; Warneke, T.; Petersen, A. K.; Notholt, J.; Temme, C.; Kock, H.; Cordy, P. Urban Mercury Pollution in the City of Paramaribo, Suriname. *Air Quality, Atmosphere & Health* **2011**, *6*. https://doi.org/10.1007/s11869-011-0162-3.

(18) Casagrande, G. C. R.; Dambros, J.; de Andrade, E. A.; Martello, F.; Sobral-Souza, T.; Moreno, M. I. C.; Battirola, L. D.; de Andrade, R. L. T. Atmospheric Mercury in Forests: Accumulation Analysis in a Gold Mining Area in the Southern Amazon,

Brazil. *Environ Monit Assess* **2023**, *195* (4), 477. https://doi.org/10.1007/s10661-023-11063-6.
(19) Gerson, J. R.; Szponar, N.; Zambrano, A. A.; Bergquist, B.; Broadbent, E.; Driscoll, C. T.; Erkenswick, G.; Evers, D. C.; Fernandez, L. E.; Hsu-Kim, H.; Inga, G.; Lansdale, K. N.; Marchese, M. J.; Martinez, A.; Moore, C.; Pan, W. K.; Purizaca, R. P.; Sánchez, V.; Silman, M.; Ury, E. A.; Vega, C.; Watsa, M.; Bernhardt, E. S. Amazon Forests Capture High Levels of Atmospheric Mercury Pollution from Artisanal Gold Mining. *Nat Commun* **2022**, *13* (1), 1–10. https://doi.org/10.1038/s41467-022-27997-3.
(20) Diringer, S. E.; Feingold, B. J.; Ortiz, E. J.; Gallis, J. A.; Araújo-Flores, J. M.; Berky, A.; Pan, W. K. Y.; Hsu-Kim, H. River Transport of Mercury from Artisanal and Small-Scale Gold Mining and Risks for Dietary Mercury Exposure in Madre de Dios, Peru. *Environ Sci Process Impacts* **2015**, *17* (2), 478–487. https://doi.org/10.1039/c4em00567h.
(21) Marchese, M. J.; Gerson, J. R.; Berky, A. J.; Driscoll, C.; Fernandez, L. E.; Hsu-Kim, H.; Lansdale, K. N.; Letourneau, E.; Montesdeoca, M.; Pan, W. K.; Robie, E.; Vega, C.; Bernhardt, E. S. Diet Choices Determine Mercury Exposure Risks for People Living in Gold Mining Regions of Peru. *Environ. Res.: Health* **2024**, *2* (3), 035001. https://doi.org/10.1088/2752-5309/ad3d79.
(22) Gonzalez, D. J. X.; Arain, A.; Fernandez, L. E. Mercury Exposure, Risk Factors, and Perceptions among Women of Childbearing Age in an Artisanal Gold Mining Region of the Peruvian Amazon. *Environ Res* **2019**, *179* (Pt A), 108786. https://doi.org/10.1016/j.envres.2019.108786.
(23) Aldous, A. R.; Tear, T.; Fernandez, L. E. The Global Challenge of Reducing Mercury Contamination from Artisanal and Small-Scale Gold Mining (ASGM): Evaluating Solutions Using Generic Theories of Change. *Ecotoxicology* **2024**, *33* (4), 506–517. https://doi.org/10.1007/s10646-024-02741-3.
(24) Guizzardi, D.; Schaaf, E.; Pagani, F.; Banja, M.; Crippa, M.; Becker, W.; Muntean, M.; Simonati, A. EDGAR v8.1 Global Mercury Emissions, 2024. https://doi.org/10.2905/83B507D7-5218-4DC5-95F9-0EC36F073204.
(25) Earth Genome. Earthrise-Media/Mining-Detector, 2021. https://github.com/earthrise-media/mining-detector (accessed 2025-08-04).
(26) McLagan, D. S.; Mitchell, C. P. J.; Huang, H.; Lei, Y. D.; Cole, A. S.; Steffen, A.; Hung, H.; Wania, F. A High-Precision Passive Air Sampler for Gaseous Mercury. *Environ. Sci. Technol. Lett.* **2016**, *3* (1), 24–29. https://doi.org/10.1021/acs.estlett.5b00319.
(27) USGS. *USMIN Mineral Deposit Database | U.S. Geological Survey*. https://www.usgs.gov/centers/gggsc/science/usmin-mineral-deposit-database (accessed 2025-08-05).
(28) Jasansky, S.; Lieber, M.; Giljum, S.; Maus, V. An Open Database on Global Coal and Metal Mine Production. *Sci Data* **2023**, *10* (1), 52. https://doi.org/10.1038/s41597-023-01965-y.
(29) Gorelick, N.; Hancher, M.; Dixon, M.; Ilyushchenko, S.; Thau, D.; Moore, R. Google Earth Engine: Planetary-Scale Geospatial Analysis for Everyone. *Remote Sensing of Environment* **2017**, *202*, 18–27. https://doi.org/10.1016/j.rse.2017.06.031.
(30) Hansen, M. C.; Potapov, P. V.; Moore, R.; Hancher, M.; Turubanova, S. A.; Tyukavina, A.; Thau, D.; Stehman, S. V.; Goetz, S. J.; Loveland, T. R.; Kommareddy,

A.; Egorov, A.; Chini, L.; Justice, C. O.; Townshend, J. R. G. High-Resolution Global Maps of 21st-Century Forest Cover Change. *Science* **2013**, *342* (6160), 850–853. https://doi.org/10.1126/science.1244693.
(31) Isard, W. Location Theory and Trade Theory: Short-Run Analysis. *The Quarterly Journal of Economics* **1954**, *68* (2), 305–320. https://doi.org/10.2307/1884452.
(32) Mellander, C.; Lobo, J.; Stolarick, K.; Matheson, Z. Night-Time Light Data: A Good Proxy Measure for Economic Activity? *PLoS ONE* **2015**, *10* (10), e0139779. https://doi.org/10.1371/journal.pone.0139779.
(33) Carrillo-Tudela, C.; Li, C. A. Trade Blocks and the Gravity Model: Evidence from Latin American Countries. *JEI* **2004**, *19* (4), 667–689. https://doi.org/10.11130/jei.2004.19.4.667.
(34) Elvidge, C. D.; Zhizhin, M.; Ghosh, T.; Hsu, F.-C.; Taneja, J. Annual Time Series of Global VIIRS Nighttime Lights Derived from Monthly Averages: 2012 to 2019. *Remote Sensing* **2021**, *13* (5), 922. https://doi.org/10.3390/rs13050922.
(35) Zhao, C.; Cao, X.; Chen, X.; Cui, X. A Consistent and Corrected Nighttime Light Dataset (CCNL 1992–2013) from DMSP-OLS Data. *Sci Data* **2022**, *9* (1), 424. https://doi.org/10.1038/s41597-022-01540-x.
(36) Cao, C.; Zhang, B.; Xia, F.; Bai, Y. Exploring VIIRS Night Light Long-Term Time Series with CNN/SI for Urban Change Detection and Aerosol Monitoring. *Remote Sensing* **2022**, *14* (13), 3126. https://doi.org/10.3390/rs14133126.
(37) Zhao, M.; Cheng, W.; Zhou, C.; Li, M.; Huang, K.; Wang, N. Assessing Spatiotemporal Characteristics of Urbanization Dynamics in Southeast Asia Using Time Series of DMSP/OLS Nighttime Light Data. *Remote Sensing* **2018**, *10* (1). https://doi.org/10.3390/rs10010047.
(38) Quant, M. I. Measuring Gradients in Gaseous Elemental Mercury Using a Passive Air Sampler. M.Sc., University of Toronto, Canada, 2021. https://www.proquest.com/docview/2557239246/abstract/6127929359DF45B7PQ/1 (accessed 2025-05-06).
(39) Wilks, S. S. The Large-Sample Distribution of the Likelihood Ratio for Testing Composite Hypotheses on JSTOR. *The Annals of Mathematical Statistics* **1938**, *9*, 60–62. https://doi.org/10.1214/aoms/1177732360.
(40) RAISG. *Amazonia Under Pressure 2020*; 2020. https://www.raisg.org/en/publication/amazonia-under-pressure-2020/ (accessed 2026-02-02).
(41) Amaral, S.; Monteiro, A. M. V.; Camara, G.; Quintanilha, J. A. DMSP/OLS Night-time Light Imagery for Urban Population Estimates in the Brazilian Amazon. *International Journal of Remote Sensing* **2006**, *27* (5), 855–870. https://doi.org/10.1080/01431160500181861.
(42) McLagan, D.; Mitchell, C.; Huang, H.; Abdul Hussain, B.; Lei, Y. D.; Wania, F. The Effects of Meteorological Parameters and Diffusive Barrier Reuse on the Sampling Rate of a Passive Air Sampler for Gaseous Mercury. *Atmospheric Measurement Techniques* **2017**, *10*, 3651–3660. https://doi.org/10.5194/amt-10-3651-2017.
(43) Sun, R.; Enrico, M.; Heimbürger-Boavida, L.-E.; Scott, C.; Sonke, J. A Double-Stage Tube Furnace - Acid-Trapping Protocol for the Pre-Concentration of Mercury from Solid Samples for Isotopic Analysis. *Analytical and bioanalytical chemistry* **2013**, *405*, 6771–6781. https://doi.org/10.1007/s00216-013-7152-2.

(44) U.S. EPA. *Method 1631, Revision E: Mercury in Water by Oxidation, Purge and Trap, and Cold Vapor Atomic Fluorescence Spectrometry (EPA-821-R-02-019)*; U.S. Environmental Protection Agency, Office of Water., 2002.
(45) UNEP. *A Practical Guide: Reducing Mercury Use in Artisanal and Small-Scale Gold Mining*; United Nations, 2012.
(46) Chang, J. C.; Hanna, S. R. Air Quality Model Performance Evaluation. *Meteorol Atmos Phys* **2004**, *87* (1), 167–196. https://doi.org/10.1007/s00703-003-0070-7.
(47) Muntean, M.; Janssens-Maenhout, G.; Song, S.; Selin, N. E.; Olivier, J. G. J.; Guizzardi, D.; Maas, R.; Dentener, F. Trend Analysis from 1970 to 2008 and Model Evaluation of EDGARv4 Global Gridded Anthropogenic Mercury Emissions. *Science of The Total Environment* **2014**, *494–495*, 337–350. https://doi.org/10.1016/j.scitotenv.2014.06.014.
(48) Bruno, D. E.; De Simone, F.; Cinnirella, S.; Hedgecock, I. M.; D'Amore, F.; Pirrone, N. Reducing Mercury Emission Uncertainty from Artisanal and Small-Scale Gold Mining Using Bootstrap Confidence Intervals: An Assessment of Emission Reduction Scenarios. *Atmosphere* **2022**, *14* (1), 62. https://doi.org/10.3390/atmos14010062.
(49) Seccatore, J.; Veiga, M.; Origliasso, C.; Marin, T.; De Tomi, G. An Estimation of the Artisanal Small-Scale Production of Gold in the World. *Science of The Total Environment* **2014**, *496*, 662–667. https://doi.org/10.1016/j.scitotenv.2014.05.003.
(50) World Bank. Commodity Price Data, 2026. https://thedocs.worldbank.org/en/doc/74e8be41ceb20fa0da750cda2f6b9e4e-0050012026/world-bank-commodities-price-data-the-pink-sheet.
(51) Espejo, J. C.; Messinger, M.; Román-Dañobeytia, F.; Ascorra, C.; Fernandez, L. E.; Silman, M. Deforestation and Forest Degradation Due to Gold Mining in the Peruvian Amazon: A 34-Year Perspective. *Remote Sensing* **2018**, *10* (12), 1903. https://doi.org/10.3390/rs10121903.
(52) Dethier, E. N.; Silman, M. R.; Fernandez, L. E.; Espejo, J. C.; Alqahtani, S.; Pauca, P.; Lutz, D. A. Operation Mercury: Impacts of National-Level Armed Forces Intervention and Anticorruption Strategy on Artisanal Gold Mining and Water Quality in the Peruvian Amazon. *Conservation Letters* **2023**, *16* (5), e12978. https://doi.org/10.1111/conl.12978.
(53) Swenson, J. J.; Carter, C. E.; Domec, J.-C.; Delgado, C. I. Gold Mining in the Peruvian Amazon: Global Prices, Deforestation, and Mercury Imports. *PLOS ONE* **2011**, *6* (4), e18875. https://doi.org/10.1371/journal.pone.0018875.
(54) Baur, D. G.; Lucey, B. M. Is Gold a Hedge or a Safe Haven? An Analysis of Stocks, Bonds and Gold. *Financial Review* **2010**, *45* (2), 217–229. https://doi.org/10.1111/j.1540-6288.2010.00244.x.
(55) Hergt, B. *Gold Prices during and after the Great Recession*; Volume 2, Number 4; Bureau of Labor Statistics, 2013. https://www.bls.gov/opub/btn/volume-2/pdf/gold-prices-during-and-after-the-great-recession.pdf.
(56) Irawan, W.; Anggita, W.; Yanto, Y.; Zulkarnain, A. A.; Afdal, S. M. The Role of Gold as a Safe-Haven Asset amid Diplomatic Turmoil and The Trump Trade War; Atlantis Press, 2025; pp 155–162. https://doi.org/10.2991/978-94-6463-974-2_23.
(57) Spence, E.; Pakiam, R. Gold Surges to 15-Month High as Attack on Ukraine Boosts Havens. *Bloomberg News*. February 24, 2022.

https://www.advisorperspectives.com/articles/2022/02/24/gold-surges-to-15-month-high-as-attack-on-ukraine-boosts-havens (accessed 2026-02-20).
(58) Jones, M. Global Market Reaction to Two Years of War in Gaza. *Reuters*. October 9, 2025. https://www.reuters.com/world/middle-east/global-market-reaction-two-years-war-gaza-2025-10-09/ (accessed 2026-02-20).
(59) PRESIDÊNCIA DA REPÚBLICA CASA CIVIL. Plano de ação para prevenção e controle do desmatamento na Amazônia legal (PPCDAm) : 3ª Fase (2012-2015) : pelo uso sustentável e conservação da floresta. *PPCDAM 3ª Fase* **2013**.
(60) Gaworecki, M. *Brazil high court Forest Code ruling largely bad for environment, Amazon: NGOs*. Mongabay Conservation news. https://news.mongabay.com/2018/03/brazil-high-court-forest-code-ruling-largely-bad-for-environment-amazon-ngos/ (accessed 2026-06-19).
(61) Azevedo, A. A.; Rajão, R.; Costa, M. A.; Stabile, M. C. C.; Macedo, M. N.; dos Reis, T. N. P.; Alencar, A.; Soares-Filho, B. S.; Pacheco, R. Limits of Brazil's Forest Code as a Means to End Illegal Deforestation. *Proceedings of the National Academy of Sciences* **2017**, *114* (29), 7653–7658. https://doi.org/10.1073/pnas.1604768114.
(62) RAISG. Amazonian Indigenous Territories and Protected Areas. Retrieved from Https://Www.Raisg.Org. https://www.raisg.org.
(63) Costa, F. R. C.; Marengo, J. A.; Albernaz, A. L. M.; Cunha, A. P.; Cuvi, N.; Espinoza, J.-C.; Ferreira, J.; Jimenez-Muñoz, J. C.; Páez, M. B.; Carramaschi De Algão Querido, L.; Schöngart, J. *Policy Brief: Droughts in the Amazon*, 1st ed.; Sustainable Development Solutions Network (SDSN), 2024. https://doi.org/10.55161/LVYB6857.
(64) Bansah, K. J.; Arthur-Holmes, F.; Assan, E. Climate Induced Transformation of Agriculture to Artisanal Mining Economy in Dry Regions. *Journal of Rural Studies* **2023**, *99*, 11–19. https://doi.org/10.1016/j.jrurstud.2023.02.005.
(65) Ribeiro Neto, G. G.; Anderson, L. O.; Barretos, N. J. C.; Abreu, R.; Alves, L.; Dong, B.; Lott, F. C.; Tett, S. F. B. Attributing the 2015/2016 Amazon Basin Drought to Anthropogenic Influence. *Climate Resilience and Sustainability* **2022**, *1* (1), e25. https://doi.org/10.1002/cli2.25.
(66) Giraldo Malca, U. F.; Sabogal Dunin-Borkowski, A.; Facho Bustamante, N.; Mori Reaño, M. J.; Giraldo Armas, J. M. Alluvial Gold Mining, Conflicts, and State Intervention in Peru's Southern Amazonia. *The Extractive Industries and Society* **2023**, *13*, 101219. https://doi.org/10.1016/j.exis.2023.101219.
(67) Flores, M. C. La Pampa: más de 1.500 policías ingresan a zona invadida por mineros ilegales. *El Comercio*. Lima February 19, 2019. https://elcomercio.pe/peru/madre-de-dios/pampa-1-500-policias-ingresan-zona-invadida-mineros-ilegales-noticia-608884-noticia/ (accessed 2026-04-08).
(68) Prescott, G. W.; Baird, M.; Geenen, S.; Nkuba, B.; Phelps, J.; Webb, E. L. Formalizing Artisanal and Small-Scale Gold Mining: A Grand Challenge of the Minamata Convention. *One Earth* **2022**, *5* (3), 242–251. https://doi.org/10.1016/j.oneear.2022.02.005.
(69) Sousa, N. S.; Veiga, M. M. *Final Summary Report — Removal of Barriers to Introduction of Cleaner Artisanal Gold Mining and Extraction Technologies.*; United Nations Industrial Development Organization (UNIDO), Global Mercury Project, Vienna.: Itaituba, State of Pará, Brazil, 2007.

https://archive.iwlearn.net/globalmercuryproject.org/countries/brazil/docs/Brazil%20Final%20report.pdf.
(70) Ali, S. H. Gold Mining and the Golden Rule: A Challenge for Producers and Consumers in Developing Countries. *Journal of Cleaner Production* **2006**, *14* (3), 455–462. https://doi.org/10.1016/j.jclepro.2004.05.009.
(71) Liu, L.; Zhang, X.; Zhao, T. GLC_FCS30D: The First Global 30-m Land-Cover Dynamic Monitoring Product with Fine Classification System from 1985 to 2022, 2023. https://doi.org/10.5281/zenodo.8239305.
(72) Santos, S. L.; De Araujo Moxotó, A. C.; Dutra, J. M. Illegal Gold Mining in the Brazilian Amazon: Environmental Degradation in Yanomami Indigenous Lands, and Regulatory Failures. *Sustainable Development* **2026**, sd.70821. https://doi.org/10.1002/sd.70821.
(73) Ngim, C. H.; Foo, S. C.; Boey, K. W.; Jeyaratnam, J. Chronic Neurobehavioural Effects of Elemental Mercury in Dentists. *Occupational and Environmental Medicine* **1992**, *49* (11), 782–790. https://doi.org/10.1136/oem.49.11.782.
(74) OEHHA. *Draft Technical Support Document for Noncancer Risk Assessment Jul 2008*; text; 2008. https://oehha.ca.gov/air/crnr/draft-technical-support-document-noncancer-risk-assessment-jul-2008 (accessed 2026-02-05).
(75) ATSDR. *Toxicological Profile for Mercury*; Agency for Toxic Substances and Disease Registry (ATSDR) Toxicological Profiles; Agency for Toxic Substances and Disease Registry (US): Atlanta (GA), 2024.
(76) Hull, V.; Liu, J. Ecology and Society: Telecoupling: A New Frontier for Global Sustainability. *Ecology and Society* **2018**, *23* (4). https://doi.org/10.5751/ES-10494-230441.
(77) Gatti, L. V.; Basso, L. S.; Miller, J. B.; Gloor, M.; Gatti Domingues, L.; Cassol, H. L. G.; Tejada, G.; Aragão, L. E. O. C.; Nobre, C.; Peters, W.; Marani, L.; Arai, E.; Sanches, A. H.; Corrêa, S. M.; Anderson, L.; Von Randow, C.; Correia, C. S. C.; Crispim, S. P.; Neves, R. A. L. Amazonia as a Carbon Source Linked to Deforestation and Climate Change. *Nature* **2021**, *595* (7867), 388–393. https://doi.org/10.1038/s41586-021-03629-6.
(78) Lovejoy, T. E.; Nobre, C. Amazon Tipping Point. *Science Advances* **2018**, *4* (2), eaat2340. https://doi.org/10.1126/sciadv.aat2340.
(79) Singh, H.; Kumar, D.; Soni, V. Impact of Mercury on Photosynthetic Performance of Lemna Minor: A Chlorophyll Fluorescence Analysis. *Sci Rep* **2023**, *13* (1), 12181. https://doi.org/10.1038/s41598-023-39297-x.
(80) Rodriguez-Pascual, M. J.; Vega, C.; Andrade, N.; Fernández, L. E.; Cheng, S.-H.; Kjellerup, B.; Torrents, A. "Effects of Mercury Exposure in Three Amazonian Agricultural Plant Species and the Impact on Bacterial Population in Soil." *Environmental Research* **2025**, *285*, 122469. https://doi.org/10.1016/j.envres.2025.122469.
(81) Niu, Z.; Zhang, X.; Wang, S.; Zeng, M.; Wang, Z.; Zhang, Y.; Ci, Z. Field Controlled Experiments on the Physiological Responses of Maize (Zea Mays L.) Leaves to Low-Level Air and Soil Mercury Exposures. *Environ Sci Pollut Res Int* **2014**, *21* (2), 1541–1547. https://doi.org/10.1007/s11356-013-2047-5.
(82) Groenendijk, J.; Swamy, V.; Aliaga, R. A.; Ortiz, V. Cocha Cashu Biological Station Profile. *ECOTROPICA* **2019**. https://doi.org/10.30427/ecotrop201904.

(83) Strasser, R. J.; Tsimilli-Michael, M.; Srivastava, A. Analysis of the Chlorophyll a Fluorescence Transient. In *Chlorophyll a Fluorescence*; Papageorgiou, G. C., Govindjee, Eds.; Govindjee, Series Ed.; Advances in Photosynthesis and Respiration; Springer Netherlands: Dordrecht, 2004; Vol. 19, pp 321–362. https://doi.org/10.1007/978-1-4020-3218-9_12.
(84) Schansker, G.; Tóth, S. Z.; Strasser, R. J. Methylviologen and Dibromothymoquinone Treatments of Pea Leaves Reveal the Role of Photosystem I in the Chl a Fluorescence Rise OJIP. *Biochimica et Biophysica Acta (BBA) - Bioenergetics* **2005**, *1706* (3), 250–261. https://doi.org/10.1016/j.bbabio.2004.11.006.
(85) U.S. EPA. *Method 7473 (SW-846): Mercury in Solids and Solutions by Thermal Decomposition, Amalgamation, and Atomic Absorption Spectrophotometry*; Washington, DC., 1998; p Revision 0.
(86) Badgley, G.; Field, C. B.; Berry, J. A. Canopy Near-Infrared Reflectance and Terrestrial Photosynthesis. *Science Advances* **2017**, *3* (3), e1602244. https://doi.org/10.1126/sciadv.1602244.
(87) Zhang, J.; Xiao, J.; Tong, X.; Zhang, J.; Meng, P.; Li, J.; Liu, P.; Yu, P. NIRv and SIF Better Estimate Phenology than NDVI and EVI: Effects of Spring and Autumn Phenology on Ecosystem Production of Planted Forests. *Agricultural and Forest Meteorology* **2022**, *315*, 108819. https://doi.org/10.1016/j.agrformet.2022.108819.
(88) Vermote, E.; Wolfe, R. MOD09GQ MODIS/Terra Surface Reflectance Daily L2G Global 250m SIN Grid V006, 2015. https://doi.org/10.5067/MODIS/MOD09GQ.006.
(89) Conley, T. G. GMM Estimation with Cross Sectional Dependence. *Journal of Econometrics* **1999**, *92* (1), 1–45. https://doi.org/10.1016/S0304-4076(98)00084-0.
(90) Lipsitch, M.; Tchetgen, E. T.; Cohen, T. Negative Controls: A Tool for Detecting Confounding and Bias in Observational Studies. *Epidemiology* **2010**, *21* (3), 383–388. https://doi.org/10.1097/EDE.0b013e3181d61eeb.
(91) Wang, S.; Zhang, Y.; Ju, W.; Qiu, B.; Zhang, Z. Tracking the Seasonal and Inter-Annual Variations of Global Gross Primary Production during Last Four Decades Using Satellite near-Infrared Reflectance Data. *Science of The Total Environment* **2021**, *755*, 142569. https://doi.org/10.1016/j.scitotenv.2020.142569.
(92) Sonoike, K. Photoinhibition of Photosystem I. *Physiol Plant* **2011**, *142* (1), 56–64. https://doi.org/10.1111/j.1399-3054.2010.01437.x.
(93) Running, S.; Maosheng, Z. MODIS/Terra Net Primary Production Gap-Filled Yearly L4 Global 500m SIN Grid V061, 2021. https://doi.org/10.5067/MODIS/MOD17A3HGF.061.
(94) Bauer, L.; Knapp, N.; Fischer, R. Mapping Amazon Forest Productivity by Fusing GEDI Lidar Waveforms with an Individual-Based Forest Model. *Remote Sensing* **2021**, *13* (22). https://doi.org/10.3390/rs13224540.
(95) Malhi, Y. The Productivity, Metabolism and Carbon Cycle of Tropical Forest Vegetation. *Journal of Ecology* **2012**, *100* (1), 65–75. https://doi.org/10.1111/j.1365-2745.2011.01916.x.
(96) Galbraith, D.; Malhi, Y.; Affum-Baffoe, K.; Castanho, A. D. A.; Doughty, C. E.; Fisher, R. A.; Lewis, S. L.; Peh, K. S.-H.; Phillips, O. L.; Quesada, C. A.; Sonké, B.; Lloyd, J. Residence Times of Woody Biomass in Tropical Forests. *Plant Ecology & Diversity* **2013**, *6* (1), 139–157. https://doi.org/10.1080/17550874.2013.770578.

(97) Spawn, S. A.; Sullivan, C. C.; Lark, T. J.; Gibbs, H. K. Harmonized Global Maps of above and Belowground Biomass Carbon Density in the Year 2010. *Sci Data* **2020**, *7* (1), 112. https://doi.org/10.1038/s41597-020-0444-4.
(98) Fendrich, A.; Feng, Y.; Wigneron, J.-P.; Chave, J.; Araza, A.; Li, Z.; Herold, M.; Ometto, J.; Aragão, L. E. O. C.; Martinez Cano, I.; Zhu, L.; Xu, Y.; Ciais, P. Human Influence on Amazon's Aboveground Carbon Dynamics Intensified over the Last Decade. *Nat Commun* **2025**, *16* (1), 6681. https://doi.org/10.1038/s41467-025-61856-1.
(99) Balachandran, L.; Ahmad, S. A.; Amin, A. M.; Shaharuddin, N. A.; Sobri, M. Z. M.; Azzeme, A. M. Effect of Mercury Exposure on the Growth and Physiological Characteristics of Lowland Tomato (Solanum Lycopersicum). *J Biochem Microbiol Biotechnol* **2024**, *12* (1), 34–43. https://doi.org/10.54987/jobimb.v12i1.959.
(100) Cowan, I.; Farquhar, G. Stomatal Function in Relation to Leaf Metabolism and Environment: Stomatal Function in the Regulation of Gas Exchange. *Symposia of the Society for Experimental Biology* **1977**, *31*, 471–505.
(101) Wong, S. C.; Cowan, I. R.; Farquhar, G. D. Stomatal Conductance Correlates with Photosynthetic Capacity. *Nature* **1979**, *282* (5737), 424–426. https://doi.org/10.1038/282424a0.
(102) Staal, A.; Tuinenburg, O. A.; Bosmans, J. H. C.; Holmgren, M.; van Nes, E. H.; Scheffer, M.; Zemp, D. C.; Dekker, S. C. Forest-Rainfall Cascades Buffer against Drought across the Amazon. *Nature Clim Change* **2018**, *8* (6), 539–543. https://doi.org/10.1038/s41558-018-0177-y.
(103) Wunderling, N.; Sakschewski, B.; Rockström, J.; Flores, B. M.; Hirota, M.; Staal, A. Deforestation-Induced Drying Lowers Amazon Climate Threshold. *Nature* **2026**, *654* (8117), 114–120. https://doi.org/10.1038/s41586-026-10456-0.
(104) Flores, B. M.; Montoya, E.; Sakschewski, B.; Nascimento, N.; Staal, A.; Betts, R. A.; Levis, C.; Lapola, D. M.; Esquível-Muelbert, A.; Jakovac, C.; Nobre, C. A.; Oliveira, R. S.; Borma, L. S.; Nian, D.; Boers, N.; Hecht, S. B.; ter Steege, H.; Arieira, J.; Lucas, I. L.; Berenguer, E.; Marengo, J. A.; Gatti, L. V.; Mattos, C. R. C.; Hirota, M. Critical Transitions in the Amazon Forest System. *Nature* **2024**, *626* (7999), 555–564. https://doi.org/10.1038/s41586-023-06970-0.
(105) Staver, A. C.; Archibald, S.; Levin, S. A. The Global Extent and Determinants of Savanna and Forest as Alternative Biome States. *Science* **2011**, *334* (6053), 230–232. https://doi.org/10.1126/science.1210465.
(106) Rennert, K.; Errickson, F.; Prest, B.; Rennels, L.; Newell, R.; Pizer, B.; Kingdon, C.; Wingenroth, J.; Cooke, R.; Parthum, B.; Smith, D.; Cromar, K.; Diaz, D.; Moore, F.; Müller, U.; Plevin, R.; Raftery, A.; Ševčíková, H.; Sheets, H.; Anthoff, D. Comprehensive Evidence Implies a Higher Social Cost of CO2. *Nature* **2022**, *610*. https://doi.org/10.1038/s41586-022-05224-9.
(107) Velásquez López, P. C. MERCURY IN ARTISANAL AND SMALL SCALE GOLD MINING: IDENTIFYING STRATEGIES TO REDUCE ENVIRONMENTAL CONTAMINATION IN SOUTHERN ECUADOR, The University of British Columbia, 2010. https://www.delvedatabase.org/resources/mercury-balance-in-amalgamation-in-artisanal-and-small-scale-gold-mining-identifying-strategies-for-reducing-environmental-pollution-in-portovelo-zaruma-ecuador (accessed 2026-02-02).

(108) Gasparinnetti, P.; Bakker, L. B.; Queiroz, J. M.; Vilela, T. Economic Valuation of Artisanal Small-Scale Gold Mining Impacts: A Framework for Value Transfer Application. *Resources Policy* **2024**, *88*, 104259. https://doi.org/10.1016/j.resourpol.2023.104259.
(109) World Gold Council. Historical Demand and Supply, 2026. https://www.gold.org/goldhub/data/gold-demand-by-country.
(110) Sjaastad, L. A.; Scacciavillani, F. The Price of Gold and the Exchange Rate. *Journal of International Money and Finance* **1996**, *15* (6), 879–897. https://doi.org/10.1016/S0261-5606(96)00045-9.
(111) Keynes, J. M. *The General Theory of Employment, Interest, and Money*; Macmillan: London, UK, 1936. https://doi.org/10.1007/978-3-319-70344-2.
(112) Auty, R.; Warhurst, A. Sustainable Development in Mineral Exporting Economies. *Resources Policy* **1993**, *19* (1), 14–29. https://doi.org/10.1016/0301-4207(93)90049-S.
(113) Szponar, N. Tracing Atmospheric Sources of Mercury through Passive Air Sampling and Isotope Characterization. Ph.D., University of Toronto, Toronto, Ontario, Canada, 2022.
(114) Driscoll, C. T.; Mason, R. P.; Chan, H. M.; Jacob, D. J.; Pirrone, N. Mercury as a Global Pollutant: Sources, Pathways, and Effects. *Environ. Sci. Technol.* **2013**, *47* (10), 4967–4983. https://doi.org/10.1021/es305071v.
(115) Li, C.; Xu, Z.; Luo, K.; Chen, Z.; Xu, X.; Xu, C.; Qiu, G. Biomagnification and Trophic Transfer of Total Mercury and Methylmercury in a Sub-Tropical Montane Forest Food Web, Southwest China. *Chemosphere* **2021**, *277*, 130371. https://doi.org/10.1016/j.chemosphere.2021.130371.
(116) Araujo, B. F.; Hintelmann, H.; Dimock, B.; De Lima Sobrinho, R.; Bernardes, M. C.; De Almeida, M. G.; Krusche, A. V.; Rangel, T. P.; Thompson, F.; De Rezende, C. E. Mercury Speciation and Hg Stable Isotope Ratios in Sediments from Amazon Floodplain Lakes—Brazil. *Limnology & Oceanography* **2018**, *63* (3), 1134–1145. https://doi.org/10.1002/lno.10758.
(117) Lavoie, R. A.; Jardine, T. D.; Chumchal, M. M.; Kidd, K. A.; Campbell, L. M. Biomagnification of Mercury in Aquatic Food Webs: A Worldwide Meta-Analysis. *Environ. Sci. Technol.* **2013**, *47* (23), 13385–13394. https://doi.org/10.1021/es403103t.
(118) Ashe, K. Elevated Mercury Concentrations in Humans of Madre de Dios, Peru. *PLoS One* **2012**, *7* (3), e33305. https://doi.org/10.1371/journal.pone.0033305.
(119) Jiskra, M.; Wiederhold, J. G.; Skyllberg, U.; Kronberg, R.-M.; Hajdas, I.; Kretzschmar, R. Mercury Deposition and Re-Emission Pathways in Boreal Forest Soils Investigated with Hg Isotope Signatures. *Environ. Sci. Technol.* **2015**, *49* (12), 7188–7196. https://doi.org/10.1021/acs.est.5b00742.
(120) Hersbach, H.; Bell, B.; Berrisford, P.; Hirahara, S.; Horányi, A.; Muñoz-Sabater, J.; Nicolas, J.; Peubey, C.; Radu, R.; Schepers, D.; Simmons, A.; Soci, C.; Abdalla, S.; Abellan, X.; Balsamo, G.; Bechtold, P.; Biavati, G.; Bidlot, J.; Bonavita, M.; De Chiara, G.; Dahlgren, P.; Dee, D.; Diamantakis, M.; Dragani, R.; Flemming, J.; Forbes, R.; Fuentes, M.; Geer, A.; Haimberger, L.; Healy, S.; Hogan, R. J.; Hólm, E.; Janisková, M.; Keeley, S.; Laloyaux, P.; Lopez, P.; Lupu, C.; Radnoti, G.; de Rosnay, P.; Rozum, I.; Vamborg, F.; Villaume, S.; Thépaut, J.-N. The ERA5 Global

Reanalysis. *Quarterly Journal of the Royal Meteorological Society* **2020**, *146* (730), 1999–2049. https://doi.org/10.1002/qj.3803.
(121) Desjardins, R. L.; Lemon, E. R. Limitations of an Eddy-Correlation Technique for the Determination of the Carbon Dioxide and Sensible Heat Fluxes. *Boundary-Layer Meteorol* **1974**, *5* (4), 475–488. https://doi.org/10.1007/BF00123493.
(122) Maier, M.; Schack-Kirchner, H. Using the Gradient Method to Determine Soil Gas Flux: A Review. *Agricultural and Forest Meteorology* **2014**, *192–193*, 78–95. https://doi.org/10.1016/j.agrformet.2014.03.006.
(123) Reynolds, O. On the Extent and Action of the Heating Surface of Steam Boilers. *International Journal of Heat and Mass Transfer* **1961**, *3* (2), 163–166. https://doi.org/10.1016/0017-9310(61)90087-4.
(124) Monin, A. S.; Obhukov, A. M. Basic Laws of Turbulent Mixing in the Surface Layer of the Atmosphere. *Contrib. Geophys. Inst. Acad. Sci. USSR* **1954**, *24*, 163–187.
(125) *An Introduction to Boundary Layer Meteorology*; Stull, R. B., Ed.; Springer Netherlands: Dordrecht, 1988. https://doi.org/10.1007/978-94-009-3027-8.
(126) Dyer, A. J. A Review of Flux-Profile Relationships. *Boundary-Layer Meteorol* **1974**, *7* (3), 363–372. https://doi.org/10.1007/BF00240838.
(127) Newey, W. K.; West, K. D. A Simple, Positive Semi-Definite, Heteroskedasticity and Autocorrelation Consistent Covariance Matrix. *Econometrica* **1987**, *55* (3), 703. https://doi.org/10.2307/1913610.
(128) Laacouri, A.; Nater, E. A.; Kolka, R. K. Distribution and Uptake Dynamics of Mercury in Leaves of Common Deciduous Tree Species in Minnesota, U.S.A. *Environ Sci Technol* **2013**, *47* (18), 10462–10470. https://doi.org/10.1021/es401357z.
(129) Janssen, S. E.; Lepak, R. F.; Tate, M. T.; Ogorek, J. M.; DeWild, J. F.; Babiarz, C. L.; Hurley, J. P.; Krabbenhoft, D. P. Rapid Pre-Concentration of Mercury in Solids and Water for Isotopic Analysis. *Analytica Chimica Acta* **2019**, *1054*, 95–103. https://doi.org/10.1016/j.aca.2018.12.026.
(130) Hoogsteen, M. J. J.; Lantinga, E. A.; Bakker, E. J.; Groot, J. C. J.; Tittonell, P. A. Estimating Soil Organic Carbon through Loss on Ignition: Effects of Ignition Conditions and Structural Water Loss. *European Journal of Soil Science* **2015**, *66* (2), 320–328. https://doi.org/10.1111/ejss.12224.
(131) Batjes, N. H.; Dijkshoorn, J. A. Carbon and Nitrogen Stocks in the Soils of the Amazon Region. *Geoderma* **1999**, *89* (3), 273–286. https://doi.org/10.1016/S0016-7061(98)00086-X.
(132) Salazar, R.; Alegre, J.; Pizarro, D.; Duff, A. J.; García, C.; Gómez, C. Soil Carbon Stock Potential in Pastoral and Silvopastoral Systems in the Peruvian Amazon. *Agroforest Syst* **2024**, *98* (7), 2157–2167. https://doi.org/10.1007/s10457-024-00969-w.
(133) European Space Agency; Airbus. Copernicus DEM, 2022. https://doi.org/10.5270/ESA-c5d3d65.
(134) Obrist, D.; Roy, E. M.; Harrison, J. L.; Kwong, C. F.; Munger, J. W.; Moosmüller, H.; Romero, C. D.; Sun, S.; Zhou, J.; Commane, R. Previously Unaccounted Atmospheric Mercury Deposition in a Midlatitude Deciduous Forest. *Proceedings of the National Academy of Sciences* **2021**, *118* (29), e2105477118. https://doi.org/10.1073/pnas.2105477118.

(135) Wright, L. P.; Zhang, L.; Marsik, F. J. Overview of Mercury Dry Deposition, Litterfall, and Throughfall Studies. *Atmospheric Chemistry and Physics* **2016**, *16* (21), 13399–13416. https://doi.org/10.5194/acp-16-13399-2016.
(136) Gerson, J. R.; Szponar, N.; Agostini, A.; Alotaibi, R.; Bergquist, B.; Chen, A.; Fernandez, L. E.; Lansdale, K. N.; Lee, A. H.; Machicao, M. F.; Marchese, M. J.; Topp, S. N.; Vega, C.; Bernhardt, E. S. Chemistry of Surface Water, Precipitation, Throughfall, Leaves, Sediment, Soil, and Air near a Gold Mining Region in Peru. *Ecology* **2022**, *103* (5), e3666. https://doi.org/10.1002/ecy.3666.
(137) Enrico, M.; Le Roux, G.; Heimbürger, L.-E.; Van Beek, P.; Souhaut, M.; Chmeleff, J.; Sonke, J. E. Holocene Atmospheric Mercury Levels Reconstructed from Peat Bog Mercury Stable Isotopes. *Environ. Sci. Technol.* **2017**, *51* (11), 5899–5906. https://doi.org/10.1021/acs.est.6b05804.
(138) Bishop, K. H.; Lee, Y.-H.; Munthe, J.; Dambrine, E. Xylem Sap as a Pathway for Total Mercury and Methylmercury Transport from Soils to Tree Canopy in the Boreal Forest. *Biogeochemistry* **1998**, *40* (2), 101–113. https://doi.org/10.1023/A:1005983932240.
(139) Greger, M.; Wang, Y.; Neuschütz, C. Absence of Hg Transpiration by Shoot after Hg Uptake by Roots of Six Terrestrial Plant Species. *Environmental Pollution* **2005**, *134* (2), 201–208. https://doi.org/10.1016/j.envpol.2004.08.007.
(140) Cui, L.; Feng, X.; Lin, C.-J.; Wang, X.; Meng, B.; Wang, X.; Wang, H. Accumulation and Translocation of 198Hg in Four Crop Species. *Environmental Toxicology and Chemistry* **2013**, *33* (2), 334–340. https://doi.org/10.1002/etc.2443.
(141) Beauford, W.; Barber, J.; Barringer, A. R. Uptake and Distribution of Mercury within Higher Plants. *Physiologia Plantarum* **1977**, *39* (4), 261–265. https://doi.org/10.1111/j.1399-3054.1977.tb01880.x.
(142) Nebel, G.; Dragsted, J.; Vega, A. S. Litter Fall, Biomass and Net Primary Production in Flood Plain Forests in the Peruvian Amazon. *Forest Ecology and Management* **2001**, *150* (1), 93–102. https://doi.org/10.1016/S0378-1127(00)00683-6.
(143) Gerson, J.; Lehnherr, I.; Luu, T.; Bergquist, B.; Szponar, N.; Fernandez, L. E.; Vega, C.; Porter, T. J. Ficus Insipida Tree Rings as Biomonitors for Gaseous Elemental Mercury in the Artisanal Gold Mining-Impacted Peruvian Amazon. *Front. Environ. Sci.* **2025**, *13*, 1531800. https://doi.org/10.3389/fenvs.2025.1531800.
(144) Feng, Y.; Negrón-Juárez, R. I.; Romps, D. M.; Chambers, J. Q. Amazon Windthrow Disturbances Are Likely to Increase with Storm Frequency under Global Warming. *Nat Commun* **2023**, *14* (1), 101. https://doi.org/10.1038/s41467-022-35570-1.
(145) Smith, M.; Nelson, B. W. Fire Favours Expansion of Bamboo-Dominated Forests in the South-West Amazon. *J. Trop. Ecol.* **2011**, *27* (1), 59–64. https://doi.org/10.1017/S026646741000057X.
(146) Yang, Y.; Zhang, C.; Shi, X.; Lin, T.; Wang, D. Effect of Organic Matter and pH on Mercury Release from Soils. *Journal of Environmental Sciences* **2007**, *19* (11), 1349–1354. https://doi.org/10.1016/S1001-0742(07)60220-4.
(147) Avner, B. D. S. G.; Diego, P. B.; Iolanda, M. S. R.; Rodrigo, D. S. Chemical and Textural Properties of Floodplain Forest Soils in the Eastern Amazon, Brazil. *Afr. J. Agric. Res.* **2023**, *19* (1), 91–100. https://doi.org/10.5897/AJAR2022.16242.

(148) Magarelli, G.; Fostier, A. H. Influence of Deforestation on the Mercury Air/Soil Exchange in the Negro River Basin, Amazon. *Atmospheric Environment* **2005**, *39* (39), 7518–7528. https://doi.org/10.1016/j.atmosenv.2005.07.067.
(149) Feinberg, A.; Jiskra, M.; Borrelli, P.; Biswakarma, J.; Selin, N. E. Deforestation as an Anthropogenic Driver of Mercury Pollution. *Environ. Sci. Technol.* **2024**. https://doi.org/10.1021/acs.est.3c07851.
(150) Melendez-Perez, J. J.; Fostier, A. H.; Carvalho, J. A.; Windmöller, C. C.; Santos, J. C.; Carpi, A. Soil and Biomass Mercury Emissions during a Prescribed Fire in the Amazonian Rain Forest. *Atmospheric Environment* **2014**, *96*, 415–422. https://doi.org/10.1016/j.atmosenv.2014.06.032.
(151) Beal, S. A.; Jackson, B. P.; Kelly, M. A.; Stroup, J. S.; Landis, J. D. Effects of Historical and Modern Mining on Mercury Deposition in Southeastern Peru. *Environ. Sci. Technol.* **2013**, *47* (22), 12715–12720. https://doi.org/10.1021/es402317x.
(152) Hedgecock, I. M.; De Simone, F.; Carbone, F.; Pirrone, N. Modelling the Fate of Mercury Emissions from Artisanal and Small Scale Gold Mining. April 3, 2024. https://doi.org/10.5194/egusphere-2024-861.
(153) Gworek, B.; Dmuchowski, W.; Baczewska-Dąbrowska, A. H. Mercury in the Terrestrial Environment: A Review. *Environ Sci Eur* **2020**, *32* (1), 128. https://doi.org/10.1186/s12302-020-00401-x.
(154) Bakewell, P. Mining in Colonial Spanish America. In *The Cambridge History of Latin America: Volume 2: Colonial Latin America*; Bethell, L., Ed.; The Cambridge History of Latin America; Cambridge University Press: Cambridge, 1984; Vol. 2, pp 105–152. https://doi.org/10.1017/CHOL9780521245166.005.
(155) Naritomi, J.; Soares, R. R.; Assunção, J. J. Institutional Development and Colonial Heritage within Brazil. *The Journal of Economic History* **2012**, *72* (2), 393–422.
(156) Acemoglu, D.; Johnson, S.; Robinson, J. A. The Colonial Origins of Comparative Development: An Empirical Investigation. *American Economic Review* **2001**, *91* (5), 1369–1401. https://doi.org/10.1257/aer.91.5.1369.
(157) Absher, S.; Grier, R.; Grier, K. The Consequences of CIA-Sponsored Regime Change in Latin America. *European Journal of Political Economy* **2023**, *80*, 102452. https://doi.org/10.1016/j.ejpoleco.2023.102452.
(158) Ramachandran, S.; UNU-WIDER. *From Empire to Aid: Analysing Persistence of Colonial Legacies in Foreign Aid to Africa*; WIDER Working Paper; WIDER Working Paper 2024; UNU-WIDER, 2024; Vol. 2024. https://doi.org/10.35188/UNU-WIDER/2024/509-7.
(159) Laurell, A. C. Structural Adjustment and the Globalization of Social Policy in Latin America. *International Sociology* **2000**, *15* (2), 306–325. https://doi.org/10.1177/0268580900015002010.
(160) Hilson, G.; Potter, C. Structural Adjustment and Subsistence Industry: Artisanal Gold Mining in Ghana. *Development and Change* **2005**, *36* (1), 103–131. https://doi.org/10.1111/j.0012-155X.2005.00404.x.
(161) Côte, M. Furious Depletion—Conceptualizing Artisan Mining and Extractivism through Gender, Race, and Environment. *Front. Hum. Dyn.* **2023**, *5*. https://doi.org/10.3389/fhumd.2023.1097195.

(162) Wibeck, V.; Jaku, A.; Lee, S.; Linnér, B. The Widening Scope of Just Transitions Research: A Review of an Emblematic Concept. *Env Pol Gov* **2026**, *36* (1), 181–193. https://doi.org/10.1002/eet.70040.
(163) Villanueva Ubillús, A.; Vila Benites, G. Performing Traceability: Unpacking the Artisanal and Small-Scale Gold Mining (ASGM) Trade Circuit in Peru. *Journal of Rural Studies* **2023**, *102*, 103088. https://doi.org/10.1016/j.jrurstud.2023.103088.
(164) Chang, S.; Christensen, H. B. Nothing Gold Can Stay: Artisanal Mine Certifications and Conflict Dynamics in the Congo. *SSRN Journal* **2023**. https://doi.org/10.2139/ssrn.4609332.
(165) Hilson, G. 'Fair Trade Gold': Antecedents, Prospects and Challenges. *Geoforum* **2008**, *39* (1), 386–400. https://doi.org/10.1016/j.geoforum.2007.09.003.
(166) Donovan, K.; Nikoladze, M. *Gold's geopolitical comeback: How physical and digital gold can be used to evade US sanctions*. Atlantic Council. https://www.atlanticcouncil.org/blogs/new-atlanticist/golds-geopolitical-comeback-how-physical-and-digital-gold-can-be-used-to-evade-us-sanctions/ (accessed 2026-07-27).
(167) Berlin, J.; Clement, D.; Elufisan, L.; Hicks, E.; Kész, Z. *The Blood Gold Report: How the Kremlin Is Using Wagner to Launder Billions in African Gold*; 21 Democracy: Washington DC, 2023. https://bloodgoldreport.com/ (accessed 2026-07-27).
(168) Gerken, T.; Chamecki, M.; Fuentes, J. D. Air-Parcel Residence Times Within Forest Canopies. *Boundary-Layer Meteorol* **2017**, *165* (1), 29–54. https://doi.org/10.1007/s10546-017-0269-7.
(169) Venkatram, A. An Examination of the Pasquill-Gifford-Turner Dispersion Scheme. *Atmospheric Environment* **1996**, *30* (8), 1283–1290. https://doi.org/10.1016/1352-2310(95)00367-3.
(170) ECMWF. *ERA5: How to calculate Obukhov Length*. ECMWF Confluence Wiki. https://confluence.ecmwf.int/display/CKB/ERA5%3A+How+to+calculate+Obukhov+Length (accessed 2026-03-13).
(171) Schmitt, A. U.; Ament, F.; de Araújo, A. C.; Sá, M.; Teixeira, P. Modeling Atmosphere–Land Interactions at a Rainforest Site – a Case Study Using Amazon Tall Tower Observatory (ATTO) Measurements and Reanalysis Data. *Atmospheric Chemistry and Physics* **2023**, *23* (16), 9323–9346. https://doi.org/10.5194/acp-23-9323-2023.
(172) Bardakov, R.; Krejci, R.; Riipinen, I.; Ekman, A. M. L. The Role of Convective Up- and Downdrafts in the Transport of Trace Gases in the Amazon. *Journal of Geophysical Research: Atmospheres* **2022**, *127* (18), e2022JD037265. https://doi.org/10.1029/2022JD037265.
(173) Wanzeler, R. T. S.; Mota, M. A. S.; Nogueira, D. S. Variability of Rainfall and Convective Available Potential Energy (CAPE) in Eastern Amazon During Chuva Project. *Anuário IGEO UFRJ* **2018**, *41* (2), 305–317. https://doi.org/10.11137/2018_2_305_317.
(174) Dias-Júnior, C. Q.; Carneiro, R. G.; Fisch, G.; D'Oliveira, F. A. F.; Sörgel, M.; Botía, S.; Machado, L. A. T.; Wolff, S.; Santos, R. M. N. dos; Pöhlker, C. Intercomparison of Planetary Boundary Layer Heights Using Remote Sensing Retrievals and ERA5 Reanalysis over Central Amazonia. *Remote Sensing* **2022**, *14* (18). https://doi.org/10.3390/rs14184561.

(175) Martin, S. T.; Artaxo, P.; Machado, L. a. T.; Manzi, A. O.; Souza, R. a. F.; Schumacher, C.; Wang, J.; Andreae, M. O.; Barbosa, H. M. J.; Fan, J.; Fisch, G.; Goldstein, A. H.; Guenther, A.; Jimenez, J. L.; Pöschl, U.; Silva Dias, M. A.; Smith, J. N.; Wendisch, M. Introduction: Observations and Modeling of the Green Ocean Amazon (GoAmazon2014/5). *Atmospheric Chemistry and Physics* **2016**, *16* (8), 4785–4797. https://doi.org/10.5194/acp-16-4785-2016.

(176) Pekel, J.-F.; Cottam, A.; Gorelick, N.; Belward, A. S. High-Resolution Mapping of Global Surface Water and Its Long-Term Changes. *Nature* **2016**, *540* (7633), 418–422. https://doi.org/10.1038/nature20584.

(177) Meaza, H.; Ali, M.; Tesfamariam, Z.; Abebe, N. Impacts of Artisanal Gold Mining Systems on Soil and Woody Vegetation in the Semi-Arid Environment of Northern Ethiopia. *Singapore Journal of Tropical Geography* **2017**, *38* (3), 386–401. https://doi.org/10.1111/sjtg.12203.

(178) Belmaker, G. *A third of Peru's La Pampa forest cleared for illegal mining ponds, study finds*. Conservation news. https://news.mongabay.com/2020/04/a-third-of-perus-la-pampa-forest-cleared-for-illegal-mining-ponds-study-finds/ (accessed 2026-06-13).

(179) Peres, A. E. C.; Chaves, A. P.; Lins, F. A. F.; Torem, M. L. Beneficiamento de minérios de ouro. *Extração de ouro: princípios, tecnologia e meio ambiente* **2002**.

(180) Bezerra, O.; Veríssimo, A.; Uhl, C. The Regional Impacts of Small-scale Gold Mining in Amazonia. *Natural Resources Forum* **1996**, *20*, 305–317. https://doi.org/10.1111/j.1477-8947.1996.tb00663.x.

(181) Okamoto, H.; Massalski, T. B. The Au-Hg (Gold-Mercury) System. *Bulletin of Alloy Phase Diagrams* **1989**, *10* (1), 50–58. https://doi.org/10.1007/BF02882176.

(182) Veiga, M. M.; Nunes, D.; Klein, B.; Shandro, J. A.; Velasquez, P. C.; Sousa, R. N. Mill Leaching: A Viable Substitute for Mercury Amalgamation in the Artisanal Gold Mining Sector? *Journal of Cleaner Production* **2009**, *17* (15), 1373–1381. https://doi.org/10.1016/j.jclepro.2009.03.012.

(183) Silva, F. D. F.; Perrin, R. K.; Fulginiti, L. E. The Opportunity Cost of Preserving the Brazilian Amazon Forest. *Agricultural Economics* **2019**, *50* (2), 219–227. https://doi.org/10.1111/agec.12478.

(184) WinklerPrins, A.; Oliveira, P. Urban Agriculture in Santarém, Pará, Brazil: Diversity and Circulation of Cultivated Plants in Urban Homegardens. *Boletim do Museu Paraense Emílio Goeldi : Ciências Humanas* **2010**, *5*. https://doi.org/10.1590/S1981-81222010000300002.

(185) Holmes, C. D.; Jacob, D. J.; Yang, X. Global Lifetime of Elemental Mercury against Oxidation by Atomic Bromine in the Free Troposphere. *Geophysical Research Letters* **2006**, *33* (20). https://doi.org/10.1029/2006GL027176.

(186) Selin, N. E.; Jacob, D. J.; Park, R. J.; Yantosca, R. M.; Strode, S.; Jaeglé, L.; Jaffe, D. Chemical Cycling and Deposition of Atmospheric Mercury: Global Constraints from Observations. *Journal of Geophysical Research: Atmospheres* **2007**, *112* (D2). https://doi.org/10.1029/2006JD007450.

(187) Beer, C.; Reichstein, M.; Tomelleri, E.; Ciais, P.; Jung, M.; Carvalhais, N.; Rödenbeck, C.; Arain, M. A.; Baldocchi, D.; Bonan, G. B.; Bondeau, A.; Cescatti, A.; Lasslop, G.; Lindroth, A.; Lomas, M.; Luyssaert, S.; Margolis, H.; Oleson, K. W.; Roupsard, O.; Veenendaal, E.; Viovy, N.; Williams, C.; Woodward, F. I.; Papale, D. Terrestrial Gross Carbon Dioxide Uptake: Global Distribution and Covariation with

Climate. *Science* **2010**, *329* (5993), 834–838. https://doi.org/10.1126/science.1184984.
(188) Aragão, L. E. O. C.; Malhi, Y.; Roman-Cuesta, R. M.; Saatchi, S.; Anderson, L. O.; Shimabukuro, Y. E. Spatial Patterns and Fire Response of Recent Amazonian Droughts. *Geophysical Research Letters* **2007**, *34* (7), 2006GL028946. https://doi.org/10.1029/2006GL028946.
(189) Tuinenburg, O. A.; Staal, A. Tracking the Global Flows of Atmospheric Moisture and Associated Uncertainties. *Hydrology and Earth System Sciences* **2020**, *24* (5), 2419–2435. https://doi.org/10.5194/hess-24-2419-2020.
(190) Loarie, S. R.; Asner, G. P.; Field, C. B. Boosted Carbon Emissions from Amazon Deforestation. *Geophysical Research Letters* **2009**, *36* (14). https://doi.org/10.1029/2009GL037526.
(191) Landis, J. D.; Obrist, D.; Zhou, J.; Renshaw, C. E.; McDowell, W. H.; Nytch, C. J.; Palucis, M. C.; Del Vecchio, J.; Montano Lopez, F.; Taylor, V. F. Quantifying Soil Accumulation of Atmospheric Mercury Using Fallout Radionuclide Chronometry. *Nat Commun* **2024**, *15* (1), 5430. https://doi.org/10.1038/s41467-024-49789-7.
(192) Guédron, S.; Amouroux, D.; Tessier, E.; Grimaldi, C.; Barre, J.; Berail, S.; Perrot, V.; Grimaldi, M. Mercury Isotopic Fractionation during Pedogenesis in a Tropical Forest Soil Catena (French Guiana): Deciphering the Impact of Historical Gold Mining. *Environ Sci Technol* **2018**, *52* (20), 11573–11582. https://doi.org/10.1021/acs.est.8b02186.
(193) Cao, Q.; Hu, H.; Yuan, W.; Huang, J.-H.; Fu, X.; Feng, X. Isotope-Based Characterization of Soil Elemental Mercury Emissions from Historical Mercury Mining Areas: Driving Pathways and Relative Contributions. *Environ. Sci. Technol.* **2024**, acs.est.4c05220. https://doi.org/10.1021/acs.est.4c05220.
(194) Zhang, H.; Tan, Q.; Zhang, L.; Fu, X.; Feng, X. A Laboratory Study on the Isotopic Composition of Hg(0) Emitted From Hg-Enriched Soils in Wanshan Hg Mining Area. *Journal of Geophysical Research: Atmospheres* **2020**, *125* (19), e2020JD032572. https://doi.org/10.1029/2020JD032572.
(195) Zheng, W.; Hintelmann, H. Nuclear Field Shift Effect in Isotope Fractionation of Mercury during Abiotic Reduction in the Absence of Light. *J. Phys. Chem. A* **2010**, *114* (12), 4238–4245. https://doi.org/10.1021/jp910353y.
(196) Bergquist, B. A.; Blum, J. D. Mass-Dependent and -Independent Fractionation of Hg Isotopes by Photoreduction in Aquatic Systems. *Science* **2007**, *318* (5849), 417–420. https://doi.org/10.1126/science.1148050.
(197) Fritsche, J.; Obrist, D.; Alewell, C. Evidence of Microbial Control of Hg^0 Emissions from Uncontaminated Terrestrial Soils. *Z. Pflanzenernähr. Bodenk.* **2008**, *171* (2), 200–209. https://doi.org/10.1002/jpln.200625211.
(198) Telmer, K.; Costa, M.; Simões Angélica, R.; Araujo, E. S.; Maurice, Y. The Source and Fate of Sediment and Mercury in the Tapajós River, Pará, Brazilian Amazon: Ground- and Space-Based Evidence. *Journal of Environmental Management* **2006**, *81* (2), 101–113. https://doi.org/10.1016/j.jenvman.2005.09.027.
(199) Lino, A. S.; Kasper, D.; Guida, Y. S.; Thomaz, J. R.; Malm, O. Total and Methyl Mercury Distribution in Water, Sediment, Plankton and Fish along the Tapajós River Basin in the Brazilian Amazon. *Chemosphere* **2019**, *235*, 690–700. https://doi.org/10.1016/j.chemosphere.2019.06.212.

(200) Maurice-Bourgoin, L.; Quemerais, B.; Moreira-Turcq, P.; Seyler, P. Transport, Distribution and Speciation of Mercury in the Amazon River at the Confluence of Black and White Waters of the Negro and Solimões Rivers. *Hydrological Processes* **2003**, *17* (7), 1405–1417. https://doi.org/10.1002/hyp.1292.
(201) Maia, P. D.; Maurice, L.; Tessier, E.; Amouroux, D.; Cossa, D.; Moreira-Turcq, P.; Etcheber, H. Role of the Floodplain Lakes in the Methylmercury Distribution and Exchanges with the Amazon River, Brazil. *Journal of Environmental Sciences* **2018**, *68*, 24–40. https://doi.org/10.1016/j.jes.2018.02.005.
(202) Silva do Nascimento, L.; Abreu Pestana, I.; Seidel, M.; Marques da Silva Junior, J.; Cherene Vaz de Oliveira, B.; Ribeiro Gomes, P.; Koschinsky, A.; Dittmar, T.; de Rezende, C. E. Mercury Concentrations along the Amazon Estuary and Plume: Spatial Trends and Geochemical Processes. *Environmental Research* **2025**, *271*, 121129. https://doi.org/10.1016/j.envres.2025.121129.
(203) Goix, S.; Maurice, L.; Laffont, L.; Rinaldo, R.; Lagane, C.; Chmeleff, J.; Menges, J.; Heimbürger, L.-E.; Maury-Brachet, R.; Sonke, J. E. Quantifying the Impacts of Artisanal Gold Mining on a Tropical River System Using Mercury Isotopes. *Chemosphere* **2019**, *219*, 684–694. https://doi.org/10.1016/j.chemosphere.2018.12.036.
(204) Garnier, J.; Martin, L. A.; Sonke, J. E.; Souza, J.; Quintarelli, J.; Kutter, V.; Roig, H.; Bonnet, M.-P.; Maurice, L.; Adam, E. A. M.; Seyler, P. Mercury Isotope Constraints on Artisanal and Small-Scale Gold Mining Source Contributions and Redox Cycling in the Yanomami Indigenous Territory. *Journal of Hazardous Materials* **2025**, *498*, 139892. https://doi.org/10.1016/j.jhazmat.2025.139892.
(205) Nitschke, N.; Guedron, S.; Tessier, E.; Tisserand, D.; Campillo, S.; Amouroux, D. Evaluation of the Hg Contamination from Gold Mining in French Guiana at the Watershed Scale Using Hg Isotopic Composition in River Sediments. *ACS EST Water* **2024**, *4* (8), 3443–3452. https://doi.org/10.1021/acsestwater.4c00270.
(206) Soares, L. C.; Egreja Filho, F. B.; Linhares, L. A.; Windmoller, C. C.; Yoshida, M. I. Accumulation and Oxidation of Elemental Mercury in Tropical Soils. *Chemosphere* **2015**, *134*, 181–191. https://doi.org/10.1016/j.chemosphere.2015.04.020.
(207) Mesquita, R. D. C. G.; W. Workman, S.; Neely, C. L. Slow Litter Decomposition in a Cecropia-Dominated Secondary Forest of Central Amazonia. *Soil Biology and Biochemistry* **1998**, *30* (2), 167–175. https://doi.org/10.1016/S0038-0717(97)00105-3.
(208) Chambers, J. Q.; Higuchi, N.; Schimel, J. P.; Ferreira, L. V.; Melack, J. M. Decomposition and Carbon Cycling of Dead Trees in Tropical Forests of the Central Amazon. *Oecologia* **2000**, *122* (3), 380–388. https://doi.org/10.1007/s004420050044.
(209) Riihimaki, L.; Zhang, D. Planetary Boundary Layer Height (PBLHTSONDE1MCFARL), 2014-01-01 to 2015-12-01, ARM Mobile Facility (MAO), Manacapuru, Amazonas, Brazil; AMF1 (M1). https://doi.org/10.5439/1991783.
(210) Watmough, S.; Osborne, C. Environmental Contamination Associated with Artisanal Gold Mining in Guyana; 2025. https://doi.org/10.7185/gold2025.29674.
(211) Quintarelli, J. M.; Garnier, J.; Rudrigues de Souza, J. P.; de Sousa Tonhá, M.; Barral, U. M.; Roig, H. L.; Martinez, J.-M.; Santini, W.; Puita, O.; Seyler, P.; Kutter, V.; Souza, J. R. Mercury in River Samples with Artisanal and Small-Scale Gold Mining Influence: The Case of the Upper Madeira River Basin (Brazil/Bolivia).

Journal of South American Earth Sciences **2024**, *145*, 105070. https://doi.org/10.1016/j.jsames.2024.105070.

Chapter 6. Supplemental Information

6.1. Chapter 2 Supplemental Information

6.1.1. Model Parameterization

Only urban areas with nighttime light exceeding 0.6 $\mathrm{nW\ sr^{-1}cm^{-2}}$ for Visible Infrared Imaging Radiometer Suite (VIIRS) and 3 digital numbers (DN) for Consistent and Corrected Nighttime Light Dataset (CCNL) are included in urban emissions modeling. Figure SI 6-2 plots the nighttime light of known mining towns in Madre de Dios with either elevated mercury levels[15] or documented mining shops.[53] Most towns exceed this threshold across years with only 4 year-town combinations falling below it.

As noted in section 2.2 of the main text, Carrillo-Tudela & Li[33] recommend a distance decay power of 2.49 for a gravity model of how far reference-price mineral goods are transported across the Andean region for processing. The mean log-squared error between modeled and measured mercury levels is minimized with a decay power of 3.7, and the 95% confidence interval ranges from 3.0 to 4.3 (see Figure SI 6-1). Across this range of decay powers, maximum likelihood emissions estimates range from 102% to 115% of the 156 $\mathrm{kg\ km^{-2}}$ presented in section 2.3.1 of the main text. With mercury data from only a few distinct towns, we cannot conclude whether this optimization represents a true improvement or model uncertainty, so we use the 2.49 power from Carrillo-Tudela & Li.[33]

6.1.2. Lagrangian Transport Modeling

The transport model ignores initial deposition of mercury into soils and leaf stomata before bringing the mercury vapor above the canopy. During turbulent daytime conditions, air residence times within Amazon canopies are on the order of minutes[168] so air quickly rises before it can deposit into foliage or soil, but during nighttime stable atmospheric conditions this assumption may fail. In this case, at SMDN's 1-km resolution, near-field (<< 1 km) deposition of vaporized mercury is indistinguishable from non-vapor mercury leakage at mining sites.

We modeled advection within the PBL for 24 hours and out to 60 kilometers (121 km × 121 km bounding square from the point of emission). During preliminary tests, we found that additional time negligibly increased modeled downwind mercury concentrations $< 0.5\ \mathrm{ng\ m^{-3}}$.

We calculated vertical dispersion using surface similarity theory following Venkatram,[169] with Obukhov lengths and friction velocities estimated according to the ERA5 recommended method.[170] We applied a 0.8 $\mathrm{ms^{-1}}$ wind speed correction[171] to account for ERA5's underestimation resulting from spatial and temporal smoothing of unbiased mean velocities. We considered the boundary layer as well mixed when concentrations from complete mixing exceed ground-level concentrations implied by

vertical dispersion alone (the standard deviation of vertical dispersion: $\sigma_z \geq \sqrt{\frac{2}{\pi}}$ * PBL Height). Our conceptual model assumes that mercury then spreads uniformly to the PBL height during expansion, remains in a residual layer during PBL contraction, and entrains back into the PBL layer during re-expansion. Since deep convection drives Amazon mixing into the free troposphere,[172] we assume air remains in the combined PBL and residual layers except during deep convection events (convective available potential energy > 1000 J kg^{-1}[173]) when the PBL fully mixes with the free troposphere.

ERA5 atmospheric parameters are updated hourly, except PBL height, which is interpolated between hourly estimates. However, estimates are not updated spatially, which assumes negligible spatial gradient in atmospheric parameters over model distances (<60 km).

Particles were tracked at 1-minute (first hour), 5-minute (second hour), and 15-minute (subsequent hours) intervals, with higher early resolution reflecting greater fractional sensitivity of dispersion coefficients. We thereby produced Lagrangian plumes (see Figure SI 6-4), which estimate the downwind increase in concentration ($\mathrm{ng\ m}^{-3}$) per emission ($\mathrm{kg\ year}^{-1}$) at a source pixel, by aggregating particle residence times in each 1-km grid cell within a 121 km × 121 km domain, weighted by inverse mixing height.

To translate downwind above-canopy to below-canopy modeled mercury concentrations, we deployed passive-mercury samplers at 58 meters and 1.75 meters along flux towers at Los Amigos (2023-2024 and 2024-2025), Kilo flux tower (2023-2024 and 2024-2025), and Tambopata (2024). A linear regression estimates that for every additional $\mathrm{ng\ m}^{-3}$ in the PBL, air near ground level increases by 0.66 $\mathrm{ng\ m}^{-3}$ (see Figure SI 6-5). This lower sensitivity of below-canopy than above-canopy concentrations to transported emissions occurs due to ecosystem uptake and long nighttime residence times of ground-level air before it remixes with air above the canopy.

We bicubically interpolated Lagrangian plumes (121 km × 121-km each) across ERA5's 0.25° resolution to generate plumes at actual emission sites. These Lagrangian plumes estimate the downwind concentrations ($\mathrm{ng\ m}^{-3}$) per mercury emission ($\mathrm{kg\ year}^{-1}$) at a given emission site. See SI section 6.1.3 for Lagrangian plume uncertainty analysis.

6.1.3. Lagrangian Transport Model Uncertainty

In addition to random standard error resulting from likelihood estimation, emissions estimates are subject to three potential sources of bias: Lagrangian transport bias, a variable relationship between above-canopy concentrations and those at ground level, and ecosystem uptake reducing distant footprint concentrations.

We can bound this first term by considering the fraction of mercury absorbed through ecosystem uptake pathways. If litterfall dominates ecosystem fluxes—note that throughfall and precipitation transport particulate mercury rather than gaseous elemental mercury and may thus be ignored—and prior litterfall flux estimates[19] scale with modeled air-mercury concentrations, we estimate that only 10% of gaseous elemental mercury fails to reach the upper atmosphere. This implies that at least 90%

of mercury modeled at downwind locations remains when ecosystem loading is accounted for, implying at most a 10% upward bias in Lagrangian plumes and a 10% downward bias in emissions.

We estimate biases in the relationship of above-canopy and below-canopy mercury levels by considering different cover types. Figure SI 6-5 shows a 66.3% scaling factor with only a 0.6% standard error. However, all 5 samples were collected at flux towers in dense canopies. In deforested sites, we anticipate a higher fraction of mercury concentration seen at 58 meters will be observed at ground level due to higher turbulence and less ecosystem uptake. Due to insufficient data, we cannot model the mercury gradient response to canopy cover, but we bound it with a worst case where the fraction of additional mercury seen at ground canopy is a linear function between 66.3% under full canopy cover to 100% under no canopy cover. This upper bound likely overestimates the fraction of mercury seen below the canopy in partially canopy covered pixels where forests dampen turbulence in nearby deforested pixels (consistent with a non-linear relationship of eddy diffusivity and leaf area index[168]); this may further overestimate the fraction seen under no-forest cover where lower turbulence due to surface roughness and soil uptake may reduce this fraction. Overall, this worst case likely overestimates the true fraction of mercury seen at ground level under less-than-full canopy cover.

Lastly, we estimate potential systematic biases in particle transport modeling at a regional to national scale. We ignore bias in horizontal transport since this will already be captured in observed footprint errors that will inform standard errors of regression coefficients. For emissions estimation, we focus on biases in ERA5 planetary-boundary-height estimates. Although surface similarity theory has bias, it is relevant only at near-field distances; since we excluded measurements within 1 kilometer of known emissions sources, this bias will likely not drive overall biases in maximum-likelihood estimates of emissions.

For medium-field dispersion, we instead consider potential bias in boundary height estimates. Past work[174] in the Brazilian Amazon noted an underestimation of nighttime planetary boundary layer (PBL) height, which likely drives bias. At medium distances, footprints are proportional to the inverse of the boundary-layer height. Using 2014 radiosonde data,[175] we find on average a 3% overestimation of this quantity by ERA5 (see Figure SI 6-6). Applying a bootstrap resampling we estimate a 95% confidence interval on true average inverse PBL height of [89%,106%]. This implies a [94%,112%] confidence interval of emission estimates resulting from PBL bias.

To estimate the total bias in emissions estimates, we bootstrapped PBL-height biases, applied a worst-case below-canopy-conversion, and statistical error confidence intervals. We bootstrapped maximum likelihood estimation by the probability distribution calculated for inverse PBL height, resulting in a 95% confidence interval on

emissions of [84%, 126%]. Adjusting the lower bound to account for a potential overestimation in the fraction of mercury at 58 meters that is observed at ground level in pixels with partial or no canopy, the confidence interval on emissions estimates extends to [77%, 126%].

6.1.4. Uncertainty in Kilometer-Scale Emission Modeling

For uncertainty analysis, we calculated log standard deviations; however, they are presented as a multiplicative error. A 2-fold standard deviation means that for 68% of mining pixels, true emissions lie between ½ and 2x the estimated average.

For pixels where informal gold mining occurs following mining deforestation, we estimate the uncertainty of emission rate by analyzing each term in:

$$\frac{\text{Hg Emissions (kg)}}{\text{Area (km}^2\text{)}} = \frac{\text{Dredged Area (km}^2\text{)}}{\text{Total mined area (km}^2\text{)}} * \frac{\text{Gold (kg)}}{\text{Dredged Area (km}^2\text{)}} * \frac{\text{Hg Vapor (kg)}}{\text{Gold (kg)}}$$

To estimate the proportion of mining deforestation that is dredged, we estimate mining pond extent. We estimate mining pond extent corresponding to mining between 2001 and 2020 as the change in 30-m water cover between 2000 and 2021[176] aggregated to square-km pixels. Restricting to 1-km pixels that were >99% mined during this period, we find a geometric mean of 39% of dredged area, with a 1.98-fold standard deviation.

We estimate the gold per dredged area by considering the depth of mining ponds and the gold concentration in raw mined sediment. We utilize past findings that mining pond depths in Ethiopia[177] averaged 3.2 meters with a 22% uncertainty, which is consistent with anecdotal evidence of 3 to 4 meter mining pond depths noted in the Peruvian Amazon.[178] Gasparinnetti et al[108] compiled estimates of 0.19, 0.4, and 1.2 grams of gold extracted per tonne of sediment processed based on prior Brazilian data collection,[179,180] implying a geometric mean of 0.45 grams tonne^{-1} with a 2.5-fold standard deviation. We assume there is negligible variation in their sediment-density estimate of 2.76 tonnes m^{-3}. These estimates imply a (geometric) average of 4.0 grams of gold per area dredged with 2.7-fold uncertainty. We assume the efficiency rate of gold extracted per gold in dredged sediment is relatively consistent across mining sites and contributes negligible uncertainty for this analysis.

Lastly, we estimate variation in the ratio of mercury vaporized to gold produced. Note that amalgamation chemistry makes this ratio more constrained than the ratio of all mercury used in the mining process which includes leakage into tailings and waterways and can range from 1:1 to greater than 10:1 found at both the country[107] and international scale.[2] The atmospheric component is determined by the species of mercury-gold compounds that form in amalgam. Average ratio in amalgam has been estimated at 1:1,[45,107] but we estimate that it may range as high as 2:1 given that the gold mercury ($AuHg_2$) amalgam is the highest ratio of mercury to gold in a stable forming

compound[181] and will form under abundant mercury conditions. Based on these three estimates of 1:1, 1:1, and 2:1, with an estimated true average ratio of 1:1, we estimate a 1.49-fold standard deviation.

Combining estimated means and standard deviations in dredged area per total mining deforestation, gold production per dredged area, and atmospheric mercury emissions per gold produced, this analysis leads to an estimate of 1600 kg of mercury emitted to the atmosphere per km^2 mined with a 3.6-fold uncertainty. The geometric mean estimated here should not be given much weight, as its order-of-magnitude estimation ignores features of mining that would inform exact production rates. SMDN's per-area emission estimate of 156 kg km^{-2} is substantially lower than this estimate, suggesting there may be additional inefficiencies. Past field Amazon research[182] has noted that informal gold mining using mercury amalgamation recovers less than 30% of gold in the sediment; with that adjustment, the back-of-the-envelope estimate here is within 2 standard deviations of the SMDN's estimate. Furthermore, the 3.6-fold standard deviation likely reflects real variability across sites; this may be used as an order-of-magnitude estimate of true inter-pixel variation in emission rate per km^2 mined.

6.2. Chapter 3 Supplemental Information

6.2.1. Speculated Agricultural Productivity Declines

Prior research has noted that soil-mercury exposure negatively impacts growth, survival, and health of Amazon agricultural plants.[80] Overlaying footprints onto agricultural lands[71] and applying the fractional productivity loss estimates per mercury exposure, we speculate that there could be a 0.2% loss in crop productivity across the Amazon's 20 million hectares of farmlands. Applying a past estimate of $797 agricultural income loss per hectare of lost Brazilian Amazon agricultural yields,[183] mercury degradation due to gold mining accounts for an estimated $30 million per year cost to Amazon farmers.

Restricting to urban lands (VIIRS[34] > 0.6 $\mathrm{nW\ str^{-1}cm^{-2}}$ based on prior research's urban threshold[36]), a parallel analysis speculates a 0.6% loss in urban agricultural yields, which play an important role in Amazon diets and provide a substantial portion of fruits and vegetables consumed by urban residents.[184] This suggests that mercury's effect on food systems could extend beyond dietary exposure risks by modestly reducing food production.

6.2.2. Potential Global Plant Productivity Declines

To estimate the potential global GPP impacts from Amazon mercury emissions, we focus on the 57% of emissions that fail to absorb regionally (see Chapter 4): of the 80 $\mathrm{t\ a^{-1}}$ of Amazon gold mining emissions (see Chapter 2), 46 $\mathrm{t\ a^{-1}}$ likely reach the free troposphere and enter global circulation. We apply a simplifying assumption that these

emissions distribute globally, rather than just hemispheric circulation, before reentering ecosystem cycling. We use a 1 year atmospheric lifetime of gaseous elemental mercury consistent with past studies[185,186] to distribute these 46 t a^{-1} of added atmospheric mercury from Amazon mining uniformly across 4.0×10^{18} kg of troposphere. Applying a ground-level air-density of 1.2 kg m^{-3}, we estimate a 9.1 pg m^{-3} increase in global surface level concentrations resulting from Amazon mining emissions. We further assume that the earth's 122 billion tonnes of global annual terrestrial GPP[187] are degraded at the same rate per mercury exposure as the Amazon. With these simplifying assumptions, on the order of 41 Mt a^{-1} global GPP loss could result from a global mercury increase, representing a speculated 177% increase over the local GPP impacts alone.

6.2.3. Mining Reduces Downwind Precipitation and Accelerates Forest Die-Off

We follow past maximum cumulative water deficit (MCWD) research,[95,188] assuming that Amazon rainforests transpire 100 mm $month^{-1}$ meaning that when precipitation is below that threshold water deficit accumulates. Using ERA5 precipitation data, we calculated water deficits for each month between 2001 and 2024 and extracted the MCWD for each year.

For each downwind pixel with potential MCWD increase due to mining, we calculated the time during which its MCWD accumulated. For each downwind pixel's selected months of accumulation, we use estimated transpiration rates from ERA5-land to calculate each upwind pixel's transpiration loss during those months.[120] We calculate the 2024 transpiration declines due to mining, by aggregating those months reductions from mining deforestation (a complete loss of transpiration) and reductions from mercury degradation (a loss proportional to GPP loss per optimal stomatal theory[101]). We used the UTRACK-atmospheric-moisture model, which modeled 2008-2017 average precipitation in each global $0.5°$ pixel per evaporation in each $0.5°$ pixel,[189] to estimate the resulting precipitation loss at the selected downwind pixel.

We predict forest-transition impacts under average annual MCWD conditions but at a modern (2024) mining scenario. We therefore predict how the current state of aggregate mining scars and mercury degradation of Amazon rainforests will lead to die-off if they stay constant. On the other hand, we account for inter-annual climate variability, using MCWD, the timespan of deficit accumulation, and upwind transpiration rates between 2001 and 2024.

We assume that in the transition zone between -350 and -450 MCWD[104] there's a continuous 1% per mm MCWD reduction in long-term forested probability. In each year, we aggregated the probability per South American pixels (this includes both the Amazon and potential forests downwind influenced by its atmospheric river) of being

forested under a baseline no-mining scenario and with mining impacts exacerbating MCWD. We calculate that the average difference, across years, of equilibrium forested area is approximately 1500 km^2.

Applying an Amazon average 23 kt C per km^2 biomass from deforestation estimate,[190] losing the speculated 1500 km^2 of forest equates to a 35 Mt loss in carbon stocks. These speculated losses in carbon stocks, aggregated across future years where forest die-off may occur, equate to a $24 (CI: [$6, $53]) billion social valuation or 18% of the total valuation of all gold production between 2001 and 2024 in the Amazon.

6.3. Chapter 4 Supplemental Information

6.3.1. Eddy Diffusivity Model Parameterization

Section 4.2.3's optimization calibrates a=1.06 m, $p_1 = 0.3$, $p_2 = 1.26$, $c_1 = 15.1$, and $c_2 = 0.34$. This parameterization allows us to explain 72% of the variance in measured heat fluxes. The estimates for p_1 and p_2 are consistent with prior estimates[126] of $p_1 = 0.25$, and $p_2 = 1$, suggesting that a similar functional form of stability function applies. Estimates for α and c_2 are consistent with those prior estimates[126] of the Van Kármán constant $k = 0.4$ and $c_2 = 4.0$ with a 2.6 m height above displacement (equivalent to the geometric mean of the 16 m and 58 m heights above a 15.84 m zero-displacement height). However, the $c_1 = 15.1$ estimate matches prior estimates[126] at $c_1 = 15.0$ with no displacement height adjustment applied. Together, this comparison suggests that the Obukhov similarity theory framework continues to apply. However, the zero-displacement height for the baseline calculation becomes very close to the lower measurement height, and this displacement height also applies to the stability function adjustment needed during turbulent unstable (L<0) conditions. However, during (night-time) stable conditions, the stability function adjustment is consistent with past estimates with a displacement height near ground level.

6.3.2. Residence Time of Soil Mercury

We estimate the residence time of soil at different depth profiles, by dividing stored soil mercury to a depth profile by an estimated equilibrium flux rate. We argue that a prior study's[19] 30-50 cm soil depths represent pre-industrial equilibrium concentrations: with minimum observed concentrations at those depths, it would require 180-800 years at post-industrial background atmospheric mercury levels (approximated at $1\ \mathrm{ng\ m^{-3}}$ implying a loading flux of 68 $\mu\mathrm{g\ m^{-2}\ a^{-1}}$) to replace the top 30 cm of mercury alone. This estimate, which exceeds the time-scale of industrialization, represents a lower bound as it would require recently deposited mercury to remain in soils during the calculated timescales—in reality, recently deposited surficial mercury likely evades at a much higher rate than longer-term and deeper mercury stores.[191]

We assume that 30-50 cm depth soils equilibrated to pre-industrial background air-mercury levels[137] (0.27 CI: $[0.18,\ 0.40]\ \mathrm{ng\ m^{-3}}$), with a corresponding 20 CI: $[13, 29]$

$\mu g\ m^{-2}\ a^{-1}$ loading flux. For author's 10-15 cm measurements, we assume they lie somewhere between the pre-industrial equilibrium and equilibrated to post-industrial background mercury concentrations (approximately 1.22 $ng\ m^{-3}$ above the canopy as found in Chapter 2) implying a flux of 13-73 $\mu g\ m^{-2}\ a^{-1}$.

6.3.3. Evasion Pathways at High Relative Elevations

We consider potential explanations for the depleted Δ^{199} seen at relative elevation high points (see Figure 4-7b). We argue that an ongoing fractionation process is likely responsible as opposed to a legacy pre-industrial signal hypothesized by past studies.[113,192] For this depleted Δ^{199} to hypothetically reflect a pre-industrial signal, then modern uncontaminated sites where Δ^{199} matches air (~0.2‰ for background sites) must have fully recycled their soil mercury after industrialization. This non-depletion has been observed for soils down to 50 cm at the background sites Boca Manu and Cocha Cashu[113] (in addition to some contaminated sites). Therefore, background mercury inputs would have to have been sufficient to fully recycle mercury down to this depth. At a post-industrial background (around 1 $ng\ m^{-3}$ implying a loading flux of $73\ ng\ m^{-2}\ a^{-1}$) it would take a minimum of 310 and 230 years (for Boca Manu and Cocha Cashu, respectively) to load the total mercury observed in the top 50 cm of soil, which already exceed the 150-year timescale of industrialization. Furthermore, these estimates represent a lower bound that likely underestimates the true time since deeper soil horizons were deposited, since evasion and erosion loss pathways occur in the surficial soil horizon, and these background sites' substantially larger soil mercury concentrations in surficial mineral soils than deeper depths indicate that industrial mercury inputs have yet to equilibrate deeper depths. Therefore, it seems unlikely that industrialization alone explains the differential Δ^{199} observed between sites.

In place of the preindustrial MIF depletion story, we propose that a pedogenic process continuously depleted MIF throughout a soil's history. We considered the potential role of evasion via photoreduction, dark abiotic reduction, and microbial reduction to explain the observed data. Microbial reduction is not known to induce a mass-independent fractionation,[193] but photoreduction and dark abiotic reduction of soil mercury can both preferentially emit odd isotopes from soils[194,195] due to a magnetic isotope effect and nuclear volumetric effect, respectively. However, we can distinguish the two processes by their odd isotope fractionation ratios. Photoreduction is associated with a Δ^{201}: Δ^{199} of 1:1-1.3 (the lower end indicates inorganic mercury photoreduction whereas the higher end indicates organic mercury photoreduction),[196] whereas the nuclear volumetric effect is characterized by a 1:1.5-1.6 ratio.[195] Our soil samples fit a line with slope $\Delta^{201}: \Delta^{199} = 1: 1.28 \pm 0.11$ as shown in Figure SI 6-10. In long-term equilibrium (where inputs equal outputs), soil mercury will differ from input fractionation by the mean intrinsic fractionations across loss processes, weighted by the fraction of loss occurring through each pathway. Our observed ratio is consistent

with the upper end of photoreduction; however, the low percent of soil mercury typically occurring in organic forms suggests a pure photoreduction story may not fully fit the data; a mixing of photoreduction and dark reduction may be more consistent with the data.

A substantial photoreduction pathway is counter-intuitive in Amazon forested soils where sunlight rarely reaches the forest floor; however, it is consistent with short periods of disturbance or local canopy loss inducing rapid photo-reduction (see section 4.3.7 for the rapid evasion noted following deforestation). Section 4.3.1 and Figure 4-2 observed that evasion continues to occur during day and night-time in the Los Amigos tower primary forest site, corroborating that there is some other evasion pathway. We observed depleted Δ^{199} in ground-level air (compared with above-canopy air) across sites (see Figure SI 6-11), with the largest effect at the Los Amigos and Kilo tower sites where soil mercury was depleted in Δ^{199}; this depletion suggests that ground-level air samplers observe a mixing of soil mercury Δ^{199} and above canopy air Δ^{199} rather than preferential emission of odd isotopes during normal forested times. In this case, neither dark adaptation nor photoreduction explain all the observed evasion. Microbial reduction could offer an alternative loss pathway as has been observed in Amazon soils.[197] Together these analyses offer a consistent explanation for observed data where photoreduction depletes soil Δ^{199} over pedogenic timescales, dark reduction may occur but as a less prominent pathway of soil-mercury loss, and some other type of (potentially microbial) evasion remains present during typical periods of forest cover. Whichever evasion pathway occurs at high relative elevations, the chapter's main findings hold.

6.3.4. Prior River-Mercury Literature is Consistent with Erosion

The Madre de Dios river contains consistent levels of total suspended solid concentrations across reaches, but higher mercury levels were observed in more downstream river reaches[20]; this difference suggests that similar concentrations of suspended solids arrive from both Andean and Amazon runoff but the latter contains substantially more particulate mercury. This story of sediment-rich low-mercury Andean water mixing with regional sediment-poor higher-mercury runoff is supported by meta-analysis where similar particulate mercury concentrations per volume of water found in research across the Amazon, despite studies in clearwater[198,199] and blackwater[200,201] reaches looking at reaches with orders of magnitude lower total suspended solids than the near-Andean Madre de Dios whitewater reaches (see Table SI 6-3).

Prior studies[198,199] have also shown that this mercury increases with suspended solid across nearby reaches, and these concentrations tend to be highest in the wet season[20] when large rain events can erode more material. This evidence further supports erosion, rather than leaching, as the mercury loss pathway at low relative elevations.

This evidence also argues against direct leakage of liquid mercury released at mining sites that could travel into rivers. Further evidence against direct leakage explaining river mercury levels is provided by Telmer et al[198] who argued that insufficient mercury is leaked this way to explain river mercury concentrations in the heavily mined Creporí river (Tapajós Basin, Brazil). Isotopic (δ^{202}) data from pristine rivers matches nearby soils,[202] further supporting the hypothesis that erosion is a primary driver of these mercury levels; however, in mining regions river mercury δ^{202} appears to mix the observed soil fractionation with a non-depleted source (likely direct leakage), indicating that both sources may contribute to contaminated rivers.[203–205] This isotope data does not contradict section 4.3.6's estimate that a 76 ± 15 % majority of mercury in mining region's larger rivers (e.g. Madre de Dios) arrived via erosion, but it does indicate that direct leakage also plays a role, especially in tributaries surrounded by mining.

A synthesis of prior studies allows us to further distinguish erosion of recent versus long-term soil inputs. River mercury levels have been previously found[198,199] to increase with organic matter concentrations within suspended solids (in addition to river mercury increasing with total suspended solids). Organic matter includes both litterfall mercury inputs, as well as potential direct dry deposition that may first deposit in a thin organic horizon, as has been observed in a prior Amazon forest study.[206] However, Amazon soil organic matter has been previously found to have a decay rate of 0.39-0.61 per year for leaf litterfall[207] and 0.17 per year for woody litter[208]; therefore, if mercury were transported from primarily surficial soil organic matter, it has likely deposited during the prior few years, when atmospheric loading is at approximately modern levels.

6.4. Supplementary Figures

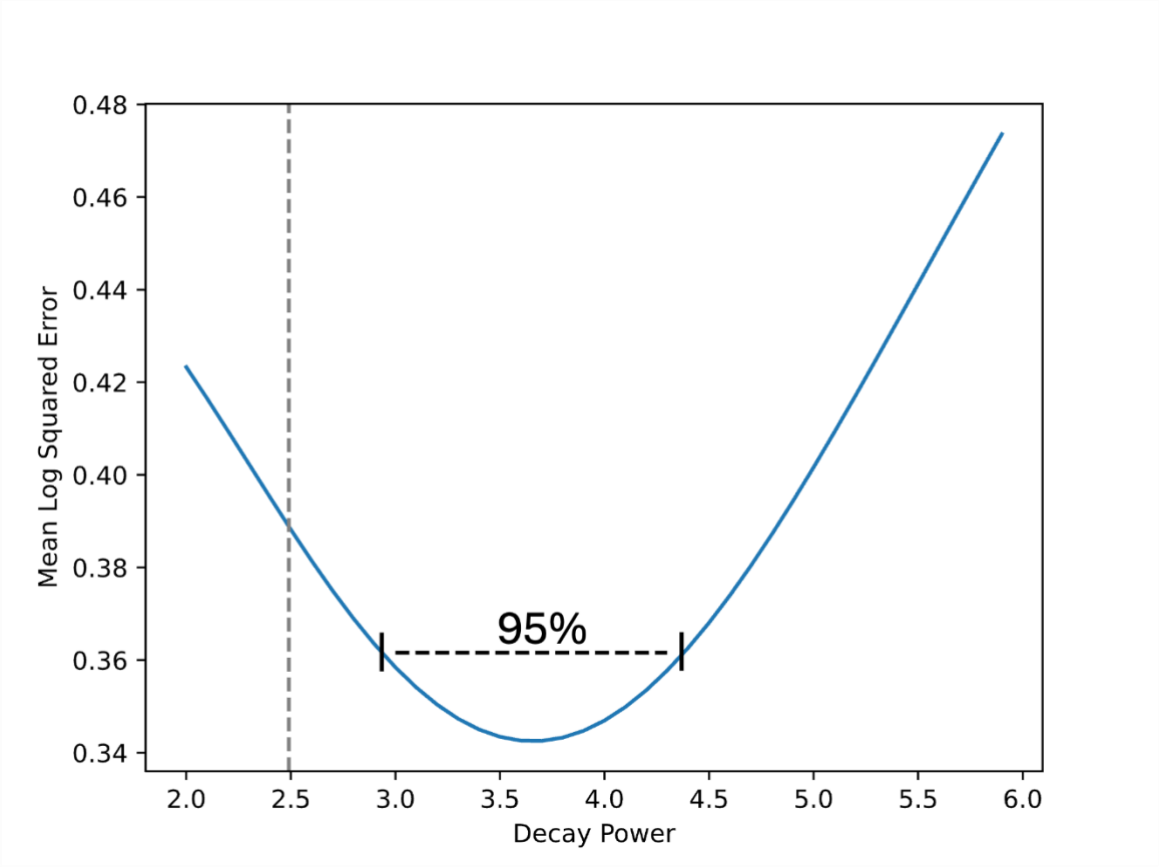

Figure SI 6-1 shows the mean log squared error between measured air-mercury (Hg) levels in calibration data[15] and modeled mercury using the Spatial Mining Deforestation and Nighttime Light (SMDN) model. A vertical line of 2.49 corresponds to the decay power estimated by Carrillo-Tudela & Li[33] for Andean reference-price mineral trade.

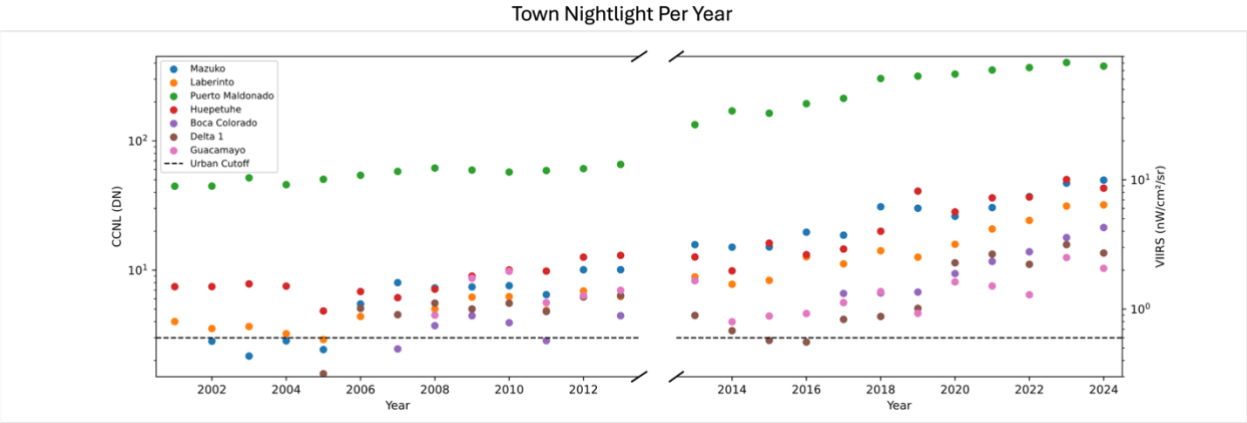

Figure SI 6-2 displays the nighttime light of the most lit pixel for 7 towns in Madre de Dios, Peru, where elevated Hg or mining shops have been observed.[15,53] Previously reported urban cutoffs of 0.6 $nW\ sr^{-1}cm^{-2}$ for VIIRS[36] and 3 digital numbers for CCNL[37] are included. Axes represent *Visible Infrared Imaging Radiometer Suite (VIIRS) and Consistent and Corrected Nighttime Light Dataset (CCNL).*

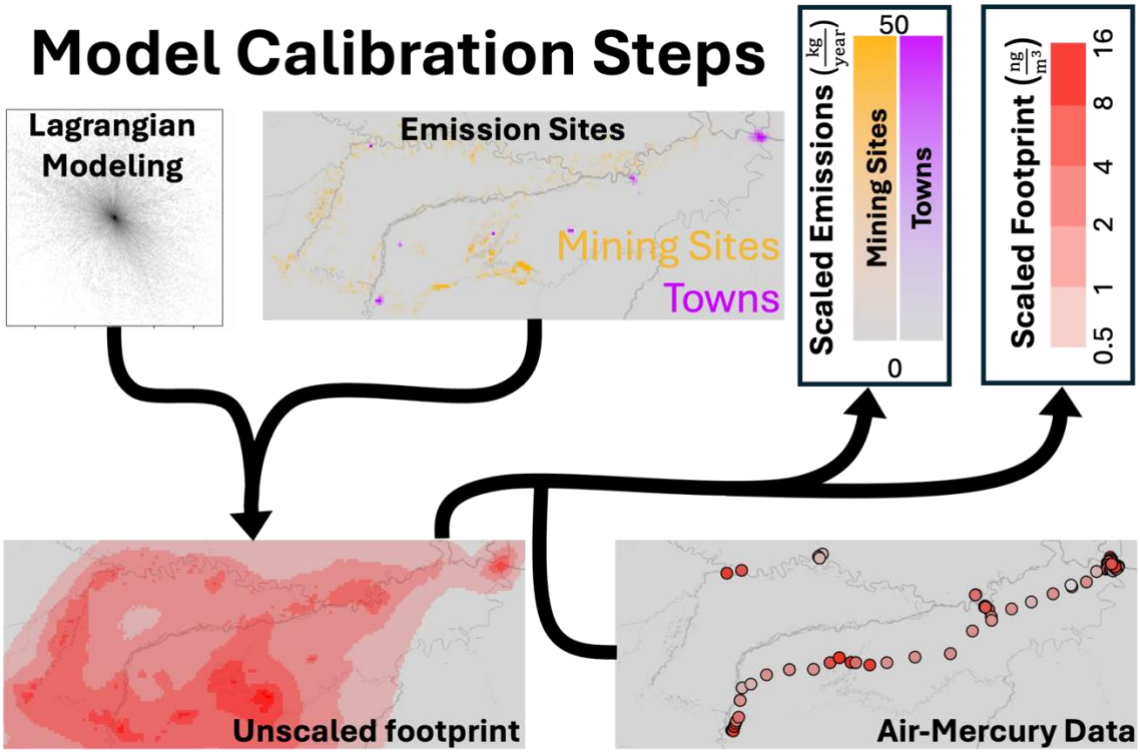

Figure SI 6-3 shows the sequence of steps followed to calibrate the Spatial Mining Deforestation and Nighttime Light model. Mining site and mining town emission pixels were identified via remote sensing and combined with Lagrangian modeling outputs to produce unscaled footprints. Maximum likelihood emission scaling factors were then estimated to produce scaled concentration footprints that best reproduce on-the-ground air-mercury data.

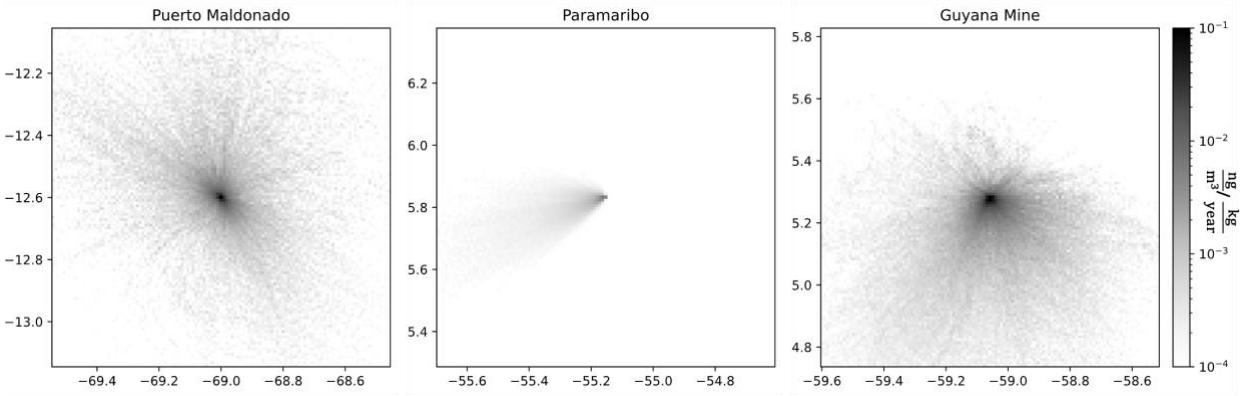

Figure SI 6-4 shows the Lagrangian transport model results for Paramaribo, a Guyana mine, and Puerto Maldonado in 2006, 2018, and 2024 corresponding to the years with air-mercury measurements in validation data.

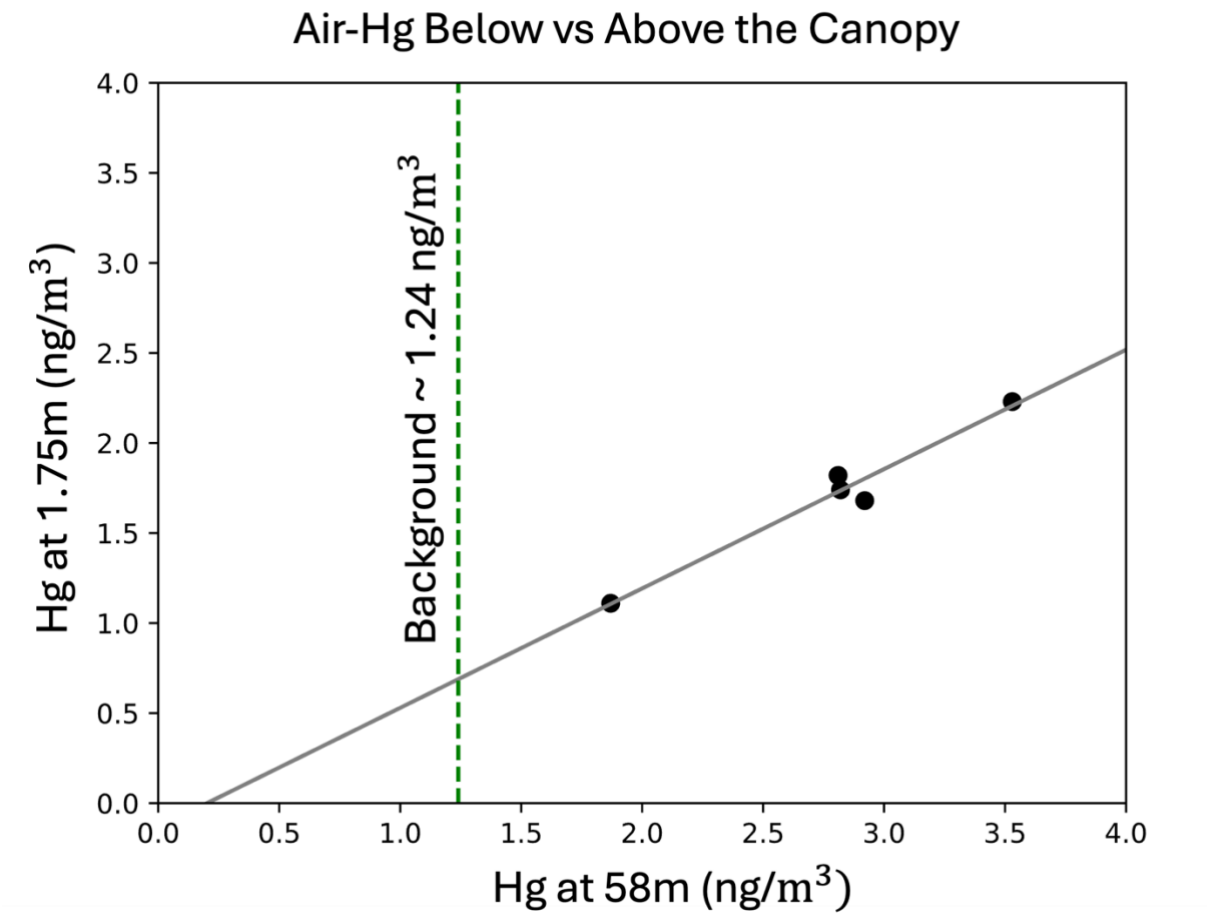

Figure SI 6-5 shows the above canopy (53 meters *at the Tambopata flux tower and 58* meters *at other sites) and below canopy (1.75* m*) mercury (Hg) concentrations. A line of best fit of* Hg_{ground} *= 0.66* Hg_{above} *- 0.13* $ng\ m^{-3}$ *is included.*

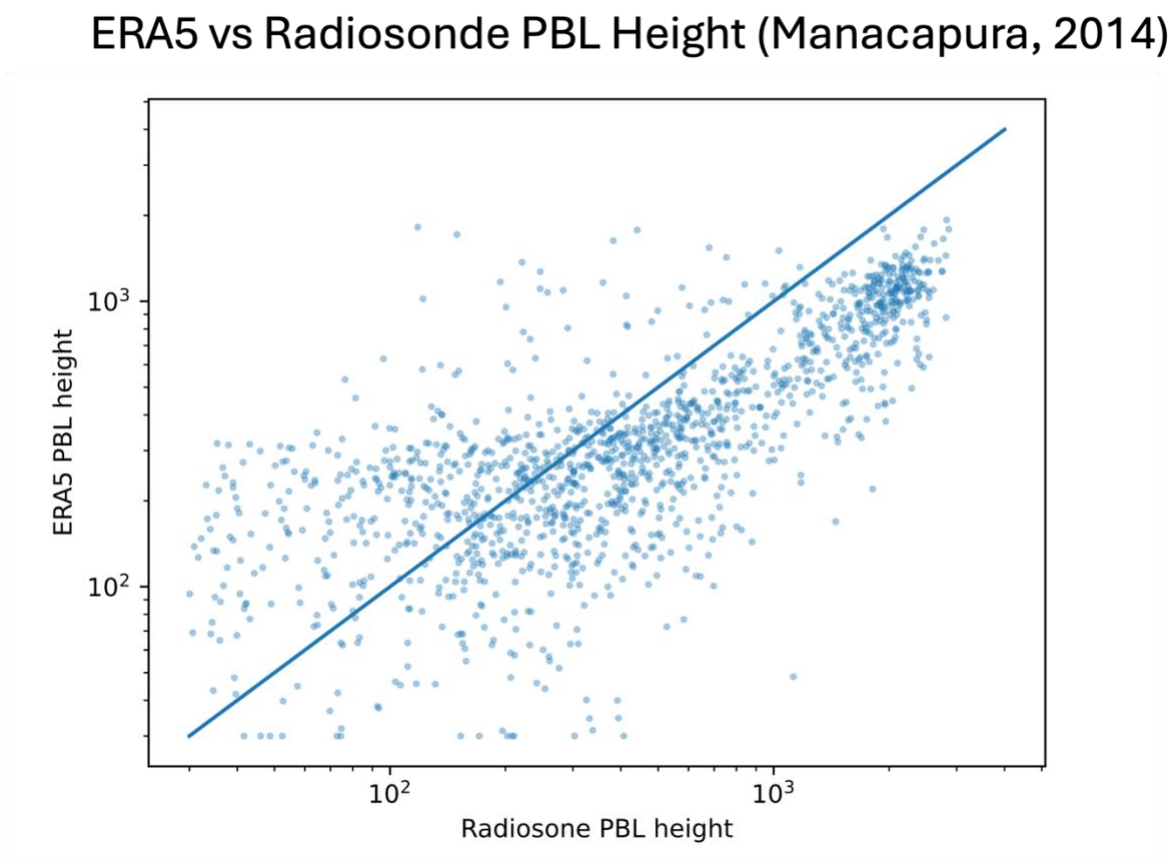

Figure SI 6-6 shows ERA5 and Radiosonde[209] estimates for the planetary boundary layer (PBL) height estimated four times per day at a site near Manaus, Brazil in 2014. A 1:1 line is also included. As found by Dias-Júnior et al[174] there is reasonable agreement between the two datasets for the thicker daytime boundary layer, but they are less correlated at night; however, the overall distribution remains similar across the two datasets.

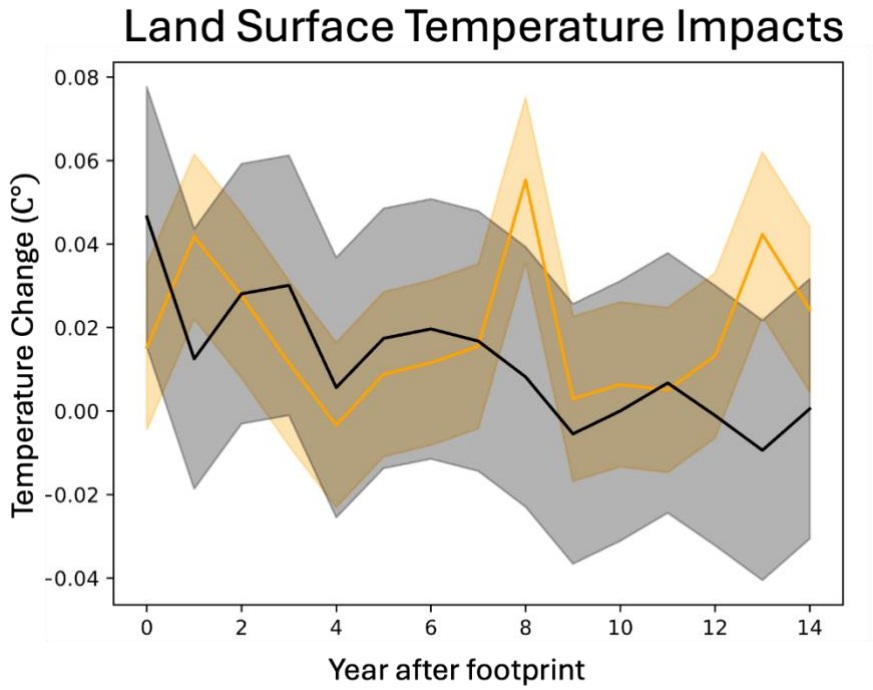

Figure SI 6-7 displays estimated multiple-linear regression coefficients of daytime land surface temperature (over a background-mercury baseline) versus footprints for 0-15 years after modeled mercury concentration footprints (black) and for the non-mining control (orange).

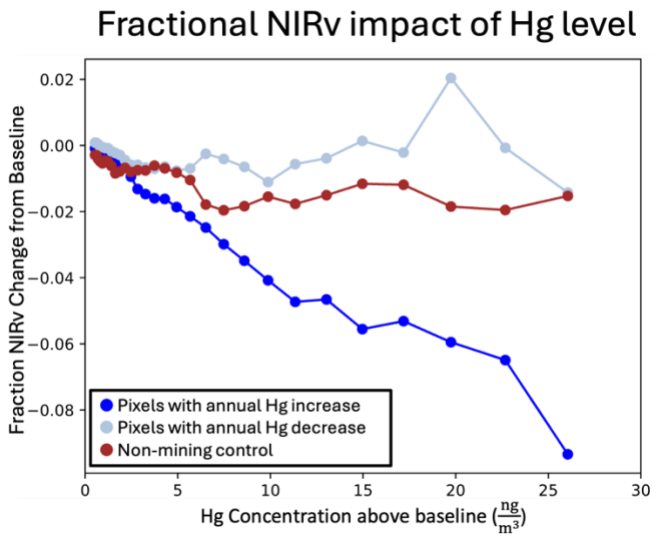

Figure SI 6-8 displays the estimated impact of mercury concentrations controlling for the prior year's concentrations during times of increasing mercury concentrations (blue) and decreasing concentrations (grey), as well during increasing non-mining deforestation control (red). Each scenario is calculated by assigning pixel-year combinations to binned categorical variables for its mercury concentrations, comparing year-to-year change in normalized NIRv with change in the categorical bin variables (-1 if the previous year's bin's categorical variable, 1 in the next year's bin's categorical variable, and 0 in all other categorical variables).

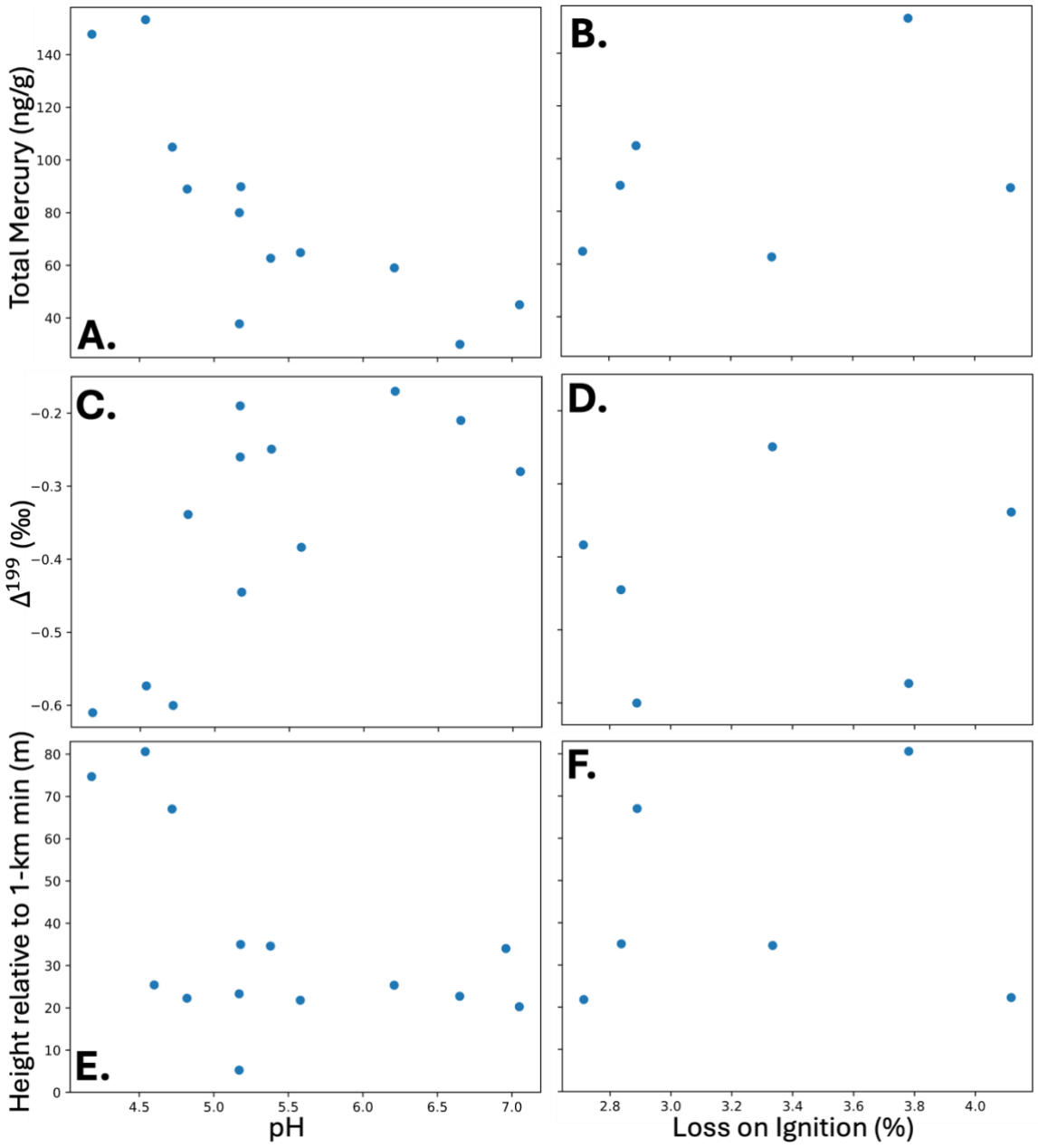

Figure SI 6-9 plots Total mercury (panels A & B), Δ^{199} (panels C & D), and height above the minimum for all pixels within 1 kilometer (panels E & F) against pH (panels A, C, & E) and loss on ignition (panels B, D, & F).

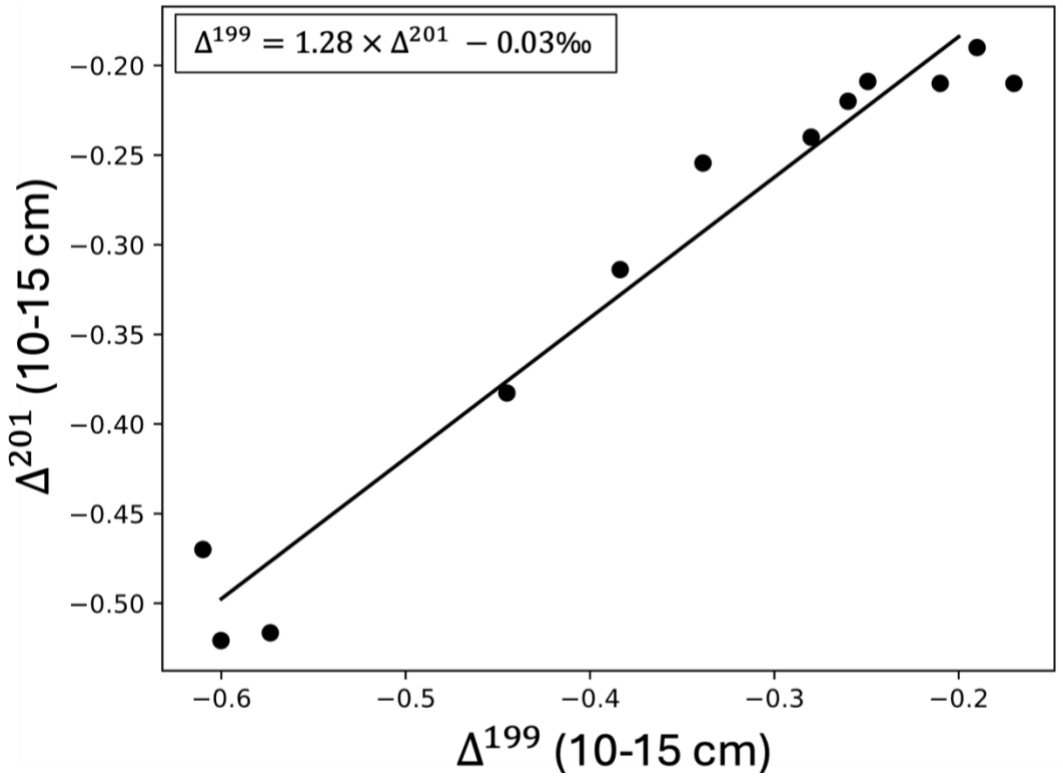

Figure SI 6-10 plots Δ^{201} versus Δ^{199} for soil mercury at 10-15 cm depths, along with the regression line of best fit.

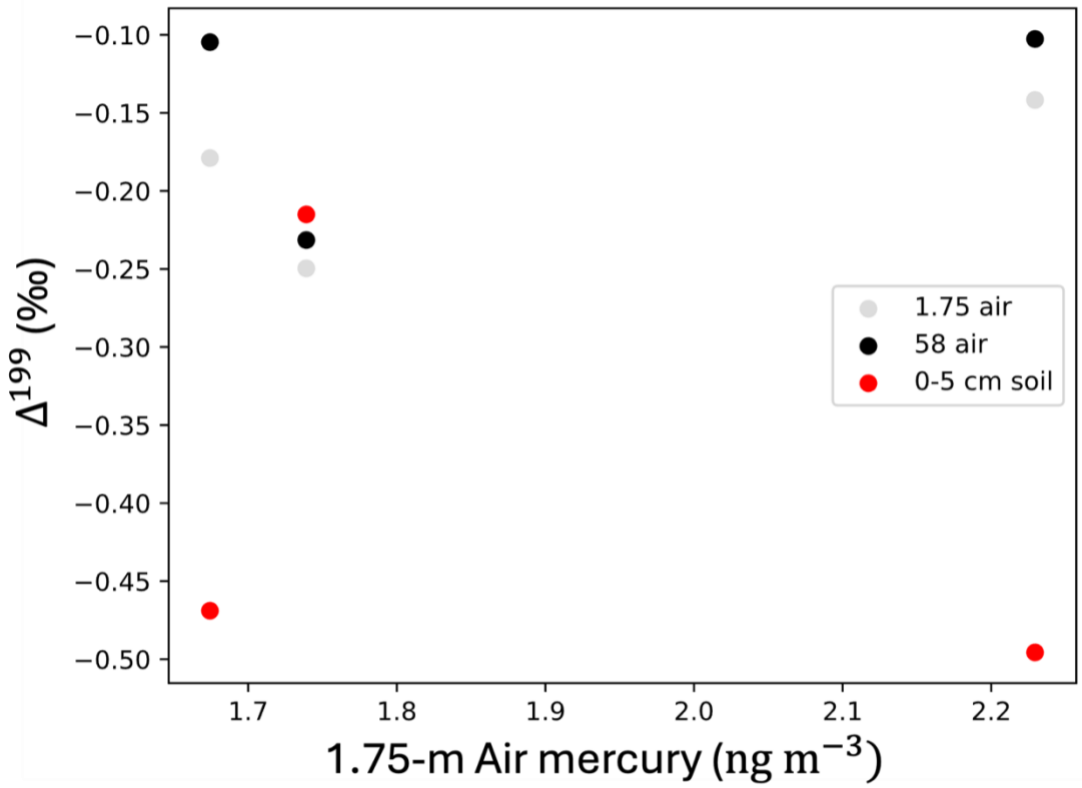

Figure SI 6-11 plots Δ^{199} for 1.75-m air (grey), 58-m air (black), and 0-5 cm soils (red) against air-mercury concentrations.

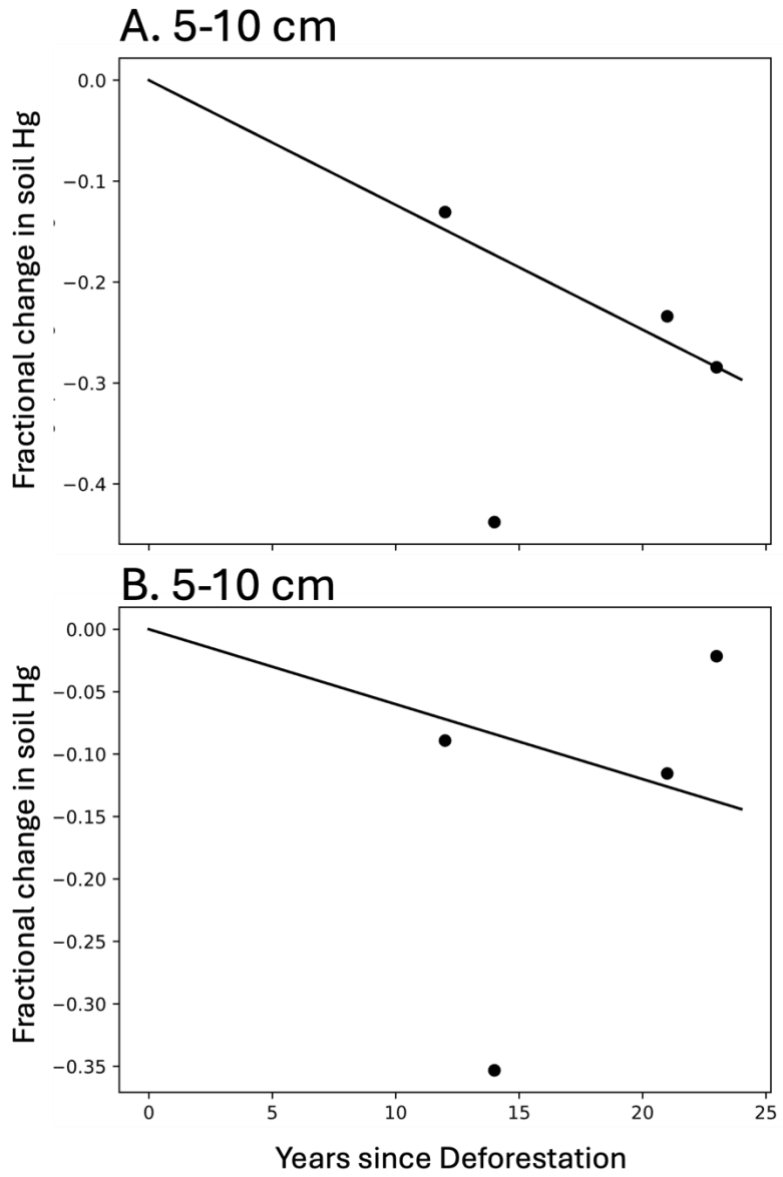

Figure SI 6-12 shows the fractional loss of soil mercury in the 5-10 cm profile (panel A) and 10-15 cm profile (panel B) at deforested versus neighboring forested plots against the estimated number of years since deforestation.

6.5. Supplementary Tables

Table SI 6-1 lists the air-mercury (Hg) concentration data utilized in this study. Sample ID, country, longitude, latitude, deployment date, retrieval date, year (midpoints of deployment and retrieval dates were used for selecting the year of model comparison), average air-mercury concentrations, authors, publication date, and data use (calibration or validation) are included.

ID	Country	Lat.	Long.	Deployment	Retrieval	Year	Hg (ng m^{-3})	Publication	Pub Year	Data Use
PAS-T1-2017	Peru	-12.5667	-69.1997	8/4/17	8/11/17	2017	45.6	Szponar et al[15]	2025	Calibration
PAS-T3-2017	Peru	-12.5739	-69.1989	8/4/17	8/11/17	2017	11.4	Szponar et al[15]	2025	Calibration
PAS-T4-2017	Peru	-12.5736	-69.1953	8/4/17	8/11/17	2017	12.1	Szponar et al[15]	2025	Calibration
PAS-T4-2018	Peru	-12.5736	-69.1953	7/14/18	7/27/18	2018	7.59	Szponar et al[15]	2025	Calibration
PAS-T6-2018	Peru	-12.5786	-69.1961	7/14/18	7/27/18	2018	14	Szponar et al[15]	2025	Calibration

PAS-T7-2017	Peru	-12.5838	-69.2085	8/4/17	8/11/17	2017	7.48	Szponar et al[15]	2025	Calibration
PAS-T7-2018	Peru	-12.5838	-69.2085	7/13/18	7/27/18	2018	7.24	Szponar et al[15]	2025	Calibration
PAS-T8-2017	Peru	-12.5805	-69.2034	8/4/17	8/11/17	2017	8.08	Szponar et al[15]	2025	Calibration
PAS-T11-2017_1	Peru	-12.5971	-69.1843	8/3/17	8/11/17	2017	173	Szponar et al[15]	2025	Calibration
PAS-T11-2017_2	Peru	-12.5971	-69.1843	8/3/17	8/11/17	2017	83.3	Szponar et al[15]	2025	Calibration
PAS-T11-2018	Peru	-12.5971	-69.1843	7/13/18	7/27/18	2018	267	Szponar et al[15]	2025	Calibration
PAS-T14-2017	Peru	-12.5871	-69.1999	8/4/17	8/11/17	2017	11.9	Szponar et al[15]	2025	Calibration
PAS-T15-2017	Peru	-12.5887	-69.1944	8/4/17	8/11/17	2017	17.5	Szponar et al[15]	2025	Calibration
PAS-T16-2017	Peru	-12.5894	-69.1884	8/4/17	8/11/17	2017	10.1	Szponar et al[15]	2025	Calibration
PAS-T17-2017	Peru	-12.5916	-69.1851	8/4/17	8/11/17	2017	24.8	Szponar et al[15]	2025	Calibration
PAS-T18-2017	Peru	-12.5892	-69.2071	8/4/17	8/11/17	2017	11.4	Szponar et al[15]	2025	Calibration
PAS-T20-2017_1	Peru	-12.5923	-69.2014	8/4/17	8/11/17	2017	7.66	Szponar et al[15]	2025	Calibration
PAS-T20-2017_2	Peru	-12.5923	-69.2014	8/4/17	8/11/17	2017	7.42	Szponar et al[15]	2025	Calibration
PAS-T21-2017	Peru	-12.5929	-69.1968	8/4/17	8/11/17	2017	8.92	Szponar et al[15]	2025	Calibration
PAS-T22-2017	Peru	-12.5925	-69.1925	8/4/17	8/11/17	2017	19.9	Szponar et al[15]	2025	Calibration
PAS-T22-2018	Peru	-12.5925	-69.1925	7/14/18	7/27/18	2018	11.6	Szponar et al[15]	2025	Calibration
PAS-T23-2017	Peru	-12.5941	-69.1873	8/4/17	8/11/17	2017	10.9	Szponar et al[15]	2025	Calibration
PAS-T25-2017	Peru	-12.5930	-69.1770	8/4/17	8/11/17	2017	6.78	Szponar et al[15]	2025	Calibration
PAS-T29-2017	Peru	-12.5958	-69.1985	8/4/17	8/11/17	2017	6.71	Szponar et al[15]	2025	Calibration
PAS-T30-2017	Peru	-12.5989	-69.1952	8/3/17	8/11/17	2017	7.45	Szponar et al[15]	2025	Calibration
PAS-T31-2017	Peru	-12.5962	-69.1932	8/3/17	8/11/17	2017	3.63	Szponar et al[15]	2025	Calibration
PAS-T32-2017	Peru	-12.5980	-69.1880	8/3/17	8/11/17	2017	7.35	Szponar et al[15]	2025	Calibration
PAS-T33-2017	Peru	-12.5960	-69.1850	8/3/17	8/11/17	2017	43.5	Szponar et al[15]	2025	Calibration
PAS-T33-2018	Peru	-12.5960	-69.1850	7/14/18	7/27/18	2018	23.5	Szponar et al[15]	2025	Calibration
PAS-T34-2017_1	Peru	-12.5975	-69.1831	8/3/17	8/11/17	2017	239	Szponar et al[15]	2025	Calibration
PAS-T34-2017_2	Peru	-12.5975	-69.1831	8/3/17	8/11/17	2017	291	Szponar et al[15]	2025	Calibration
PAS-T34-2018	Peru	-12.5975	-69.1831	7/14/18	7/27/18	2018	90.5	Szponar et al[15]	2025	Calibration
PAS-T35-2017	Peru	-12.5953	-69.1810	8/3/17	8/11/17	2017	22.5	Szponar et al[15]	2025	Calibration
PAS-T36-2017	Peru	-12.5986	-69.1783	8/4/17	8/11/17	2017	3.68	Szponar et al[15]	2025	Calibration
PAS-T38-2017	Peru	-12.5943	-69.1734	8/4/17	8/11/17	2017	3.28	Szponar et al[15]	2025	Calibration
PAS-T40-2017	Peru	-12.6039	-69.2128	8/4/17	8/11/17	2017	5.32	Szponar et al[15]	2025	Calibration
PAS-T41-2018	Peru	-12.6014	-69.2075	7/14/18	7/27/18	2018	5.89	Szponar et al[15]	2025	Calibration
PAS-T42-2017	Peru	-12.6028	-69.1992	8/3/17	8/11/17	2017	4.17	Szponar et al[15]	2025	Calibration
PAS-T43-2017	Peru	-12.6030	-69.1941	8/3/17	8/11/17	2017	5.5	Szponar et al[15]	2025	Calibration
PAS-T44-2017	Peru	-12.6017	-69.1900	8/3/17	8/11/17	2017	10.7	Szponar et al[15]	2025	Calibration
PAS-T44-2018	Peru	-12.6017	-69.1900	7/14/18	7/27/18	2018	6.03	Szponar et al[15]	2025	Calibration
PAS-T45-2017	Peru	-12.6002	-69.1886	8/3/17	8/11/17	2017	7.43	Szponar et al[15]	2025	Calibration
PAS-T48-2017	Peru	-12.6021	-69.1820	8/4/17	8/11/17	2017	19.8	Szponar et al[15]	2025	Calibration
PAS-T49-2017	Peru	-12.5993	-69.1831	8/3/17	8/11/17	2017	36.1	Szponar et al[15]	2025	Calibration
PAS-T50-2017	Peru	-12.5984	-69.1810	8/3/17	8/11/17	2017	16	Szponar et al[15]	2025	Calibration
PAS-T51-2017_1	Peru	-12.5982	-69.1753	8/4/17	8/11/17	2017	2.18	Szponar et al[15]	2025	Calibration
PAS-T51-2017_2	Peru	-12.5982	-69.1753	8/4/17	8/11/17	2017	2.45	Szponar et al[15]	2025	Calibration

PAS-T52-2017	Peru	-12.6059	-69.1963	8/3/17	8/11/17	2017	6.79	Szponar et al[15]	2025	Calibration
PAS-T53-2017	Peru	-12.6086	-69.1905	8/3/17	8/11/17	2017	2.86	Szponar et al[15]	2025	Calibration
PAS-T53-2018_1	Peru	-12.6086	-69.1905	7/14/18	7/27/18	2018	2.44	Szponar et al[15]	2025	Calibration
PAS-T55-2017	Peru	-12.5987	-69.1857	8/3/17	8/11/17	2017	22.9	Szponar et al[15]	2025	Calibration
PAS-T56-2017	Peru	-12.5947	-69.1835	8/3/17	8/11/17	2017	25.2	Szponar et al[15]	2025	Calibration
PAS-T57-2017	Peru	-12.6034	-69.1813	8/4/17	8/11/17	2017	7.74	Szponar et al[15]	2025	Calibration
PAS-T57-2018_1	Peru	-12.6034	-69.1813	7/14/18	7/27/18	2018	3.09	Szponar et al[15]	2025	Calibration
PAS-T57-2018_2	Peru	-12.6034	-69.1813	7/14/18	7/27/18	2018	3.02	Szponar et al[15]	2025	Calibration
PAS-T58-2017	Peru	-12.5969	-69.1841	8/3/17	8/11/17	2017	498	Szponar et al[15]	2025	Calibration
PAS-T59-2017	Peru	-12.5961	-69.1843	8/4/17	8/16/17	2017	96.1	Szponar et al[15]	2025	Calibration
PAS-T60-2017	Peru	-12.5869	-69.1948	8/15/17	8/23/17	2017	6.38	Szponar et al[15]	2025	Calibration
PAS-T60-2018	Peru	-12.5869	-69.1948	7/13/18	7/27/18	2018	12.8	Szponar et al[15]	2025	Calibration
PAS-R6-2017_1	Peru	-12.7200	-69.5883	8/7/17	8/24/17	2017	45.3	Szponar et al[15]	2025	Calibration
PAS-R6-2017_2	Peru	-12.7200	-69.5883	8/7/17	8/24/17	2017	43.8	Szponar et al[15]	2025	Calibration
PAS-R7-2017	Peru	-12.7180	-69.5865	8/7/17	8/24/17	2017	60.6	Szponar et al[15]	2025	Calibration
PAS-R8-2017_1	Peru	-12.7183	-69.5888	8/7/17	8/24/17	2017	5360	Szponar et al[15]	2025	Calibration
PAS-R8-2017_2	Peru	-12.7183	-69.5888	8/7/17	8/24/17	2017	5710	Szponar et al[15]	2025	Calibration
PAS-R8-2018_1	Peru	-12.7183	-69.5888	7/13/18	7/30/18	2018	35466	Szponar et al[15]	2025	Calibration
PAS-R9-2017_1	Peru	-12.7215	-69.5845	8/5/17	8/24/17	2017	9.79	Szponar et al[15]	2025	Calibration
PAS-R9-2017_2	Peru	-12.7215	-69.5845	8/5/17	8/24/17	2017	10.9	Szponar et al[15]	2025	Calibration
PAS-R10-2017	Peru	-12.7281	-69.5762	8/5/17	8/24/17	2017	8.37	Szponar et al[15]	2025	Calibration
PAS-R10-2018	Peru	-12.7281	-69.5762	7/13/18	7/30/18	2018	13.4	Szponar et al[15]	2025	Calibration
PAS-R13-2017	Peru	-12.7507	-69.5676	8/5/17	8/24/17	2017	4.61	Szponar et al[15]	2025	Calibration
PAS-R14-2017	Peru	-12.7620	-69.5668	8/5/17	8/24/17	2017	3.16	Szponar et al[15]	2025	Calibration
PAS-R14-2018	Peru	-12.7620	-69.5668	7/13/18	7/30/18	2018	4.09	Szponar et al[15]	2025	Calibration
PAS-R15-2017	Peru	-13.1016	-70.3716	8/7/17	8/24/17	2017	24	Szponar et al[15]	2025	Calibration
PAS-R15-2018	Peru	-13.1016	-70.3716	7/13/18	7/30/18	2018	127	Szponar et al[15]	2025	Calibration
PAS-R16-2017	Peru	-13.1012	-70.3675	8/7/17	8/24/17	2017	273.9	Szponar et al[15]	2025	Calibration
PAS-R16-2018	Peru	-13.1012	-70.3675	7/13/18	7/30/18	2018	105.1	Szponar et al[15]	2025	Calibration
PAS-R17-2017_1	Peru	-13.1037	-70.3674	8/7/17	8/24/17	2017	23.8	Szponar et al[15]	2025	Calibration
PAS-R17-2017_2	Peru	-13.1037	-70.3674	8/7/17	8/24/17	2017	26.4	Szponar et al[15]	2025	Calibration
PAS-R17-2018	Peru	-13.1037	-70.3674	7/13/18	7/30/18	2018	21.5	Szponar et al[15]	2025	Calibration
PAS-R18-2017	Peru	-13.0900	-70.3636	8/7/17	8/24/17	2017	57.6	Szponar et al[15]	2025	Calibration
PAS-R18-2018	Peru	-13.0900	-70.3636	7/13/18	7/30/18	2018	122	Szponar et al[15]	2025	Calibration
PAS-R19-2017	Peru	-13.0807	-70.3599	8/7/17	8/24/17	2017	9.57	Szponar et al[15]	2025	Calibration
PAS-R20-2017	Peru	-13.0732	-70.3576	8/7/17	8/24/17	2017	6.29	Szponar et al[15]	2025	Calibration
PAS-R20-2018	Peru	-13.0732	-70.3576	7/13/18	7/30/18	2018	7.96	Szponar et al[15]	2025	Calibration
PAS-R25-2017	Peru	-13.0620	-70.3501	8/7/17	8/24/17	2017	4.77	Szponar et al[15]	2025	Calibration
PAS-R27-2017	Peru	-13.0094	-70.3454	8/7/17	8/24/17	2017	3.09	Szponar et al[15]	2025	Calibration
PAS-R27-2018	Peru	-13.0094	-70.3454	7/13/18	7/30/18	2018	2.79	Szponar et al[15]	2025	Calibration
PAS-R29-2017	Peru	-12.9713	-70.3391	8/7/17	8/24/17	2017	2.53	Szponar et al[15]	2025	Calibration
PAS-R30-2017	Peru	-12.9593	-70.3123	8/7/17	8/24/17	2017	2.41	Szponar et al[15]	2025	Calibration

PAS-R32-2017	Peru	-12.9307	-70.2642	8/7/17	8/24/17	2017	2.8	Szponar et al[15]	2025	Calibration
PAS-R34-2017	Peru	-12.9146	-70.1930	8/7/17	8/24/17	2017	3.42	Szponar et al[15]	2025	Calibration
PAS-R34-2018	Peru	-12.9146	-70.1930	7/13/18	7/30/18	2018	3.88	Szponar et al[15]	2025	Calibration
PAS-R35-2017	Peru	-12.9137	-70.1182	8/7/17	8/24/17	2017	4.3	Szponar et al[15]	2025	Calibration
PAS-R37-2017	Peru	-12.8925	-70.0671	8/7/17	8/24/17	2017	9.56	Szponar et al[15]	2025	Calibration
PAS-R37-2018	Peru	-12.8925	-70.0671	7/13/18	7/30/18	2018	9.75	Szponar et al[15]	2025	Calibration
PAS-R39-2017_1	Peru	-12.8772	-70.0386	8/7/17	8/24/17	2017	79.3	Szponar et al[15]	2025	Calibration
PAS-R39-2017_2	Peru	-12.8772	-70.0386	8/7/17	8/24/17	2017	87	Szponar et al[15]	2025	Calibration
PAS-R41-2017	Peru	-12.8914	-70.0029	8/7/17	8/24/17	2017	29.7	Szponar et al[15]	2025	Calibration
PAS-R41-2018	Peru	-12.8914	-70.0029	7/13/18	7/30/18	2018	35.6	Szponar et al[15]	2025	Calibration
PAS-R42-2017	Peru	-12.8924	-69.9875	8/7/17	8/24/17	2017	4.75	Szponar et al[15]	2025	Calibration
PAS-R42-2018	Peru	-12.8924	-69.9875	7/13/18	7/30/18	2018	7.37	Szponar et al[15]	2025	Calibration
PAS-R43-2017	Peru	-12.8999	-69.9445	8/7/17	8/24/17	2017	20.3	Szponar et al[15]	2025	Calibration
PAS-R44-2017	Peru	-12.8924	-69.8912	8/7/17	8/24/17	2017	4.41	Szponar et al[15]	2025	Calibration
PAS-R45-2017	Peru	-12.8755	-69.8041	8/7/17	8/24/17	2017	4.5	Szponar et al[15]	2025	Calibration
PAS-R48-2017	Peru	-12.8653	-69.6942	8/7/17	8/24/17	2017	2.75	Szponar et al[15]	2025	Calibration
PAS-R48-2018	Peru	-12.8653	-69.6942	7/13/18	7/30/18	2018	4.18	Szponar et al[15]	2025	Calibration
PAS-R49-2017	Peru	-12.7949	-69.6259	8/7/17	8/24/17	2017	3.11	Szponar et al[15]	2025	Calibration
PAS-R52-2017	Peru	-12.7266	-69.5052	8/5/17	8/24/17	2017	3.76	Szponar et al[15]	2025	Calibration
PAS-R53-2017	Peru	-12.7047	-69.4439	8/5/17	8/24/17	2017	2.34	Szponar et al[15]	2025	Calibration
PAS-R54-2017	Peru	-12.6801	-69.3761	8/5/17	8/24/17	2017	4.05	Szponar et al[15]	2025	Calibration
PAS-R55-2017	Peru	-12.6587	-69.3185	8/5/17	8/25/17	2017	3.1	Szponar et al[15]	2025	Calibration
PAS-R56-2017_1	Peru	-12.6432	-69.2733	8/5/17	8/24/17	2017	2.53	Szponar et al[15]	2025	Calibration
PAS-R56-2017_2	Peru	-12.6432	-69.2733	8/5/17	8/24/17	2017	2.83	Szponar et al[15]	2025	Calibration
PAS-R57-2017	Peru	-12.6106	-69.2422	8/7/17	8/24/17	2017	2.29	Szponar et al[15]	2025	Calibration
PAS-R57-2018_1	Peru	-12.6106	-69.2422	7/13/18	7/30/18	2018	2.63	Szponar et al[15]	2025	Calibration
PAS-R57-2018_2	Peru	-12.6106	-69.2422	7/13/18	7/30/18	2018	2.29	Szponar et al[15]	2025	Calibration
PAS_LP_2017_1	Peru	-12.2271	-69.1120	8/13/17	10/23/17	2017	0.76	Szponar et al[15]	2025	Calibration
PAS_LP_2017_3	Peru	-12.2271	-69.1120	8/13/17	10/23/17	2017	0.52	Szponar et al[15]	2025	Calibration
PAS_CHI_2018_1	Peru	-12.4809	-70.5810	7/16/18	8/14/18	2018	0.8	Szponar et al[15]	2025	Calibration
PAS_BDM_2018_33	Peru	-12.2691	-70.9105	6/4/18	7/24/18	2018	0.68	Szponar et al[15]	2025	Calibration
PAS_BDM_2018_43	Peru	-12.2681	-70.8862	7/17/18	8/14/18	2018	0.92	Szponar et al[15]	2025	Calibration
PAS_Limonal_2018_27	Peru	-12.2332	-70.9395	6/4/18	7/24/18	2018	0.64	Szponar et al[15]	2025	Calibration
PAS_Pakitza_2018_25	Peru	-11.9442	-71.2828	6/4/18	7/23/18	2018	0.83	Szponar et al[15]	2025	Calibration
PAS_CCashu_2018_20	Peru	-11.8888	-71.4074	6/13/18	8/14/18	2018	0.49	Szponar et al[15]	2025	Calibration
PAS_Yomibato_2018_21	Peru	-11.8034	-71.9107	6/7/18	7/23/18	2018	0.7	Szponar et al[15]	2025	Calibration
PAS_IIAP_2017_1	Peru	-12.6527	-69.3212	8/21/17	5/8/18	2017	1.07	Szponar et al[15]	2025	Calibration
PAS_IIAP_2017_2	Peru	-12.6527	-69.3212	8/21/17	5/8/18	2017	1.56	Szponar et al[15]	2025	Calibration
PAS_PAU_1_2017_1	Peru	-12.6822	-69.6167	8/10/17	5/22/18	2017	1.74	Szponar et al[15]	2025	Calibration

PAS_PAU_1_2017_2	Peru	-12.6822	-69.6167	8/10/17	5/22/18	2017	1.77	Szponar et al[15]	2025	Calibration
PAS_PAU_4_2017	Peru	-12.6838	-69.6176	8/10/17	5/22/18	2017	1.64	Szponar et al[15]	2025	Calibration
PAS_PAU_4_2018	Peru	-12.6838	-69.6176	5/22/18	7/23/18	2018	5.06	Szponar et al[15]	2025	Calibration
PAS_LAB_2018_38	Peru	-12.7212	-69.5862	7/15/18	8/17/18	2018	9.55	Szponar et al[15]	2025	Calibration
PAS_BC_2018_32	Peru	-12.6158	-70.3871	6/3/18	6/14/18	2018	25	Szponar et al[15]	2025	Calibration
PAS_BC_2018_42	Peru	-12.6073	-70.3412	7/16/18	8/15/18	2018	10.9	Szponar et al[15]	2025	Calibration
PAS_LA_2018_1	Peru	-12.5633	-70.0995	6/6/18	7/14/18	2018	0.61	Szponar et al[15]	2025	Calibration
PAS_LA_2018_7	Peru	-12.5601	-70.0972	6/6/18	7/14/18	2018	2.03	Szponar et al[15]	2025	Calibration
PAS_LA_2018_4	Peru	-12.5572	-70.0909	6/6/18	7/14/18	2018	2.13	Szponar et al[15]	2025	Calibration
PAS_LA_2018_11	Peru	-12.5650	-70.1031	6/6/18	7/14/18	2018	3.24	Szponar et al[15]	2025	Calibration
PAS_LA_2018_6	Peru	-12.5691	-70.0997	7/15/18	8/16/18	2018	2.63	Szponar et al[15]	2025	Calibration
Cristalino State	Brazil	-9.5978	-55.9323	12/5/17	3/27/19	2018	0.59	Quant[38]	2021	Validation
Puruzinho, AM	Brazil	-7.3706	-63.0594	3/24/18	4/6/19	2018	0.79	Quant[38]	2021	Validation
Manaus, AM	Brazil	-2.1440	-59.0000	10/24/18	12/11/19	2019	0.61	Quant[38]	2021	Validation
Amazonía	Colombia	-4.1915	-69.9394	12/14/17	1/9/19	2018	0.99	Quant[38]	2021	Validation
Background Station	Suriname	5.9500	-57.0333	3/14/07	5/1/07	2007	1.4	Wip et al[17]	2011	Validation
Outskirt Station	Suriname	5.8000	-55.2000	10/28/06	11/30/06	2006	2.4	Wip et al[17]	2011	Validation
Paramaribo	Suriname	5.8318	-55.1527	11/30/06	1/8/07	2006	5.6	Wip et al[17]	2011	Validation
Mine	Guyana	5.2819	-59.0580	5/1/23	8/1/23	2023	93	Watmough & Osborne[210]	2025	Validation
Adjacent	Guyana	5.2761	-59.0671	5/1/23	8/1/23	2023	3.69	Watmough & Osborne[210]	2025	Validation
Distant	Guyana	5.2822	-59.0955	5/1/23	8/1/23	2023	2.25	Watmough & Osborne[210]	2025	Validation
B. HORIZONTE	Peru	-12.4804	-69.0838	3/1/24	5/31/24	2024	0.69	This study	NA	Validation
MERCEDES	Peru	-12.6989	-69.5159	3/2/24	5/26/24	2024	2	This study	NA	Validation
Los Amigos	Peru	-12.5563	-70.1199	3/15/24	5/17/24	2024	1.52	This study	NA	Validation
Kilo	Peru	-12.5177	-70.0839	9/20/23	5/16/24	2024	1.11	This study	NA	Validation
EBLA	Peru	-12.5599	-70.1018	9/17/23	5/10/24	2024	1.82	This study	NA	Validation
Los Amigos Tree	Peru	-12.5572	-70.0915	9/19/23	5/8/24	2024	1.47	This study	NA	Validation
EBLA-2025	Peru	-12.5599	-70.1018	5/10/24	9/18/25	2024	2.23	This study	NA	Validation
KILO-2025	Peru	-12.5177	-70.0839	5/16/24	9/23/25	2024	1.68	This study	NA	Validation
TAM-2025	Peru	-12.8316	-69.2837	7/31/24	10/19/24	2024	1.74	This study	NA	Validation
LP-2025	Peru	-13.0178	-69.9452	8/29/24	12/4/24	2024	4.62	This study	NA	Validation
CC-2025	Peru	-11.8883	-71.4074	1/19/25	4/15/25	2024	1.19	This study	NA	Validation

Table SI 6-2 shows the estimated replacement time per cm of baseline soil mercury, along with a baseline estimate of the equilibrium residence time of the 0-5 cm surficial pool from authors' sampling sites along with prior study sites[19,113].

Site	1-cm res. time (years)	Surficial 5-cm res. time (years)
CM2 Tower	11-76	55-380
KILO Tower	19-123	75-618

Los Amigos River	16-106	80-530
La Pampa	16-105	80-525
Los Amigos Tower	27-180	135-900
Tambopata Tower	11-74	55-370
Los Amigos Station	73-146	365-730
Paulita	39-79	195-395
Laberinto	23-46	115-230
Boca Manu	18-35	90-175
Chilive	23-46	115-230
Colorado	23-45	115-225
Cocha Cashu	27-54	135-270

Table SI 6-3 compiles particulate mercury, total suspended solids, and mercury concentrations in suspended particulates across wet season and dry season measurements reported by prior Amazon studies. Ambiguous shoulder season measurements[198] were reported as wet season for the purpose of comparison. For studies[20] where only total particulate mercury and total suspended solid concentrations were reported, the particulate mercury concentration within suspended solids were computed by dividing the former by the latter with quadrature fractional error propagation. When only total suspended solid and mercury concentrations within suspended solid data were available,[201] total river particulate mercury concentrations were calculated via multiplication but errors were not computed on the result as they would overestimate the study's measured sample error in river particulate mercury concentrations. For a blackwater study[200] where multiple depth profiles were reported, we included only 5-6 meter depth samples from the center of the river, because we believe that they are more representative of average water concentrations than organic rich surficial water.

Site	Water type	Wet Season River Particulate mercury ($ng\ L^{-1}$)	Wet Season Suspended Solids ($mg\ L^{-1}$)	Wet Season Susp Solids Hg ($ng\ g^{-1}$)	Dry Season River Hg ($ng\ L^{-1}$)	Dry Season Suspended Solids ($mg\ L^{-1}$)	Dry Season Susp. Solid Hg ($ng\ g^{-1}$)
Madre de Dios (Headwaters)[20]	Whitewater	7.0 ± 1.7	527 ± 22	13.3 ± 3.3	0.4 ± 1.7	125 ± 22	3.2 ± 13.6
Madre de Dios (middle reach)[20]	Whitewater	17.0 ± 1.4	617 ± 36	27.6 ± 2.8	10.4 ± 1.4	215 ± 36	48.4 ± 10.4
Madre de Dios (lower reach)[20]	Whitewater	21.6 ± 1.7	514 ± 44	42.0 ± 4.9	15.0 ± 1.7	112 ± 44	134 ± 55
Upper Madeira (Bolivia)[211]	Whitewater			93.4 ± 13.0			
Amazon River[201]	Whitewater	1.6-3.3	28-58	57 [no std rep.]	2.3 [no std rep.]	89 [no std rep.]	26 [no std rep.]
Amazon floodplain Lake[201]	Whitewater	5.4 [no std rep.]	9.7 ± 3.7	560 ± 490	95 [no std rep.]	790 ± 730	120 ± 130
Madeira near confluence[200]	Whitewater	5.5 [no std rep.]	49.9-56.2	58-93			
Solimões near confluence[200]	Whitewater	5.9 [no std rep.]	74.8 [no std rep.]	79 [no std rep.]			
Tapajos[198]	Clearwater	76 [no std rep.]	540 [no std rep.]	134 [no std rep.]			
Tapajos[199]	Clearwater	4.63 ± 4.41	70 ± 40	66 ± 74			
Amazon floodplain lakes[201]	Blackwater	3.0 [no std rep.]	8.7 ± 10.9	350 ± 380			
Negro near confluence[200]	Blackwater	5.6 ± 0.35	5.3 [no std rep.]	1100 ± 70			